Supplementary Information to accompany

Systematic Control of the Spin Crossover Profile in Dinuclear Iron(III) Complexes via the Bridging Ligand Redox-State

Jett T. Janetzki,[1] Maxim G. Chegerev,[2] I. Haseena Ismail,[1] Robert W. Gable,[1] Roger J. Mulder,[3] Guy N. L. Jameson,[1] Lorenzo Sorace,[4] Alyona A. Starikova,[2] and Colette Boskovic[*,1]*

[1] School of Chemistry, University of Melbourne, Victoria 3010, Australia

[2] Institute of Physical and Organic Chemistry, Southern Federal University, 344090, Rostov-on-Don, Russian Federation

[3] CSIRO Manufacturing, Clayton, Victoria 3168, Australia

[4] Department of Chemistry, "Ugo Schiff" and INSTM RU Università degli Studi di Firenze, Via della Lastruccia, 3, 50019 Sesto Fiorentino, Italy

Contents

Experimental and Synthetic Methods

Synthesis

All manipulations, unless otherwise indicated, were performed under anaerobic conditions in an M-Braun N_2-atmosphere glove box or on a Schlenk line with N_2 gas using standard Schlenk techniques. All chemicals purchased were of reagent grade or higher and used as received, except Bu_4NPF_6 and ferrocene which were purified from hot ethanol recrystallization and sublimation, respectively. Solvents were dried over molecular sieves (3 Å) for a minimum of 3 days and stored under N_2 on sieves until used. Solvents were degassed prior to use via 3 freeze-pump-thaw cycles. Molecular sieves were activated by heating at 300 °C for 48 hours and then cooled under vacuum. Ligand $theaH_4$,[1] $[\{Fe^{III}(tpa)\}_2(thea)](PF_6)_2$ (**1**) (see below),[2] and $[\{Co^{III}(tpa)\}_2(thea)](PF_6)_3$ (**2-Co**) and $[\{Co^{III}(tpa)\}_2(thea)](PF_6)_4$ (**3-Co**)[3] were prepared as previously reported.

$[\{Fe^{III}(tpa)\}_2(thea)](PF_6)_2$ (1). A methanolic solution of tpa (0.25 g, 0.86 mmol; 10 mL) was added dropwise to a methanolic solution of $FeCl_3$ (0.14 g, 0.85 mmol; 25 mL), and left to stir for 15 minutes. After, a methanolic solution of $theaH_4$ (0.13 g, 0.43 mmol; 20 mL), deprotonated with Et_3N (240 μL, 1.7 mmol), was subsequently added resulting in a yellow to dark blue purple change. After stirring for 30 minutes, the solution was filtered to remove the formed solid and combined with a methanolic solution of KPF_6 (0.16 g, 0.88 mmol; 15 mL). The volume of methanol was reduced to create a saturated solution, and then left at −18 °C for 24 hours, after which a microcrystalline powder formed. The solid was collected by vacuum filtration in air, washed with cold methanol and Et_2O, and air dried to yield **1** as a dark purple solid (0.18 g, 78%). Layering a concentrated MeCN solution with Et_2O afforded dark purple rods suitable for X-ray diffraction. The crude product was recrystallized by layering a filtered MeCN solution of **1** (0.24 g, 8.8 mL) below 20 ml iPr$_2$O, which after one week, yielded a microcrystalline product (0.18 g, 75%). The sample was collected and washed with iPr$_2$O, with

the crystalline product appearing hygroscopic, analyzing as **1**·2H_2O·0.5*i*Pr_2O. Anal. Calcd for $C_{57}H_{61}Fe_2N_8O_{6.5}P_2F_{12}$: C, 50.20; H, 4.51; N, 8.22. Found C, 50.31; H, 4.11; N, 7.86. Selected FT-IR data (ATR, cm^{-1}): 2930 (w), 1605 (s), 1445 (m), 1284 (s), 1024 (s), 830 (s), 764 (s), 556 (s). UV-Vis (acetonitrile) λ_{max} (ε): 520 (2720), 1020 nm (5660 L mol^{-1} cm^{-1}).

[{Fe^{III}(tpa)}$_2$(thea)](PF$_6$)$_3$ (**2**). To a stirred solution of compound **1** (0.19 g, 0.15 mmol) in 15 mL MeCN was added a solid $FcPF_6$ (0.056 g, 0.17 mmol), resulting in color change from bright purple to grey-purple. The resulting solution was stirred at room temperature for 1.5 hours, followed by 30 minutes of sonication, before cannula filtration to remove insoluble solids. The resulting solution was reduced in volume to saturation, after which Et_2O was added until a blue solid formed. The suspension was left at −18 °C for 24 hours, before collecting the solid in air and washing with Et_2O and toluene and air drying to yield [{Fe^{III}(tpa)}$_2$(thea)](PF$_6$)$_3$ (0.19 g, 90%). Layering a concentrated MeCN solution with toluene afforded dark blue rods suitable for X-ray diffraction. The crude product was recrystallized by layering a filtered MeCN solution (0.02 g, 0.5 mL MeCN) with 5 mL toluene (9 batches, 0.18 g of product total), which after one week, yielded a crystalline product. The sample was vacuum collected in air and washed with toluene and Et_2O, appearing hygroscopic, analyzing as **2**·0.5toluene·3H_2O (0.13 g, 72%). Anal. Calcd for $C_{54}H_{50}Fe_2N_8O_4P_3F_{18}$·0.5toluene·3$H_2O$: C, 45.38; H, 3.97; N, 7.36 Found C, 45.30; H, 3.76; N, 7.19. Selected FT-IR data (ATR, cm^{-1}): 3650 (w), 1607 (m), 1432 (m), 1288 (m), 1024 (m), 830 (s), 765 (m), 554 (m). UV-Vis (acetonitrile) λ_{max} (ε): 842 nm (2,700 L mol^{-1} cm^{-1}), 512 (2,900 L mol^{-1} cm^{-1}).

[{Fe^{III}(tpa)}$_2$(thea)](PF$_6$)$_4$ (**3**). A 0.5 mL MeCN solution of $NOPF_6$ (0.015 g, 0.086 mmol) was added dropwise to a filtered 1 mL MeCN solution of compound **1** (0.05 g, 0.04 mmol), causing an immediate color change from purple to dark blue/green. The solution was filtered and layered with 5 mL *i*Pr_2O. After one week, a dark blue crystalline solid formed, which was collected and washed with Et_2O and air dried to yield [{Fe^{III}(tpa)}$_2$(thea)](PF$_6$)$_4$

(0.06 g, 95%). The product was recrystallized by layering a filtered MeCN solution (0.03 g, 0.7 mL MeCN) with toluene (4 mL), which after one week, yielded a dark blue crystalline product. The product was vacuum collected in air, washed with toluene, analyzing as **3**·0.5MeCN (0.041 g). Anal. Calcd for $C_{54}H_{50}Fe_2N_8O_4P_4F_{24}$·0.5MeCN: C, 41.62; H, 3.27; N, 7.50. Found C, 41.44; H, 3.36; N, 7.19. Selected FT-IR data (ATR, cm^{-1}): 3668 (w), 1611 (m), 1436 (m), 1374 (m), 1296 (m), 830 (s), 764 (m), 556 (s), 530 (m). UV-Vis (acetonitrile) λ_{max} (ε): 396 nm (3,400 L mol^{-1} cm^{-1}). Single crystals of X-ray diffraction quality were grown by: A 1.2 mL MeCN solution of $NOPF_6$ (0.015 g, 0.086 mmol) was added dropwise to a filtered 1 mL MeCN solution of $[\{Fe^{III}(tpa)\}_2(thea)](PF_6)_2$ (0.05 g, 0.04 mmol), filtered, then layered below 5 mL *i*Pr_2O to yield dark blue crystals after one week.

Note on crystallinity and bulk sample preparation: For all complexes, rapid crystallization and the large sample quantities required for bulk analyses (e.g., Mössbauer spectroscopy) unavoidably lead to partial amorphous content in the isolated powders. Powder X-ray diffraction (PXRD) analysis shows broad scattering features consistent with this (Figure S3). However, baseline-corrected PXRD for **1** and **2** confirms that the crystalline fraction of the bulk material matches the simulated patterns from SCXRD (Figure S4), consistent with the same crystalline phase. This point is explicitly acknowledged in the discussion and conclusions.

X-ray Data Collection and Structure Solution

Single X-ray diffraction data for **2**·3toluene·2MeCN and **3**·2MeCN 3*i*Pr_2O were collected at the Australian Synchrotron MX2[4] and MX1[5] beamlines, respectively, tuned to approximate Mo-Kα radiation (λ = 0.71075 Å, MX1; λ = 0.71092 Å, MX2) fitted with a silicon double crystal monochromator. Data reduction was performed using XDS, using strong multi-scan absorption correction in SADABS. Data for crystals mounted on MX1 were collected at

multiple orientations and merged with SADABS,[6] while data for crystals mounted on MX2 (those too weakly scattering to enable the collection of adequate data from MX1) were only able to be collected around one rotation axis. Crystals were transferred directly from the mother liquor to crystallographic oil to prevent solvent loss and loss of crystallinity. Structures were solved with SHELXT[7] and refined using a full matrix least squared procedure based on F^2 using SHELXL within Olex2.[8,9] All non-hydrogen atoms were refined using anisotropic displacement factors. Hydrogen atoms were placed at geometrical positions and refined using the riding model.

2: All temperatures: Both PF_6^- anions were refined over three different orientations, constrained to ideal geometry. For the PF_6^- anion situated around the center of symmetry, displacement parameters of each component were constrained to be equal. For the other PF_6^- anion, the displacement parameters of each component were constrained to be similar. One MeCN and one toluene were severely disordered and attempts to model this was unsuccessful. Accordingly, the OLEX2 solvent mask routine was used to account for the contribution of this solvent to the data.[10] Collections at 150, 200, 250, 275, 285, 290, 295, 300, 305, 310 K: The second toluene molecule, situated around a 2-fold axis, was constrained to ideal geometry. Collections at 100, 315, 325, 350 K: The second toluene molecule, situated around a 2-fold axis, was disordered. Attempts to model this was unsuccessful. Accordingly, the OLEX2 solvent mask routine was used to account for the contribution of this solvent to the data.[10]

3: One PF_6^- was localized, two PF_6^- anions was refined over two different orientations, and the other PF_6^- anion were refined over three different orientations; the components of all anions were restrained to have ideal geometry and to have similar displacement parameters. Two MeCN and three iPr$_2$O molecules were severely disordered and attempts to model this was unsuccessful Accordingly, the OLEX2 solvent mask routine was used to account for the

contribution of this solvent to the data.[10] The crystal showed evidence of disorder. In the final difference map, there are electron peaks (0.6-1.0 e $Å^{-3}$) around the PF_6^- anions due to incomplete modelling of the disorder, and the Fe atom which is attributed to disorder of the crystal. There is also a peak (~1.8 e $Å^{-3}$) close to one of the carbon atoms of the tpa ligand. As the temperature increased, this peak reduced in intensity and moved further away from the carbon atom, before becoming no longer apparent at 350K. This electron peak is attributed to disorder of the crystal rather than a chemical component of the cation.

Powder X-ray diffraction (PXRD) data were measured on a Rigaku Synergy Dual Wavelength Rotating Anode X-ray Diffractometer System using Cu-Kα (λ = 1.5418 Å) at 100 K. Powder samples were prepared by crushing the sample gently and loading them into a borosilicate glass capillary for measurement. Data were collected at $2\theta = 50°$ with an exposure time of 60 seconds per frame and processed using CrysAlisPro. Due to partial amorphous content inherent to bulk preparations, the raw PXRD patterns contain significant diffuse scattering. To better assess the crystalline component, baseline correction was applied; the corrected patterns for **1** and **2** match the simulated patterns from SCXRD (Figure S4). Accordingly, while we do not claim complete phase purity, the crystalline fraction of the bulk is consistent with the single-crystal phase.

UV-Vis-NIR and IR Spectroscopy

Attenuated total reflectance infrared spectra were measured on a Bruker Alpha spectrometer and normalized as absorbance spectra. Samples for solution UV-Visible-NIR measurements were prepared in an M-Braun N_2-atmosphere glove box and placed in a gastight cuvette. Solution state UV-Visible-NIR spectra were measured on a PerkinElmer UV-Vis-NIR Spectrometer Lambda 1050. Variable temperature UV-Visible absorption spectra were measured on an Agilent Cary UV-Visible Multicell Peltier Spectrometer, with a flow of N_2 gas

to remove condensation. Diffuse reflectance UV-Visible spectra were measured on the samples diluted ~5% in KBr on a Thermo Scientific Evolution 220 UV-Visible spectrophotometer.

Electrochemistry

Samples for electrochemical measurements were prepared in an M-Braun N_2-atmosphere glove box. Electrochemical measurements were performed in MeCN at room temperature using a standard three-electrode configuration connected to an eDAQ computer-controlled potentiostat. Measurements were performed under a constant flow of N_2. For cyclic voltammetry measurements, the three-electrode system consisted of a 1.0 mm diameter glassy carbon electrode (Cypress Systems), a platinum/titanium auxiliary electrode (eDAQ), and a Ag/AgCl reference electrode (eDAQ). For steady state voltammetry measurements, the working electrode was replaced with a 3.0 mm diameter glassy carbon rotating disk electrode with external controller (Metrohm). Analyte solutions of 1.0 mM were prepared using anaerobic techniques in 5 ml MeCN containing 0.25 M Bu_4NPF_6 as the supporting electrolyte. All potentials have been references *versus* the ferrocene/ferrocenium redox couple, measured immediately afterwards. The cyclic voltammetry (CV) midpoint potentials (E_m) are calculated by taking the average of the anodic and cathodic peak potentials (Ep). The half-wave potentials ($E_{1/2}$) are calculated as the potential at half the limiting current (i_L). Reversible processes are identified by peak-to-peak separations (ΔE_p) close to the value measured under the same conditions for ferrocene at a scan rate of 100 mV s^{-1}.

Variable Temperature NMR and Solution-Based Magnetic Measurements

Variable temperature ^{1}H NMR measurements on compound **3**, measured in d_3-MeCN (253 – 333 K) and CD_2Cl_2 (253 – 303 K), were recorded on a Bruker Ascend 400 MHz NMR spectrometer equipped with a BCUII temperature control. The solution samples were prepared in an M-Braun N_2-atmosphere glove box and measured in an anaerobic NMR tube equipped

with a J Young tap. Solution-based magnetic susceptibility measurements for compounds **1**, **2** and **3** were measured in MeCN (238 – 318 K) by ^{1}H NMR spectroscopy according to Evans method.[11] Measurements were recorded on a Bruker Av500 NMR spectrometer equipped with a 5 mm TCI CryoProbe Prodigy ^{1}H/^{2}H-^{13}C-^{15}N probe. Cooling was achieved with a Bruker BCU-II gas pre-conditioner. Sample temperature was calibrated using d_4-methanol and stable at ±0.1 K. The solution samples were prepared in an M-Braun N_2-atmosphere glove box and measured in an anaerobic NMR tube equipped with a J Young tap. A solvent mixture was prepared containing d_3-MeCN and 0.5 – 2% H_3-MeCN as a standard. The compound was dissolved in the solvent mixture under anaerobic conditions to form a solution of precisely known concentration and placed inside an NMR tube with an attached J-Young valve. A narrow capillary was filled with the same solvent mixture and placed inside the NMR tube as an internal reference. The shift in the H_3-MeCN singlet in the paramagnetic solution compared to H_3-MeCN in the internal references, Δυ in hertz, can be used to calculate the mass susceptibility of the compound, χ_g, according to eq S1.

$$\chi_g = \frac{3\Delta\upsilon}{4\pi m\upsilon} + \chi_0 + \chi_0 \frac{d_0 - d_s}{m} \qquad \text{(S1)}$$

where m is the concentration of the paramagnetic solution (in g cm^{-3}), corrected for the temperature dependence of the density of the solvent,[12,13] υ is the spectrometer frequency (in Hz), χ_0 is the mass susceptibility of the solvent mixture, d_0 is the density of the pure solvent mixture, and d_s is the density of the compound solution. As the sample solution is dilute, the following approximation can be made: $d_s = d_s + m$, leading to a cancelation of the second and third terms of eq. S1. The mass susceptibility is converted to the molar susceptibility by multiplying by the molecular weight (including molecules of solvation) and then corrected for the diamagnetic contribution of the compound using Pascal's constants.[14]

Solid-State Magnetic Measurements

The dc susceptibility and magnetization measurements for samples **1**·2H_2O·0.5*i*Pr_2O, **2**·0.5toluene·3H_2O and **3**·0.5MeCN were performed on a Quantum Design MPMS 3 SQUID magnetometer measured between 1.8 and 300 K with an applied field of 1000 Oe. Measurements employed scan rates of 2 K/min for 20–300 K, 1 K/min for 10–19 K, and 0.5 K/min for 1.8–9 K. The data was corrected for the diamagnetic contribution of the gel cap, and of the sample using Pascal's constants.[14] Each sample was measured from 300 to 1.8 K, before measuring back to 300 K. Magnetization (M) vs field (H) measurements were performed between 0 and 7 T at 1.8, 4 and 7 K. Fitting the magnetic data made use of the program PHI.[15]

Mössbauer Spectroscopy

^{57}Fe Mössbauer spectra were recorded for **1**·2H_2O·0.5*i*Pr_2O, **2**·0.5toluene·3H_2O and **3**·0.5MeCN with a ^{57}Co source in a Rh matrix on a SEE Co. (Science Engineering & Education Co., MN) spectrometer equipped with a closed-cycle refrigerator system. Data were collected in constant acceleration mode in transmission geometry. Isomer shifts are given relative to metallic iron foil at room temperature. Analysis of spectra were conducted using the WMOSS program (SEE Co, formerly WEB Research Co. Edina, MN).

Electron Paramagnetic Spectroscopy

The solution-state CW X-band EPR spectra were recorded at 10 K on a Bruker E500 spectrometer equipped with an ESR900 (Oxford Instruments) continuous flow ^{4}He cryostat and a SHQ resonator. The spectra were baseline corrected with a linear function. The measurements were performed on 1:1 DCM:toluene (0.05 mM) solutions of **1**, **2** and **3**. Samples were prepared in an M-Braun N_2-atmosphere glovebox by first dissolving the solid sample in DCM, followed by addition of toluene. The solution samples were inspected to make sure no

solid precipitate formed. The EPR spectra for **1** and **2** were simulated using EasySpin.[16] The solid-state X-band EPR spectra were recorded on a Bruker Magnettech ESR5000. Measurements were performed at 303 K, and at 77 K (liquid N_2 temperature) using a cold finger. The spectra were measured at 9.45 GHz and 10 mW, having confirmed linear power dependence.

Other Measurements

Elemental analyses (C, H, N) were performed at the Macquarie Analytical and Fabrication Facility, Macquarie University. Thermogravimetric analyses were performed on a Perkin Elmer TGA 8000 thermogravimetry analyzer using a ramp rate of 5 °C per minute from 30 °C up to a maximum temperature of 400 °C under an N_2 atmosphere.

Density Functional Theory (DFT) Calculations

The DFT calculations were performed using the Gaussian 16[17] program package with the UOPBE[18,19] functional and the 6-311++G(d,p) basis set including diffuse and polarization functions at all atoms. The stationary points on the potential energy surfaces (PESs) were localized by a full geometry optimization, with subsequent confirmation of the stabilities of the DFT wave function and calculation of the force constant matrices. Geometry optimizations of **1**, **2** and **3** were performed using the experimental crystal structures; the structure of **1** was used for calculation of **2-*meso***. The geometry optimization of the different charge distributions of **2** in four solvents (MeCN, BuCN, DCE and toluene) has been performed in the DFT OPBE/Def2-TZVP approximation using the ORCA program package.[20–23] The solvation effects were taken into account using the SMD continuum solvation model.[24] The geometry optimization of the [LS-cat-SQ-HS] state of the compound **2** with inclusion of the PF_6^- counterions into the computational scheme has been implemented by applying the DFT UOPBE/B97-3c (SMD, solvent = MeCN) and DFT UOPBE/Def2-TZVP (SMD, solvent =

MeCN) methods. The atomic coordinates obtained from experimental crystal structures were used as input files, excluding the counterions. Structural visualizations were prepared using the ChemCraft[25] software with the calculated atomic coordinates as input parameters.

Literature Compounds

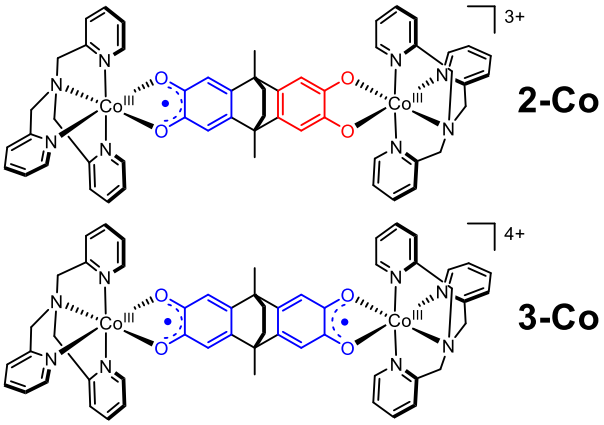

Figure S1. Dinuclear Co^{III} metal complexes in $[\{Co^{III}(tpa)\}_2(thea^{cat\text{-}SQ})](PF_6)_3$ (**2-Co**) and $[\{Co^{III}(tpa)\}_2(thea^{SQ\text{-}SQ})](PF_6)_4$ (**3-Co**), previously reported in reference [3].

Thermogravimetric Analysis

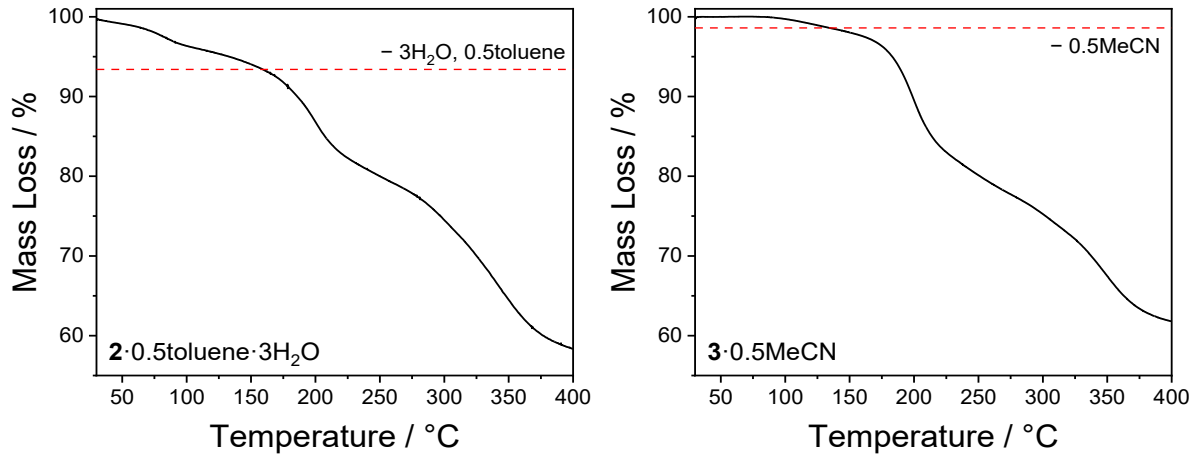

Figure S2. Thermogravimetric profile for **2**·0.5tol·$3H_2O$, and **3**·0.5MeCN, at a ramp rate of 5 °C min^{-1} under a flow of N_2.

Powder X-Ray Diffraction

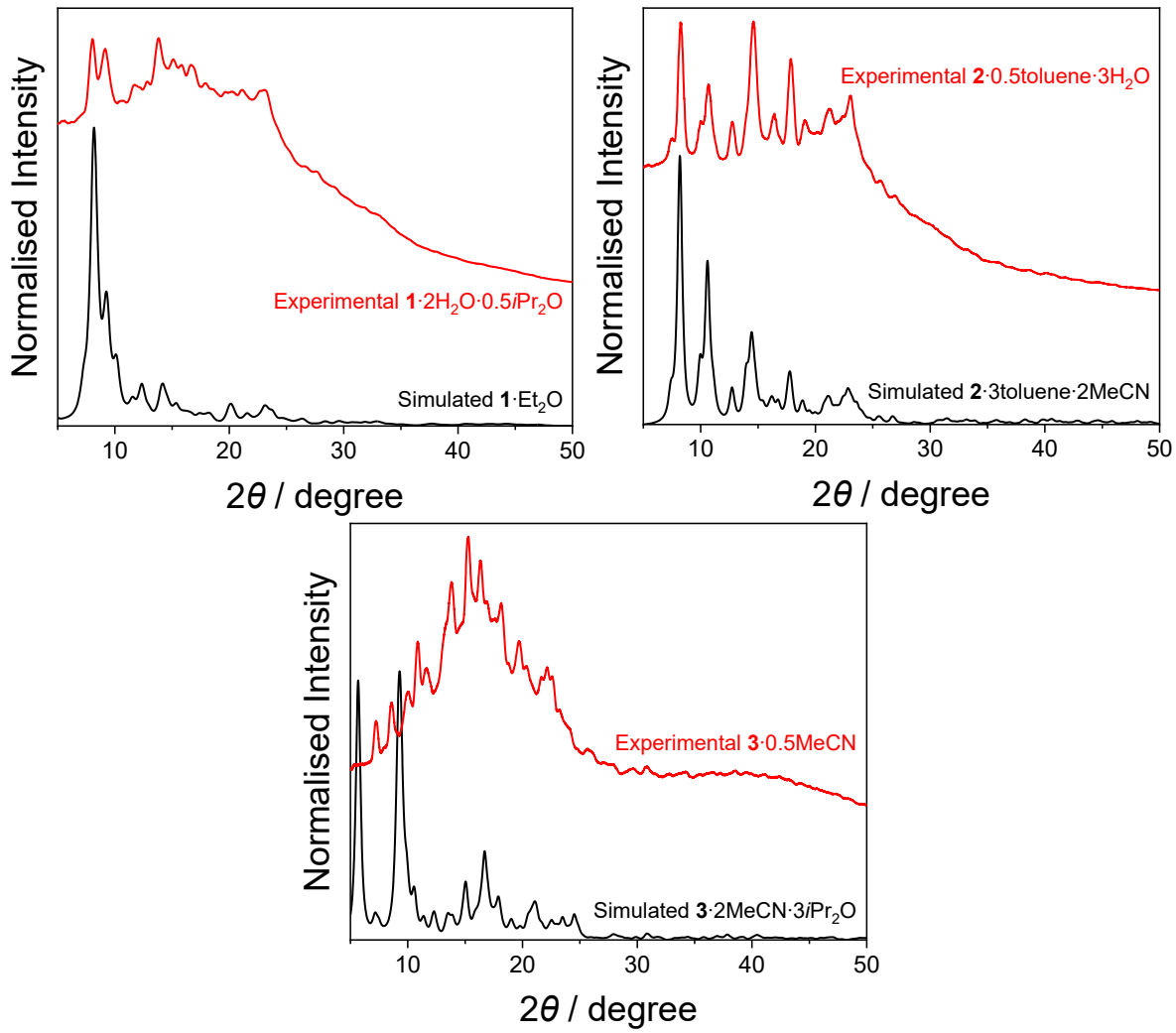

Figure S3. Top left: experimental PXRD pattern of **1**·3H_2O·0.5*i*Pr_2O at 100 K (red) and simulated PXRD pattern from crystal structure of **1**·Et_2O (black). Top right: experimental PXRD pattern of **2**·0.5toluene·3H_2O at 100 K (red) and simulated PXRD pattern from crystal structure of **2**·3toluene·2MeCN (black). Bottom: experimental PXRD pattern of **3**·0.5MeCN at 100 K (red) and simulated PXRD pattern from crystal structure of **3**·2MeCN·3*i*Pr_2O at 100 K. (black).

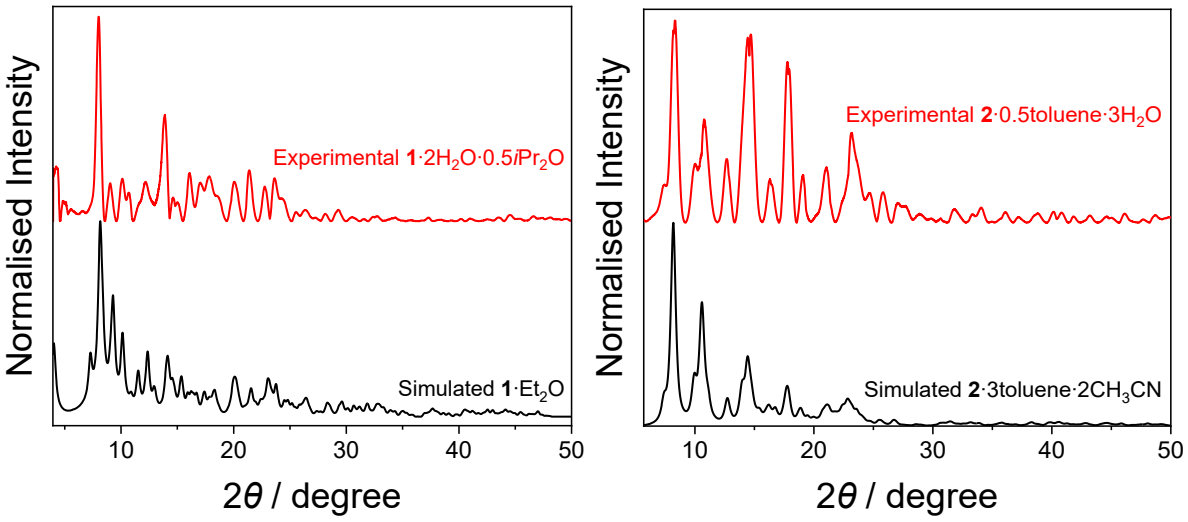

Figure S4. Left: baseline corrected experimental PXRD pattern of **1**·3H_2O·0.5*i*Pr_2O at 100 K (red) and simulated PXRD pattern from crystal structure of **1**·Et_2O (black). Right: baseline corrected experimental PXRD pattern of **2**·0.5toluene·3H_2O at 100 K (red) and simulated PXRD pattern from crystal structure of **2**·3toluene·2MeCN (black). While both samples display significant amorphous scattering in the raw data, baseline correction highlights the crystalline fraction, which shows a general match to the simulated patterns. This supports that the crystalline component is of the same phase as the SCXRD data, though amorphous contributions cannot be excluded.

Structural Data

Table S1. Crystallographic data and structure refinement parameters for compound **2**·3toluene·2MeCN at 100, 150, 200 and 250 K.

	2·3toluene·2MeCN (100 K)	**2**·3toluene·2MeCN (150 K)	**2**·3toluene·2MeCN (200 K)	**2**·3toluene·2MeCN (250 K)
Empirical formula	$C_{79}H_{80}F_{18}Fe_2N_{10}O_4P_3$	$C_{79}H_{80}F_{18}Fe_2N_{10}O_4P_3$	$C_{79}H_{80}F_{18}Fe_2N_{10}O_4P_3$	$C_{79}H_{80}F_{18}Fe_2N_{10}O_4P_3$
Formula weight	1780.14	1780.14	1780.14	1780.14
Temperature (K)	100.0(2)	150.0(2)	200.0(2)	250.0(2)
Crystal system	monoclinic	monoclinic	monoclinic	monoclinic
Space group	*P*2/n	*P*2/n	*P*2/n	*P*2/n
a (Å)	18.861(4)	18.943(4)	19.017(4)	19.089(4)
b (Å)	9.0330(18)	9.0420(18)	9.0620(18)	9.0840(18)
c (Å)	22.888(5)	22.966(5)	23.044(5)	23.177(5)
α (°)	90	90	90	90
β (°)	109.31(3)	109.41(3)	109.41(3)	109.38(3)
γ (°)	90	90	90	90
Volume (Å^3)	3680.2(14)	3710.0(14)	3745.4(14)	3791.3(15)
Z	2	2	2	2
ρ_{calc} (g/cm^3)	1.606	1.594	1.578	1.559
μ (mm^{-1})	0.566	0.562	0.556	0.550
F(000)	1830.0	1830.0	1830.0	1830.0
Crystal size (mm^3)	0.23 × 0.15 × 0.13	0.25 × 0.15 × 0.13	0.25 × 0.15 × 0.13	0.25 × 0.15 × 0.13
Radiation	Synchrotron (λ = 0.71092)	Synchrotron (λ = 0.71092)	Synchrotron (λ = 0.71092)	Synchrotron (λ = 0.71092)
2*θ* range for data collection (°)	2.438 to 64.006	2.426 to 64.218	3.392 to 64.368	3.374 to 64.25
Index ranges	-25 ≤ h ≤ 25, -11 ≤ k ≤ 11, -32 ≤ l ≤ 32	-25 ≤ h ≤ 25, -11 ≤ k ≤ 11, -32 ≤ l ≤ 32	-25 ≤ h ≤ 25, -11 ≤ k ≤ 11, -32 ≤ l ≤ 32	-25 ≤ h ≤ 25, -11 ≤ k ≤ 11, -32 ≤ l ≤ 32
Reflections collected	63777	64552	65690	66099
Independent reflections	10659 [R_{int} = 0.0467, R_{sigma} = 0.0304]	10731 [R_{int} = 0.0455, R_{sigma} = 0.0286]	10900 [R_{int} = 0.0490, R_{sigma} = 0.0306]	10985 [R_{int} = 0.0657, R_{sigma} = 0.0388]
Data/restraints/parameters	10659/305/562	10731/329/614	10900/347/602	10985/347/602
Goodness-of-fit on F^2	1.094	1.074	1.065	1.062
Final *R* indexes [$I \geq 2\sigma(I)$]	R_1 = 0.0506, wR_2 = 0.1576	R_1 = 0.0496, wR_2 = 0.1504	R_1 = 0.0475, wR_2 = 0.1438	R_1 = 0.0556, wR_2 = 0.1683
Final *R* indexes [all data]	R_1 = 0.0517, wR_2 = 0.1590	R_1 = 0.0516, wR_2 = 0.1538	R_1 = 0.0498, wR_2 = 0.1478	R_1 = 0.0589, wR_2 = 0.1748
Largest diff. peak/hole (e Å^{-3})	0.75/-0.77	0.67/-0.73	0.48/-0.60	0.44/-0.62

Table S2. Crystallographic data and structure refinement parameters for compound **2**·3toluene·2MeCN at 275, 285, 290 and 295 K.

	2·3toluene·2MeCN (275 K)	**2**·3toluene·2MeCN (285 K)	**2**·3toluene·2MeCN (290 K)	**2**·3toluene·2MeCN (295 K)
Empirical formula	$C_{79}H_{80}F_{18}Fe_2N_{10}O_4P_3$	$C_{79}H_{80}F_{18}Fe_2N_{10}O_4P_3$	$C_{79}H_{80}F_{18}Fe_2N_{10}O_4P_3$	$C_{79}H_{80}F_{18}Fe_2N_{10}O_4P_3$
Formula weight	1780.14	1780.14	1780.14	1780.14
Temperature (K)	275.0(2)	285.0(2)	290.0(2)	295.0(2)
Crystal system	monoclinic	monoclinic	monoclinic	monoclinic
Space group	*P*2/n	*P*2/n	*P*2/n	*P*2/n
a (Å)	19.130(4)	19.151(4)	19.152(4)	19.128(4)
b (Å)	9.1020(18)	9.1100(18)	9.1130(18)	9.1140(18)
c (Å)	23.265(5)	23.306(5)	23.318(5)	23.281(5)
α (°)	90	90	90	90
β (°)	109.35(3)	109.34(3)	109.33(3)	109.30(3)
γ (°)	90	90	90	90
Volume (Å^3)	3822.0(15)	3836.6(15)	3840.3(15)	3830.6(15)
Z	2	2	2	2
ρ_{calc} (g/cm^3)	1.547	1.541	1.539	1.543
μ (mm^{-1})	0.545	0.543	0.543	0.544
F(000)	1830.0	1830.0	1830.0	1830.0
Crystal size (mm^3)	0.23 × 0.15 × 0.13	0.23 × 0.15 × 0.13	0.23 × 0.15 × 0.13	0.23 × 0.15 × 0.13
Radiation	Synchrotron (λ = 0.71092)	Synchrotron (λ = 0.71092)	Synchrotron (λ = 0.71092)	Synchrotron (λ = 0.71092)
2*θ* range for data collection (°)	2.4 to 64.156	2.398 to 64.372	3.358 to 64.346	2.4 to 64.148
Index ranges	-25 ≤ h ≤ 25, -11 ≤ k ≤ 11, -32 ≤ l ≤ 32	-25 ≤ h ≤ 25, -11 ≤ k ≤ 11, -32 ≤ l ≤ 33	-25 ≤ h ≤ 25, -11 ≤ k ≤ 11, -32 ≤ l ≤ 33	-25 ≤ h ≤ 25, -11 ≤ k ≤ 11, -33 ≤ l ≤ 32
Reflections collected	66136	66491	65929	54006
Independent reflections	11061 [R_{int} = 0.0567, R_{sigma} = 0.0344]	11163 [R_{int} = 0.0569, R_{sigma} = 0.0361]	11145 [R_{int} = 0.0532, R_{sigma} = 0.0335]	10557 [R_{int} = 0.0591, R_{sigma} = 0.0439]
Data/restraints/parameters	11061/347/602	11163/371/601	11145/371/601	10557/365/601
Goodness-of-fit on F^2	1.074	1.070	1.077	1.042
Final *R* indexes [$I \geq 2\sigma(I)$]	R_1 = 0.0599, wR_2 = 0.1860	R_1 = 0.0653, wR_2 = 0.2074	R_1 = 0.0600, wR_2 = 0.1952	R_1 = 0.0695, wR_2 = 0.2130
Final *R* indexes [all data]	R_1 = 0.0645, wR_2 = 0.1954	R_1 = 0.0717, wR_2 = 0.2203	R_1 = 0.0684, wR_2 = 0.2088	R_1 = 0.0727, wR_2 = 0.2213
Largest diff. peak/hole (e Å^{-3})	0.45/-0.53	0.49/-0.42	0.37/-0.44	0.58/-0.54

Table S3. Crystallographic data and structure refinement parameters for compound **2**·3toluene·2MeCN at 300, 305, 310 and 315 K.

	2·3toluene·2MeCN (300 K)	**2**·3toluene·2MeCN (305 K)	**2**·3toluene·2MeCN (310 K)	**2**·3toluene·2MeCN (315 K)
Empirical formula	$C_{79}H_{80}F_{18}Fe_2N_{10}O_4P_3$	$C_{79}H_{80}F_{18}Fe_2N_{10}O_4P_3$	$C_{79}H_{80}F_{18}Fe_2N_{10}O_4P_3$	$C_{79}H_{80}F_{18}Fe_2N_{10}O_4P_3$
Formula weight	1780.14	1780.14	1780.14	1780.14
Temperature (K)	300.0(2)	305.0(2)	310.0(2)	315.0(2)
Crystal system	monoclinic	monoclinic	monoclinic	monoclinic
Space group	*P*2/n	*P*2/n	*P*2/n	*P*2/n
a (Å)	19.140(4)	19.140(4)	19.145(4)	19.144(4)
b (Å)	9.1170(18)	9.1200(18)	9.1220(18)	9.1260(18)
c (Å)	23.317(5)	23.307(5)	23.329(5)	23.352(5)
α (°)	90	90	90	90
β (°)	109.33(3)	109.29(3)	109.31(3)	109.33(3)
γ (°)	90	90	90	90
Volume (Å^3)	3839.5(15)	3840.1(15)	3845.1(15)	3849.8(15)
Z	2	2	2	2
ρ_{calc} (g/cm^3)	1.540	1.540	1.538	1.536
μ (mm^{-1})	0.543	0.543	0.542	0.541
F(000)	1830.0	1830.0	1830.0	1830.0
Crystal size (mm^3)	0.23 × 0.15 × 0.13	0.23 × 0.15 × 0.13	0.23 × 0.15 × 0.13	0.23 × 0.15 × 0.13
Radiation	Synchrotron (λ = 0.71092)	Synchrotron (λ = 0.71092)	Synchrotron (λ = 0.71092)	Synchrotron (λ = 0.71092)
2θ range for data collection (°)	3.358 to 64.352	3.358 to 64.206	3.356 to 64.324	3.356 to 64.284
Index ranges	-25 ≤ h ≤ 25, -11 ≤ k ≤ 11, -33 ≤ l ≤ 33	-25 ≤ h ≤ 25, -11 ≤ k ≤ 11, -33 ≤ l ≤ 32	-25 ≤ h ≤ 25, -11 ≤ k ≤ 11, -33 ≤ l ≤ 33	-25 ≤ h ≤ 25, -11 ≤ k ≤ 11, -33 ≤ l ≤ 33
Reflections collected	66037	52678	65072	64592
Independent reflections	11187 [R_{int} = 0.0600, R_{sigma} = 0.0397]	10573 [R_{int} = 0.0696, R_{sigma} = 0.0423]	11070 [R_{int} = 0.0606, R_{sigma} = 0.0412]	11077 [R_{int} = 0.0629, R_{sigma} = 0.0441]
Data/restraints/parameters	11187/396/602	10573/390/602	11070/390/602	11077/389/562
Goodness-of-fit on F^2	1.046	1.045	1.083	1.102
Final *R* indexes [$I \geq 2\sigma$ (*I*)]	R_1 = 0.0613, wR_2 = 0.1899	R_1 = 0.0639, wR_2 = 0.1927	R_1 = 0.0695, wR_2 = 0.2188	R_1 = 0.0756, wR_2 = 0.2468
Final *R* indexes [all data]	R_1 = 0.0710, wR_2 = 0.2055	R_1 = 0.0684, wR_2 = 0.2031	R_1 = 0.0760, wR_2 = 0.2330	R_1 = 0.0869, wR_2 = 0.2685
Largest diff. peak/hole (e Å^{-3})	0.37/-0.45	0.34/-0.51	0.46/-0.40	0.41/-0.49

Table S4. Crystallographic data and structure refinement parameters for compound **2**·3toluene·2MeCN at 325 and 350 K

	2·3toluene·2MeCN (325 K)	**2**·3toluene·2MeCN (350 K)
Empirical formula	$C_{82}H_{77}F_{18}Fe_2N_{10}O_4P_3$	$C_{79}H_{80}F_{18}Fe_2N_{10}O_4P_3$
Formula weight	1813.14	1780.14
Temperature (K)	325.0(2)	350.0(2)
Crystal system	monoclinic	monoclinic
Space group	*P*2/n	*P*2/n
a (Å)	19.151(4)	19.164(4)
b (Å)	9.1330(18)	9.1490(18)
c (Å)	23.366(5)	23.395(5)
α (°)	90	90
β (°)	109.32(3)	109.30(3)
γ (°)	90	90
Volume (Å^3)	3856.7(15)	3871.4(15)
Z	2	2
ρ_{calc} (g/cm^3)	1.561	1.527
μ (mm^{-1})	0.542	0.538
F(000)	1860.0	1830.0
Crystal size (mm^3)	0.23 × 0.15 × 0.13	0.23 × 0.15 × 0.13
Radiation	Synchrotron (λ = 0.71092)	Synchrotron (λ = 0.71092)
2θ range for data collection (°)	3.354 to 64.234	2.394 to 64.144
Index ranges	-25 ≤ h ≤ 25, -11 ≤ k ≤ 11, -33 ≤ l ≤ 33	-25 ≤ h ≤ 25, -11 ≤ k ≤ 11, -33 ≤ l ≤ 33
Reflections collected	64819	65246
Independent reflections	11113 [R_{int} = 0.0703, R_{sigma} = 0.0487]	11151 [R_{int} = 0.0793, R_{sigma} = 0.0525]
Data/restraints/parameters	11113/395/562	11151/389/562
Goodness-of-fit on F^2	1.053	1.089
Final *R* indexes [$I \geq 2\sigma(I)$]	R_1 = 0.0760, wR_2 = 0.2445	R_1 = 0.0874, wR_2 = 0.2787
Final *R* indexes [all data]	R_1 = 0.0889, wR_2 = 0.2682	R_1 = 0.1023, wR_2 = 0.3073
Largest diff. peak/hole (e Å^{-3})	0.42/-0.47	0.57/-0.47

Table S5. Crystallographic data and structure refinement parameters for compound **3**·2MeCN·3*i*Pr$_2$O at 100, 150, and 200 K.

	3·2MeCN·3*i*Pr$_2$O (100 K)	**3**·2MeCN·3*i*Pr$_2$O (150 K)	**3**·2MeCN·3*i*Pr$_2$O (200 K)
Empirical formula	$C_{76}H_{98}F_{24}Fe_2N_{10}O_7P_4$	$C_{76}H_{98}F_{24}Fe_2N_{10}O_7P_4$	$C_{76}H_{98}F_{24}Fe_2N_{10}O_7P_4$
Formula weight	1955.22	1955.22	1955.22
Temperature (K)	100.0(2)	150.0(2)	200.0(2)
Crystal system	monoclinic	monoclinic	monoclinic
Space group	$P2_1/c$	$P2_1/c$	$P2_1/c$
a (Å)	13.063(3)	13.087(3)	13.132(3)
b (Å)	31.109(6)	31.235(6)	31.410(6)
c (Å)	20.787(4)	20.849(4)	20.941(4)
α (°)	90	90	90
β (°)	102.02(3)	102.02(3)	101.76(3)
γ (°)	90	90	90
Volume (Å^3)	8262(3)	8336(3)	8456(3)
Z	4	4	4
ρ_{calc} (g/cm^3)	1.572	1.558	1.536
μ (mm^{-1})	0.543	0.538	0.530
F(000)	4032.0	4032.0	4032.0
Crystal size (mm^3)	0.2 × 0.16 × 0.15	0.2 × 0.16 × 0.15	0.2 × 0.16 × 0.15
Radiation	Synchrotron (λ = 0.71075)	Synchrotron (λ = 0.71075)	Synchrotron (λ = 0.71075)
2θ range for data collection (°)	2.392 to 57.408	2.386 to 57.39	2.372 to 57.358
Index ranges	-17 ≤ h ≤ 17, -35 ≤ k ≤ 35, -23 ≤ l ≤ 22	-17 ≤ h ≤ 17, -35 ≤ k ≤ 35, -23 ≤ l ≤ 22	-17 ≤ h ≤ 17, -36 ≤ k ≤ 36, -23 ≤ l ≤ 22
Reflections collected	103314	104132	105703
Independent reflections	15076 [R_{int} = 0.0461, R_{sigma} = 0.0244]	15189 [R_{int} = 0.0472, R_{sigma} = 0.0253]	15477 [R_{int} = 0.0518, R_{sigma} = 0.0270]
Data/restraints/parameters	15076/388/1083	15189/397/1062	15477/373/1062
Goodness-of-fit on F^2	1.081	1.045	1.040
Final R indexes [$I \geq 2\sigma$ (I)]	R_1 = 0.0599, wR_2 = 0.1716	R_1 = 0.0621, wR_2 = 0.1797	R_1 = 0.0629, wR_2 = 0.1848
Final R indexes [all data]	R_1 = 0.0631, wR_2 = 0.1745	R_1 = 0.0664, wR_2 = 0.1838	R_1 = 0.0686, wR_2 = 0.1903
Largest diff. peak/hole (e Å^{-3})	1.89/-0.61	1.82/-0.52	1.60/-0.39

Table S6. Crystallographic data and structure refinement parameters for compound **3**·2MeCN·3*i*Pr$_2$O at 250, 300 and 350 K.

	3·2MeCN·3*i*Pr$_2$O (250 K)	**3**·2MeCN·3*i*Pr$_2$O (300 K)	**3**·2MeCN·3*i*Pr$_2$O (350 K)
Empirical formula	$C_{76}H_{98}F_{24}Fe_2N_{10}O_7P_4$	$C_{76}H_{98}F_{24}Fe_2N_{10}O_7P_4$	$C_{76}H_{98}F_{24}Fe_2N_{10}O_7P_4$
Formula weight	1955.22	1955.22	1955.22
Temperature (K)	250.0(2)	300.0(2)	350.0(2)
Crystal system	monoclinic	monoclinic	monoclinic
Space group	$P2_1/c$	$P2_1/c$	$P2_1/c$
a (Å)	13.170(3)	13.191(3)	13.137(3)
b (Å)	31.605(6)	31.952(6)	32.215(6)
c (Å)	21.043(4)	21.133(4)	21.194(4)
α (°)	90	90	90
β (°)	101.47(3)	101.24(3)	100.89(3)
γ (°)	90	90	90
Volume (Å^3)	8584(3)	8736(3)	8808(3)
Z	4	4	4
ρ_{calc} (g/cm^3)	1.513	1.487	1.474
μ (mm^{-1})	0.523	0.513	0.509
F(000)	4032.0	4032.0	4032.0
Crystal size (mm^3)	0.2 × 0.16 × 0.15	0.2 × 0.16 × 0.15	0.2 × 0.16 × 0.15
Radiation	Synchrotron (λ = 0.71075)	Synchrotron (λ = 0.71075)	Synchrotron (λ = 0.71075)
2θ range for data collection (°)	2.358 to 57.452	2.342 to 57.37	2.33 to 57.38
Index ranges	-17 ≤ h ≤ 17, -36 ≤ k ≤ 36, -23 ≤ l ≤ 23	-17 ≤ h ≤ 17, -36 ≤ k ≤ 36, -23 ≤ l ≤ 23	-17 ≤ h ≤ 17, -37 ≤ k ≤ 37, -23 ≤ l ≤ 23
Reflections collected	107456	108109	108359
Independent reflections	15813 [R_{int} = 0.0521, R_{sigma} = 0.0266]	16107 [R_{int} = 0.0621, R_{sigma} = 0.0314]	15814 [R_{int} = 0.0621, R_{sigma} = 0.0339]
Data/restraints/parameters	15813/391/1062	16107/827/1191	15814/857/1190
Goodness-of-fit on F^2	1.036	1.051	1.020
Final R indexes [$I \geq 2\sigma$ (I)]	R_1 = 0.0672, wR_2 = 0.2058	R_1 = 0.0688, wR_2 = 0.2148	R_1 = 0.0761, wR_2 = 0.2372
Final R indexes [all data]	R_1 = 0.0746, wR_2 = 0.2160	R_1 = 0.0810, wR_2 = 0.2329	R_1 = 0.0991, wR_2 = 0.2659
Largest diff. peak/hole (e Å^{-3})	1.55/-0.41	1.30/-0.43	0.66/-0.29

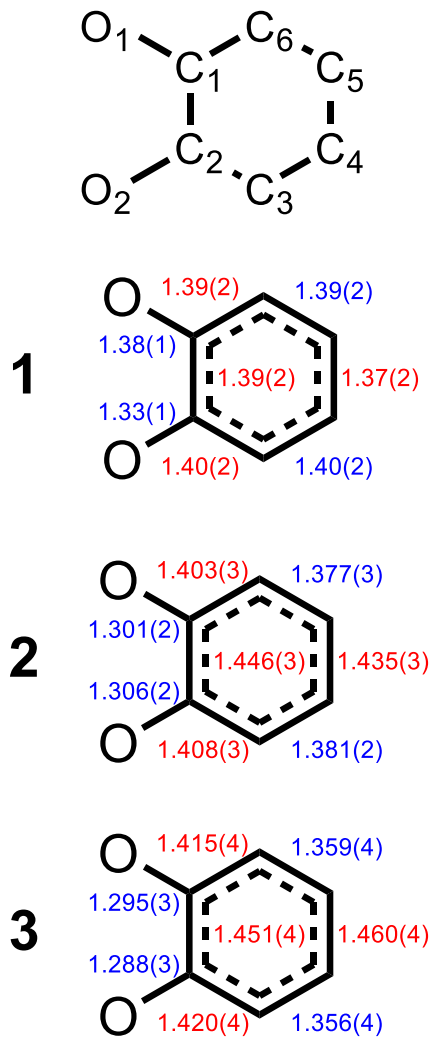

Figure S5. Average bond lengths of the dioxolene rings of thea^{n-} in **1**·Et$_2$O, **2**·3toluene·2MeCN, and **3**·2MeCN·3*i*Pr$_2$O at 100 K. Numbering scheme for atoms above. Bond lengths in blue contract upon oxidation from cat^{2-} to SQ$^{\bullet-}$, bond lengths in red elongate upon oxidation from cat^{2-} to SQ$^{\bullet-}$.

Infrared Spectroscopy

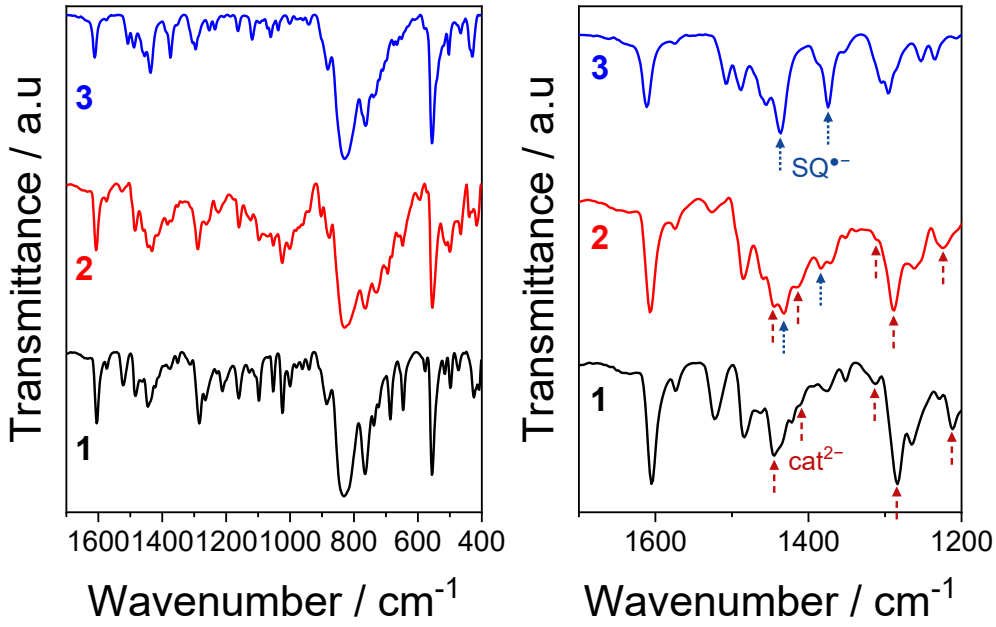

Figure S6. Room temperature ATR-IR spectra of **1**·2H_2O·0.5*i*Pr_2O, **2**·0.5toluene·3H_2O, and **3**·0.5MeCN in the region 1700 – 400 cm^{-1} (left) and 1700-1200 cm^{-1} highlighting catecholate and semiquinonate stretches (right).

Table S7. Selected IR (cm^{-1}) assignments of compounds **1**, **2**, and **3**

Moiety	and Assignment	1	2	3	Ref [a]
methyl	ν(C-H)	2959 (w), 2930 (w), 2855 (w)	2967 (w), 2922 (w), 2859 (w)	2967 (w), 2922 (w)	
tpa	ν(C=C)	1605 (s)	1607 (s)	1611 (m)	26
tpa	ν(C=N)	1574 (w)	1574 (w)	1574 (w)	26
SQ	ν(C-C)	-	1432 (s)	1436 (s)	27
SQ	ν(C=O) + ν(C=C) + δ(C-H)	-	1384 (m)	1374 (m)	26,28
cat	ν(C-O) + δ(C-H)	1445 (m)	1445 (m)	-	26
cat	ν(C=O) + ν(C=C) + δ(C-H)	1412 (sh)	1416 (w)	-	26
cat	ν(C-O) + ν(C=C) + ν(C-C)	1313 (m)	1311 (sh)	-	26,29
cat	skeletal diox	1284 (s)	1288 (s)	-	26,28,29
cat	ν(C-O) + ν(C-C)	1212 (m)	1224 (m)	-	26,29
PF_6^-	ν(P-F)	831 (vs)	829 (vs)	829 (vs)	30
PF_6^-	δ(P-F) + ν(P-F)	556 (s)	554 (s)	556 (s)	30

Intermolecular Interactions

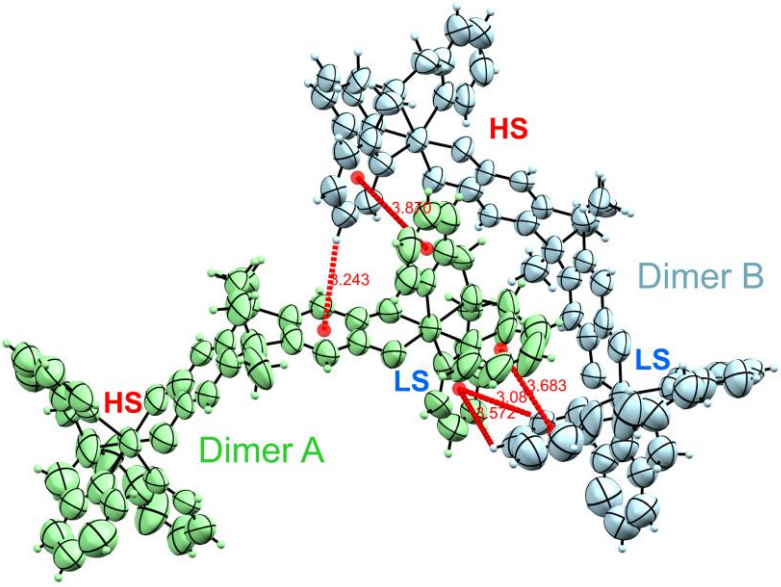

Figure S7. Intermolecular interactions highlighted in red between the two dimers in the asymmetric unit of **1**·Et_2O at 100 K. The dimers are labelled as A or B (with corresponding color) as discussed in the main text. The spin states of the Fe^{III} centers are labelled with LS or HS based on their Fe−N/O bond distances as discussed in main text (Table 1). Distances in Å.

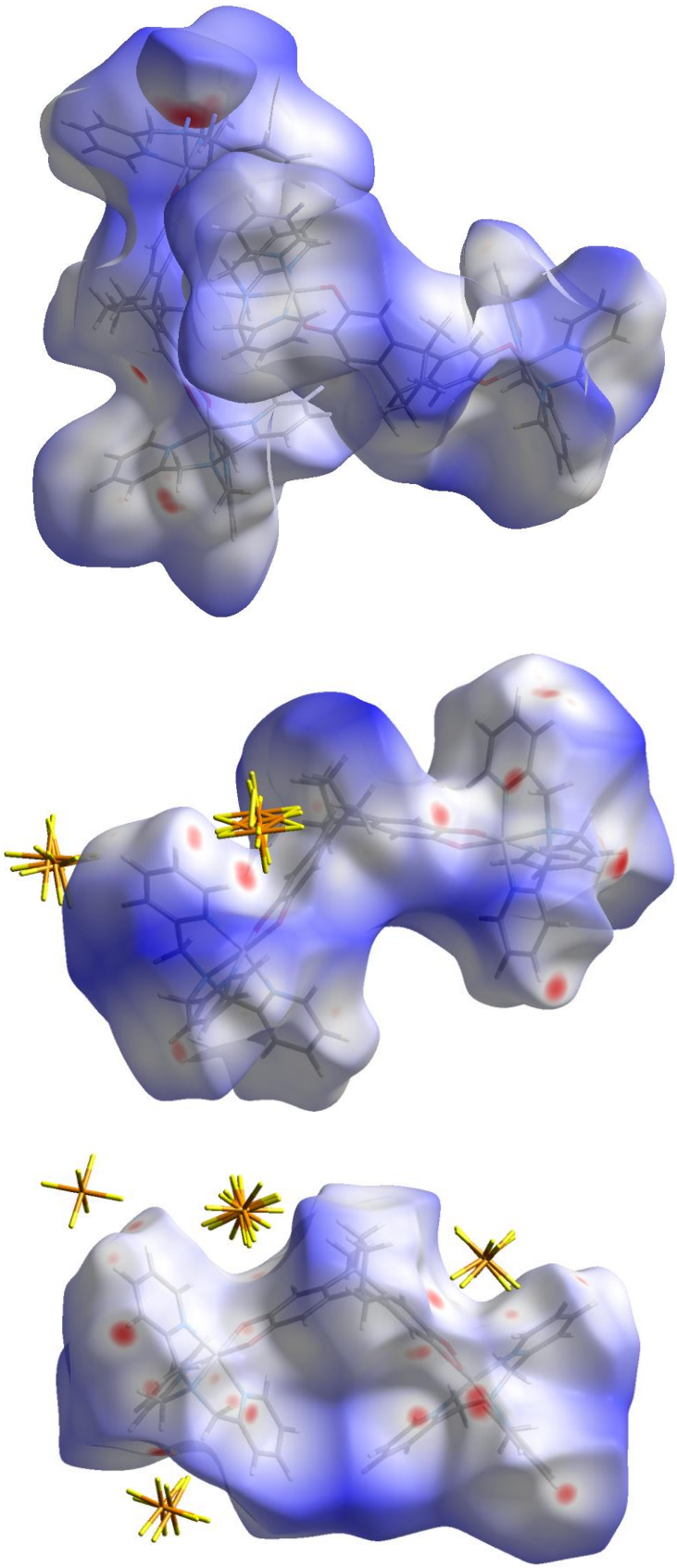

Figure S8. Hirshfeld surface mapped with d_{norm} for molecules A and B **1**·Et_2O (top), **2**·3toluene·2MeCN (middle), and **3**·2MeCN·3$i$$Pr_2O$ (bottom) at 100 K.

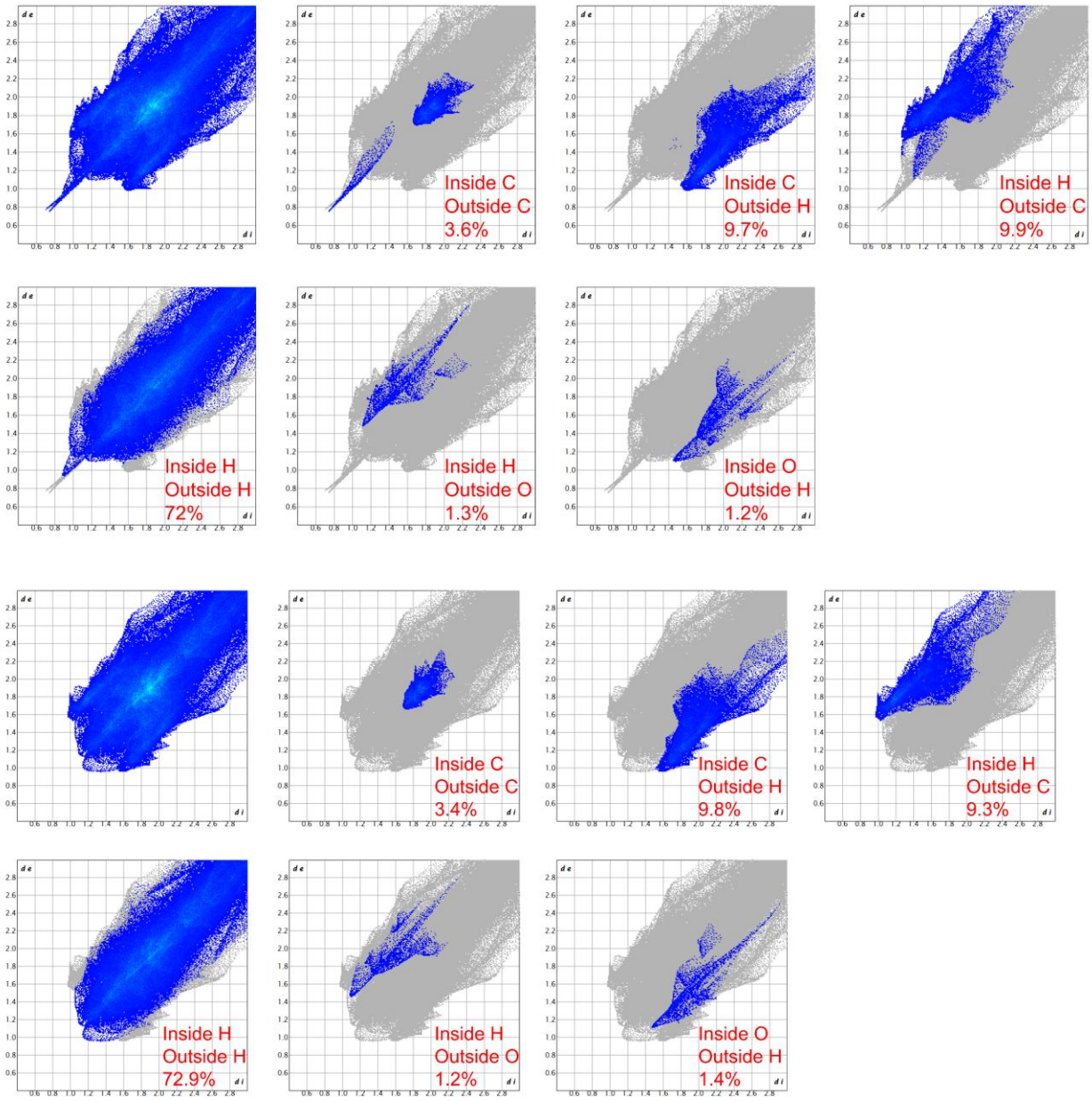

Figure S9. 2D fingerprint plots of all contacts, C···C, C···H/H··C, H···H, and H···O/O···H for molecule A (top two rows) and B (bottom two rows) in **1**·Et_2O at 100 K.

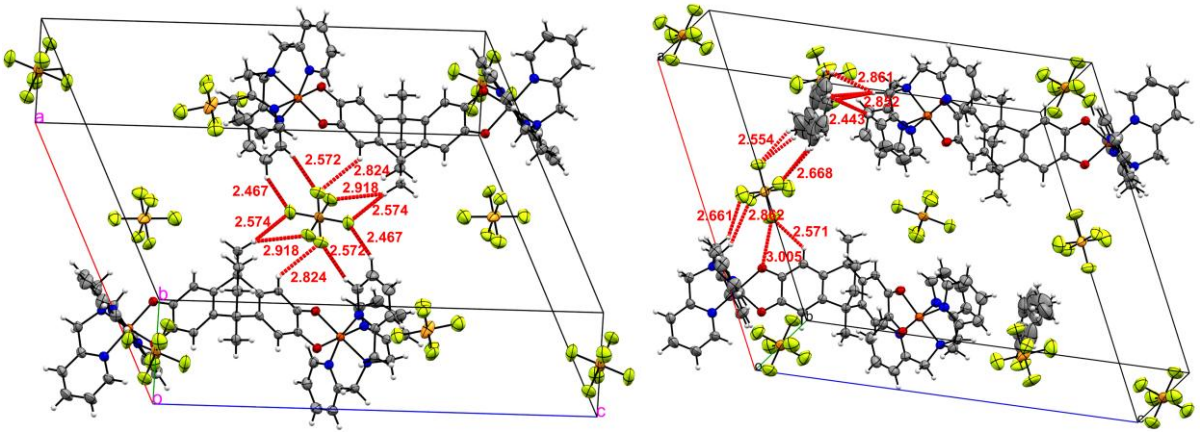

Figure S10. Intermolecular interactions in the unit cell of **2**·3toluene·2MeCN at 100 K. As the PF_6^- are disordered over three positions, the PF_6^- components with the closest intermolecular contacts are highlighted. Distances in Å.

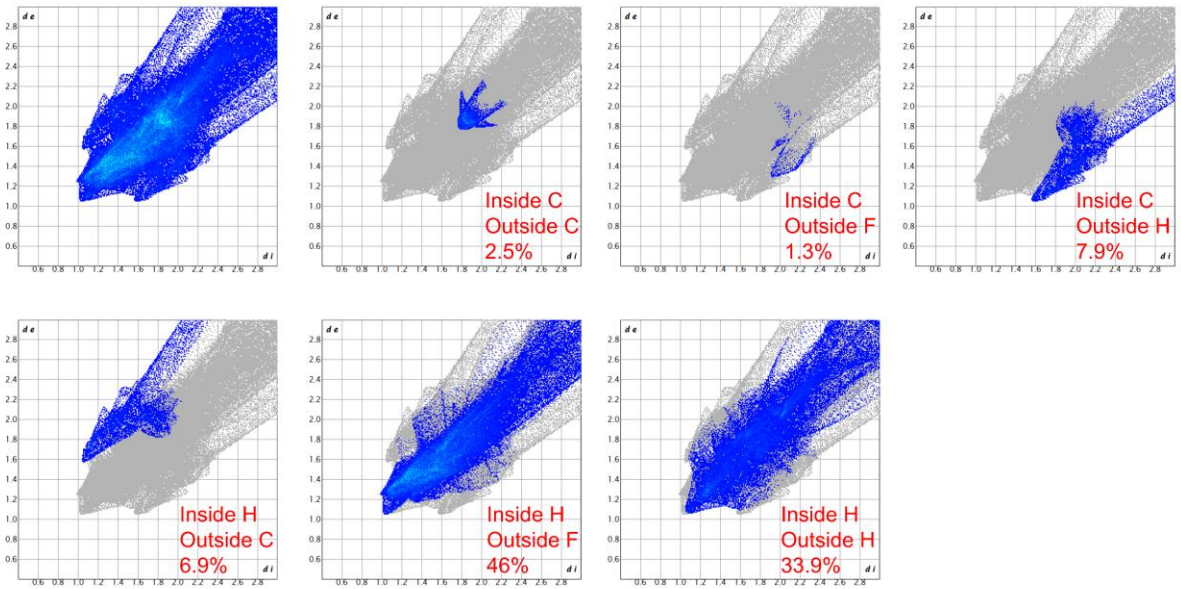

Figure S11. 2D fingerprint plots of all contacts, C···C, C···F, C···H/H··C, H···F, and H···H in **2**·3toluene·2MeCN at 100 K.

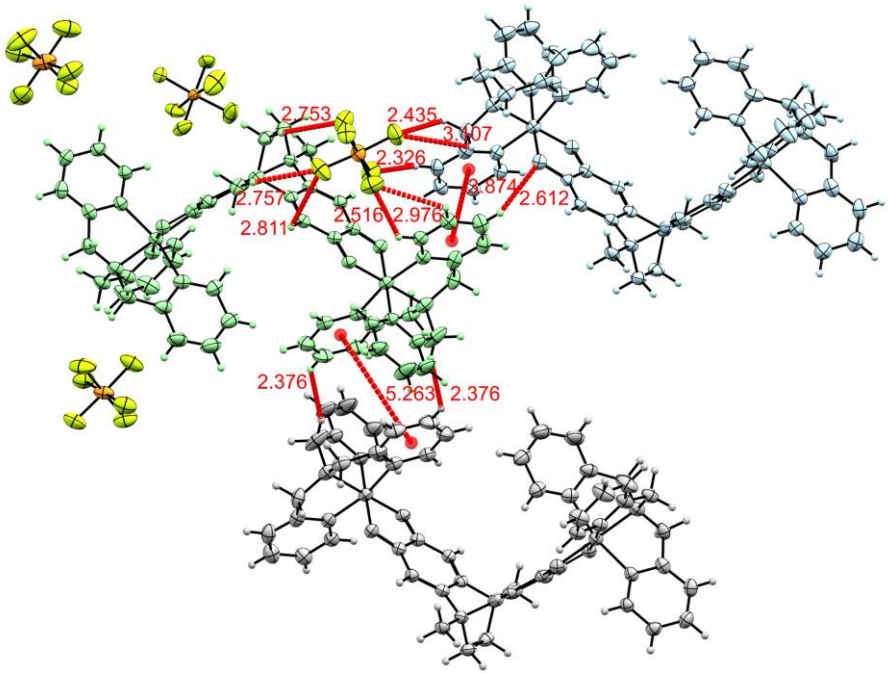

Figure S12. Intermolecular interactions in the structure of **3**·2MeCN·3*i*Pr$_2$O at 100 K. As the PF_6^- are disordered over three positions, the PF_6^- components with the closest intermolecular contacts are highlighted. Distances in Å.

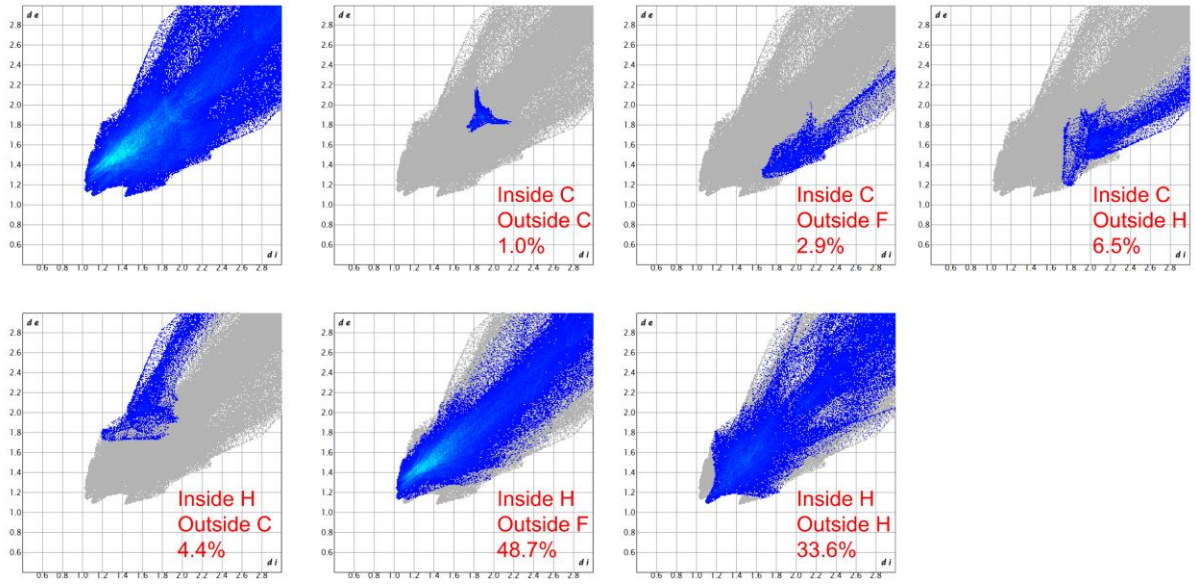

Figure S13. 2D fingerprint plots of all contacts, C···C, C···F, C···H/H··C, H···F, and H···H in **3**·2MeCN·3*i*Pr$_2$O at 100 K.

Mössbauer Spectroscopy

At 300 K, **1**·2H_2O·0.5*i*Pr_2O exhibits a broad asymmetric quadrupole doublet with isomer shift (δ) of 0.41 mm s^{-1} and quadrupole splitting (ΔE_Q) of 1.26 mm s^{-1} (Figure S14, Table S8). These parameters are similar to those for mononuclear HS-Fe^{III}-cat complexes,[31–34] indicating **1**·2H_2O·0.5*i*Pr_2O is [HS-HS] at room temperature. Compound **1**·2H_2O·0.5*i*Pr_2O remains [HS-HS] down to 250 K. Further cooling to 100 K is accompanied by formation of a second quadrupole doublet (δ = 0.39, ΔE_Q = 1.72 mm s^{-1}), with an accompanying decrease in relative area of the HS-Fe^{III} doublet. The ΔE_Q value of this new doublet is consistent with mononuclear LS-Fe^{III} -cat compounds (1.51–2.02 mm s^{-1}).[31–33,35] Notably, the δ value is larger than expected for LS-Fe^{III} -cat (0.20–0.29 mm s^{-1}).[31–33,35] The δ value is not consistent with HS-Fe^{II}-SQ (δ = 0.75–0.85 mm s^{-1}, ΔE_Q = 0.68–0.81 mm s^{-1}).[33] This new doublet could be arising from intermediate spin (IS)-Fe^{III} (δ = 0.32–0.37 mm s^{-1}).[34,36] However, solid- and solution-state EPR spectra discounts this (see Electron Paramagnetic Resonance Spectroscopy section). Alternatively, the large isomer shift can be explained by a LS-Fe^{III} state of **1** with Fe^{III}-cat/Fe^{II}-SQ quantum mixing, resulting in an average δ and ΔE_Q. This occurs as the electron transfer between the dioxolene and iron centers is faster than the Mössbauer experiment timescale (10^7–10^8 s^{-1}),[37,38] as shown with EPR measurements (see Electron Paramagnetic Resonance Spectroscopy, timescale 10^8–10^{10} s^{-1}). At 5.3 K, the two doublets are equal in area. Overall, Mössbauer spectroscopy shows **1** undergoes [LS-HS] ⇌ [HS-HS] SCO.

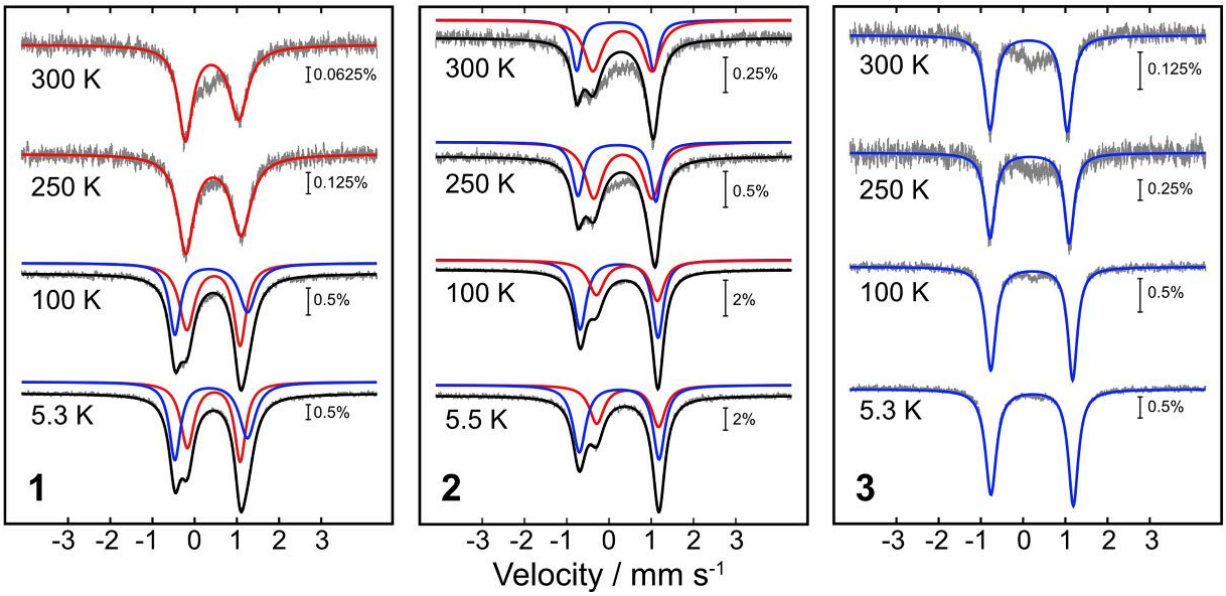

Figure S14. Variable temperature Mössbauer spectra of **1**·2H_2O·0.5*i*Pr_2O (left), **2**·0.5toluene·3H_2O (middle) and **3**·0.5MeCN (right). The black hashed is the raw data, and the solid lines (blue – LS-Fe^{III}, red – HS-Fe^{III}, black – overall fit) are the least-squares best fit.

Table S8. Selected ^{57}Fe Mössbauer fitted parameters of **1**·2H_2O·0.5*i*Pr_2O, **2**·0.5toluene·3H_2O and **3**·0.5MeCN at different temperatures.

Compound	T / K	δ / mm s^{-1}	ΔE_Q / mm s^{-1}	Γ_L / mm s^{-1}	Γ_R / mm s^{-1}	I / %	δ / mm s^{-1}	ΔE_Q / mm s^{-1}	Γ_L / mm s^{-1}	Γ_R / mm s^{-1}	I / %
		LS-Fe^{III}					HS-Fe^{III}				
1	300	-	-	-	-	0	0.41	1.26	0.41	0.54	100
	250	-	-	-	-	0	0.45	1.31	0.47	0.57	100
	100	0.39	1.72	0.33	0.46	44	0.45	1.26	0.44	0.36	56
	5.3	0.39	1.72	0.33	0.46	50	0.45	1.25	0.39	0.32	50
2	300	0.15	1.82	0.29	0.29	37	0.32	1.40	0.50	0.50	63
	250	0.19	1.84	0.33	0.30	39	0.33	1.38	0.50	0.50	61
	100	0.24	1.85	0.35	0.32	61	0.42	1.45	0.46	0.39	39
	5.5	0.24	1.89	0.37	0.34	61	0.44	1.46	0.42	0.39	39
3	300	0.13	1.83	0.31	0.31	100	-	-	-	-	0
	250	0.16	1.88	0.30	0.28	100	-	-	-	-	0
	100	0.20	1.94	0.30	0.27	100	-	-	-	-	0
	5.3	0.21	1.95	0.32	0.29	100	-	-	-	-	0

Solid-State Magnetic Data

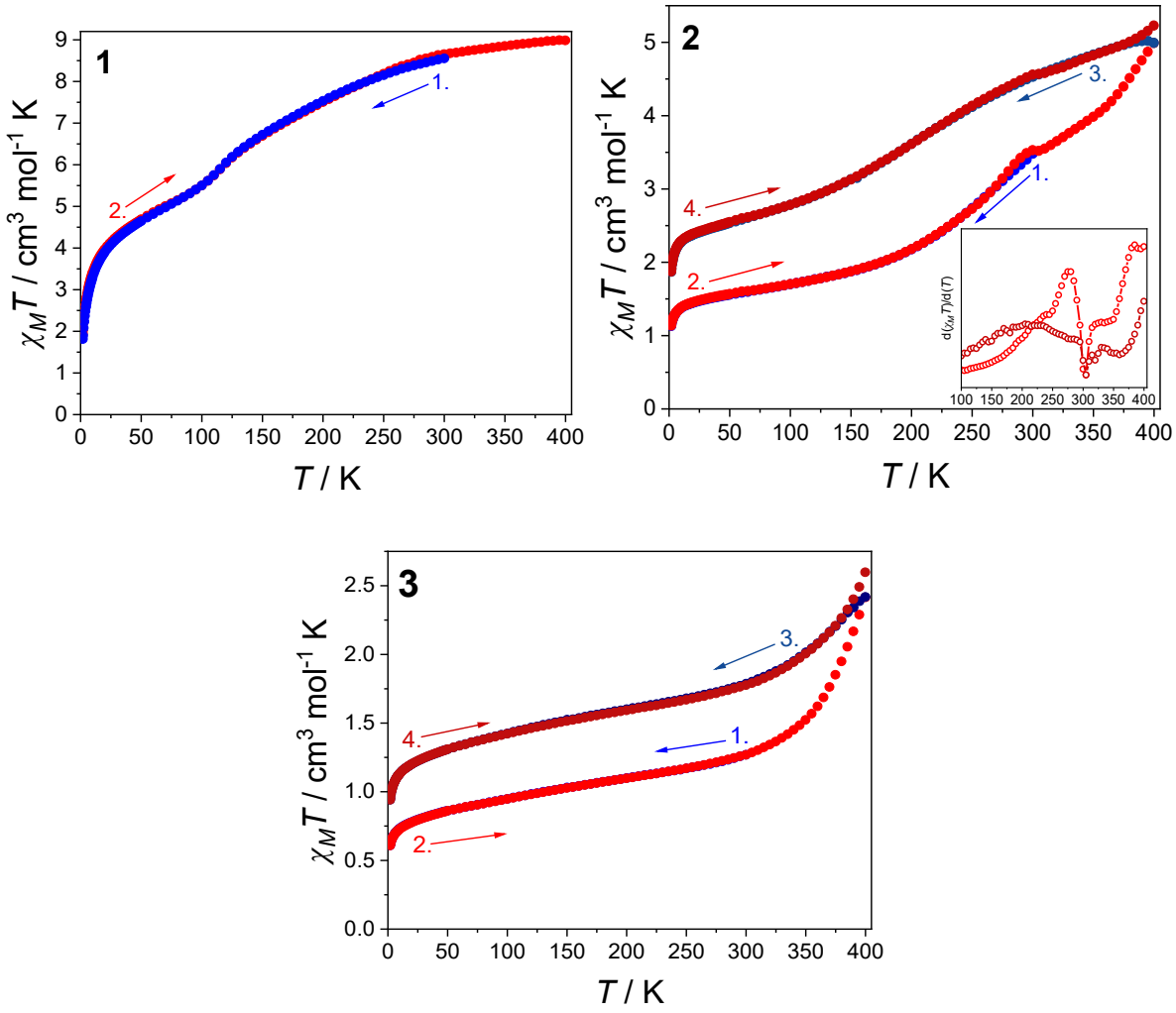

Figure S15. Plot of $\chi_M T$ vs T for **1**·2H$_2$O·0.5*i*Pr$_2$O on first cooling (blue circles) followed by heating (red circles) and plots of $\chi_M T$ vs T for **2**·0.5toluene·3H$_2$O and **3**·0.5MeCN on first cooling (blue circle), first heating (red circle), second cooling (dark blue crircle) and second heating (dark red circle). Arrows and numbers indicate direction and order of measurement. Bottom right inset: first derivative plot d($\chi_M T$)/d(T) for **2**·0.5toluene·3H$_2$O upon first heating (red) and second heating (dark red), highlighting the two-step SCO behavior and the plateau temperature.

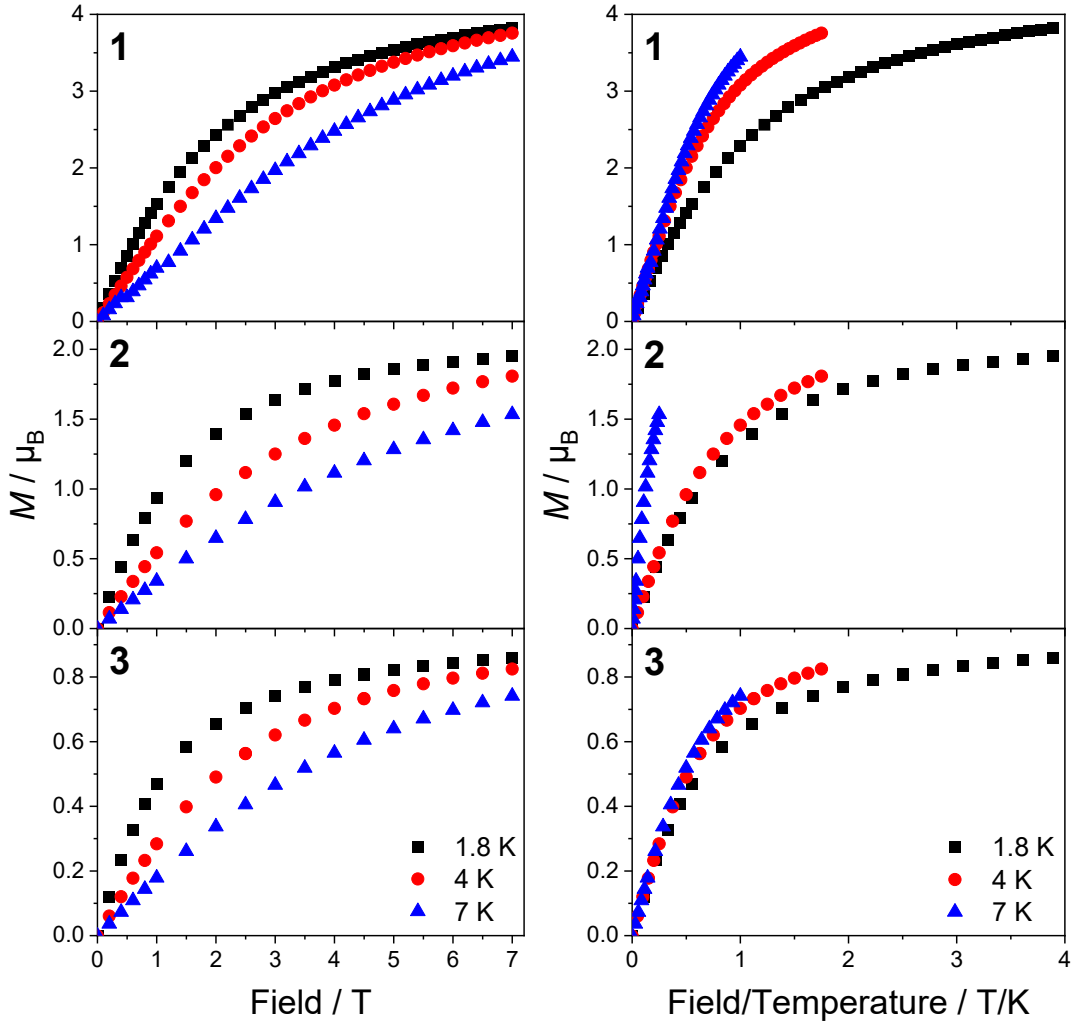

Figure S16. The field dependence of magnetization vs temperature (left) and the plot of magnetization vs field/temperature (right) for **1**·2H_2O·0.5*i*Pr_2O, **2**·0.5toluene·3H_2O and **3**·0.5MeCN at specified temperatures.

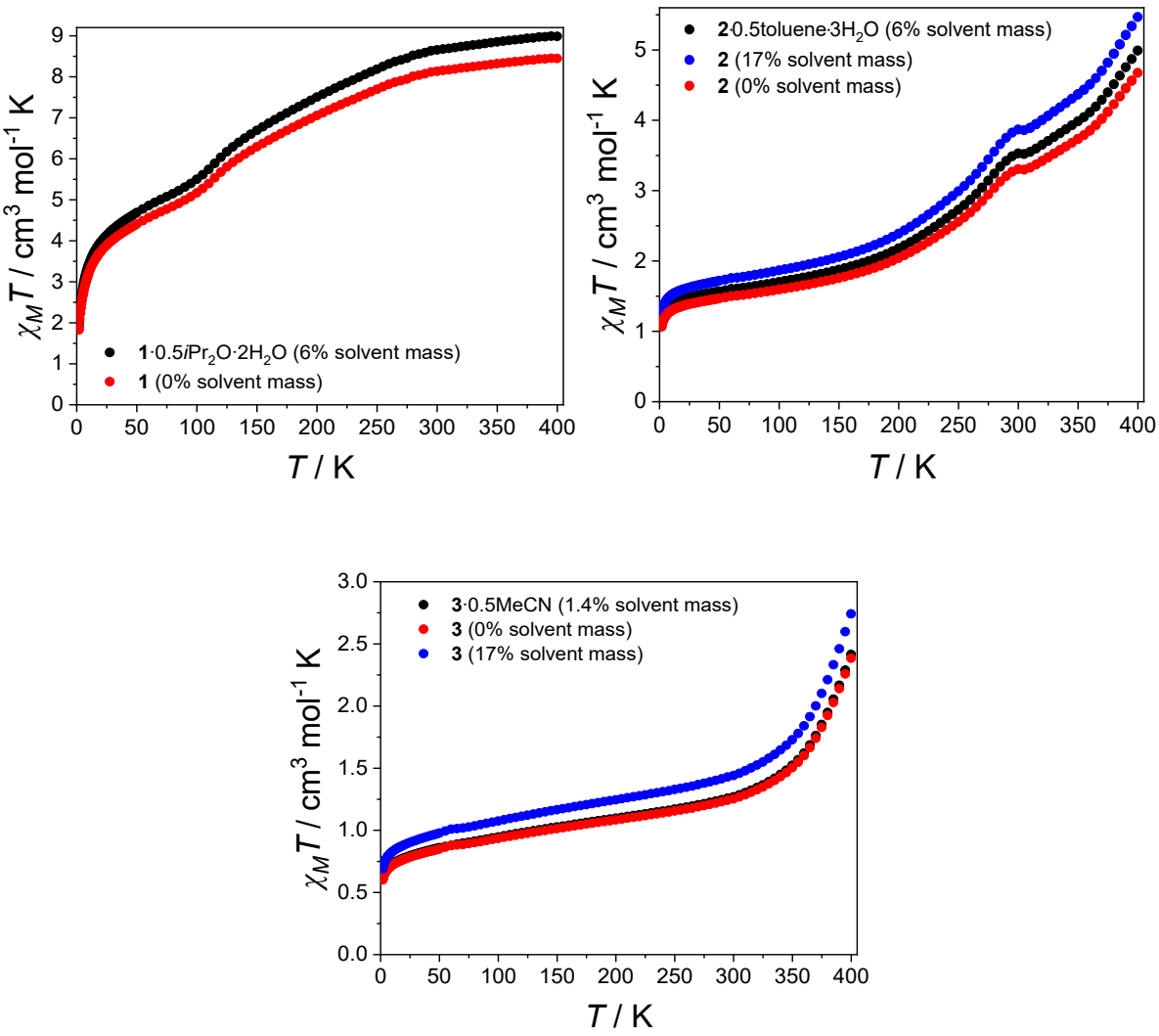

Figure S17. Plot of $\chi_M T$ vs T for **1**, **2** and **3** on first heating calculated using the solvation as determined from EA and TGA (black dots), assuming no solvation (red dots), and potential maximal solvation from TGA (blue dots). For **1** and **2**, the 'maximal solvation' was estimated from mass loss at 220 °C in TGA (Figure S2) which likely reflects decomposition rather than solvent, but is included for illustration. The small spread (~10%) demonstrates that conclusions remain valid despite solvation uncertainty.

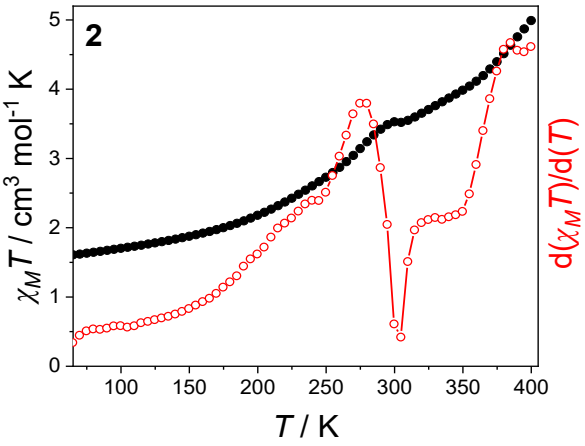

Figure S18. Plot of $\chi_M T$ vs T for **2**·0.5toluene·3H_2O on first heating (black filled circles) and the associated first derivatives (open red circles).

Table S9. Estimated percentages of the three different spin states at different temperature regimes form **2** based on the variable temperature magnetic susceptibility data

	Low-Temperature	Mid-Temperature	High-Temperature
	Assuming $\chi_M T$ of [LS-HS] state is 4.4 cm^3 mol^{-1} K		
[LS-LS]	85%	25%	25%
[LS-HS]	15%	75%	50%
[HS-HS	0%	0%	25%
	Assuming $\chi_M T$ of [LS-HS] state is 4.4 cm^3 mol^{-1} K		
[LS-LS]	85%	40%	40%
[LS-HS]	15%	60%	20%
[HS-HS	0%	0%	40%

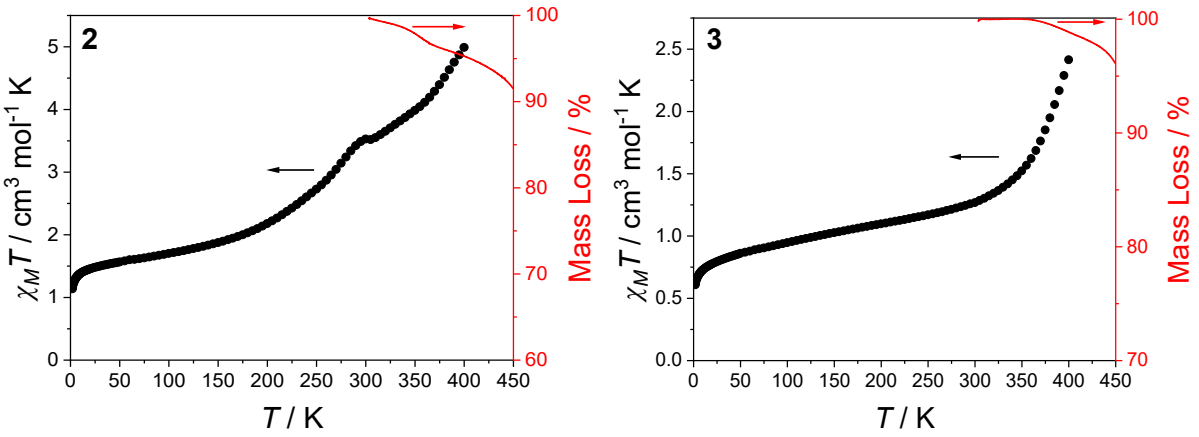

Figure S19. Plots of $\chi_M T$ (left axis, black circles) for **2**·0.5toluene·3H_2O and **3**·0.5MeCNsuperimposed with the thermogravimetric analysis data (right axis, red line).

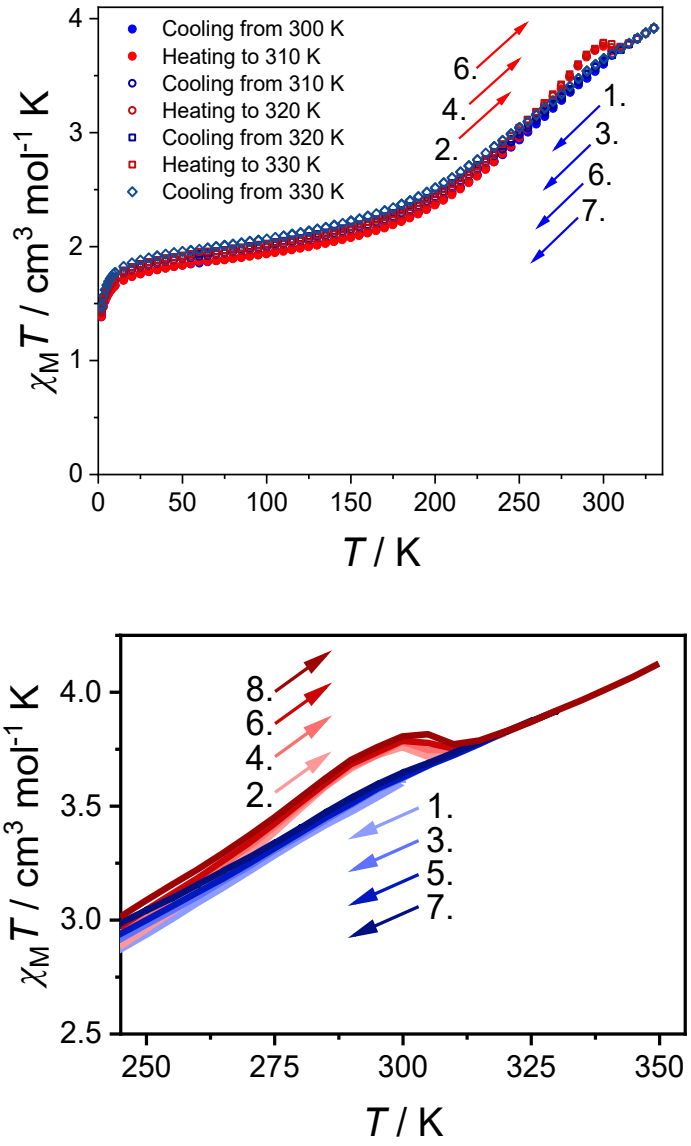

Figure S20. Top: plot of $\chi_M T$ vs T for **2**·0.5toluene·3H_2O successive cooling/heating cycles overlayed following: cooling from 300 – 1.8 K (Cycle 1), heating from 1.8 – 310 K (cycle 2), cooling from 310 – 1.8 K (cycle 3), heating from 1.8 – 320 K (cycle 4), cooling from 320 – 1.8 K (cycle 5), heating from 1.8 – 330 K (cycle 6), cooling from 330 K – 1.8 K (cycle 7). Bottom: plot of $\chi_M T$ vs T for **2**·0.5toluene·3H_2O successive cooling/heating cycles in the plateau region: cooling from 300 – 1.8 K (Cycle 1), heating from 1.8 – 310 K (cycle 2), cooling from 310 – 1.8 K (cycle 3), heating from 1.8 – 320 K (cycle 4), cooling from 320 – 1.8 K (cycle 5), heating from 1.8 – 330 K (cycle 6), cooling from 330 K – 1.8 K (cycle 7), heating from 1.8 – 250 K (cycle 8).

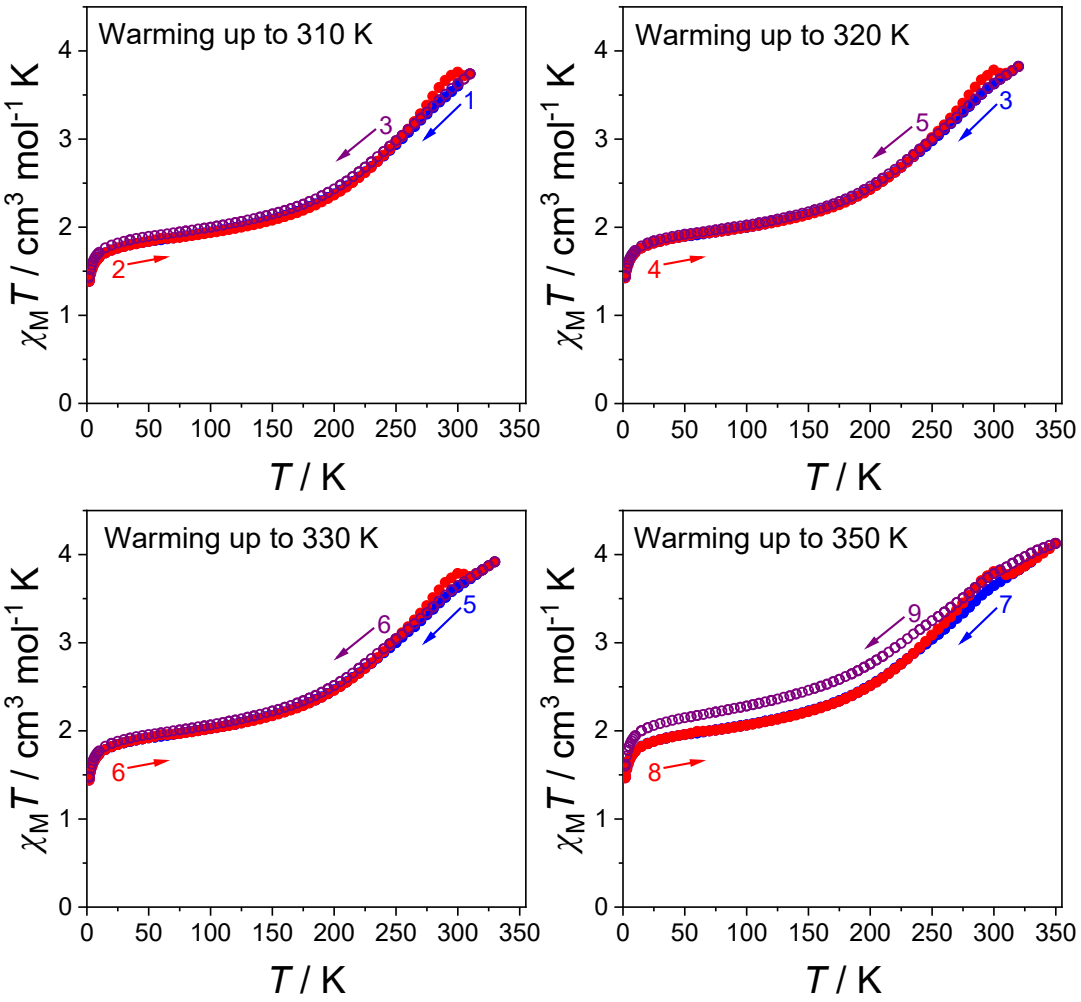

Figure S21. Plot of $\chi_M T$ vs T for **2**·0.5toluene·3H_2O for various continuous temperature cycles. Top left: cooling from 300 – 1.8 K (blue circles), heating from 1.8 – 310 K (red circles), cooling from 310 – 1.8 K (open purple circles). Top right: cooling from 310 – 1.8 K (blue circles), heating from 1.8 – 320 K (red circles), cooling from 320 – 1.8 K (open purple circles). Bottom left: cooling from 330 – 1.8 K (blue circles), heating from 1.8 – 350 K (red circles), cooling from 350 – 1.8 K (open purple circles). Bottom right: cooling from 300 – 1.8 K (blue circles), heating from 1.8 – 310 K (red circles), cooling from 310 – 1.8 K (open purple circles). Arrows and numbers indicate direction and order of measurement. Cycle numbering: cooling from 300 K (1), heating to 310 K (2), cooling from 310 K (3), heating to 320 K (4), cooling from 320 K (5), heating to 330 K (6), cooling from 330 K (7), heating to 350 K (8), cooling from 350 K (9).

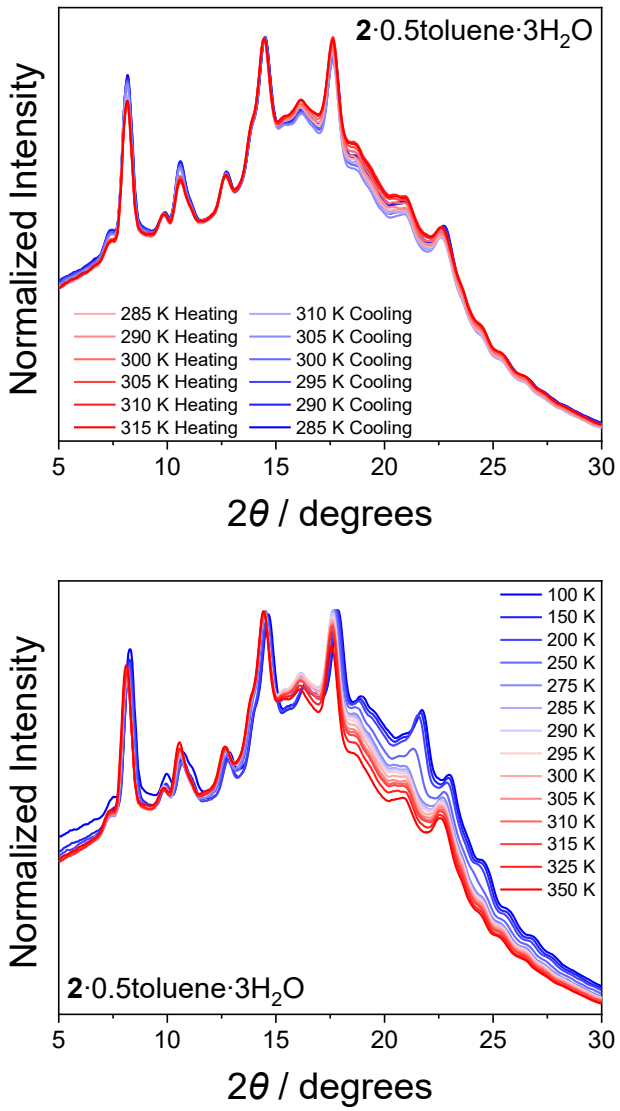

Figure S22. Experimental PXRD pattern of **2**·0.5toluene·3H_2O collected at 100, 150, 200, 250, 275, 285, 290, 295, 300, 305, 310, 315, 325 and 350 K (heating).

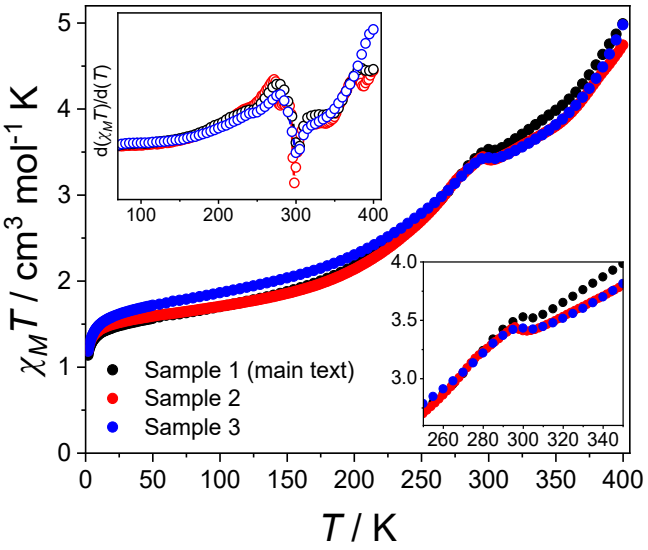

Figure S23. Plot of $\chi_M T$ vs T for compound **2** samples 1 (discussed in main text, black circles), 2 (red circles) and 3 (blue circles) on first heating. Top left inset: first derivative plot d($\chi_M T$)/d(T) for **2** samples 1 (open black circles), 2 (open red circles) and 3 (open blue circles) highlighting the two-step SCO behavior and the plateau temperature. Bottom right inset: Illustration of plateau region centered between 295 – 305 K.

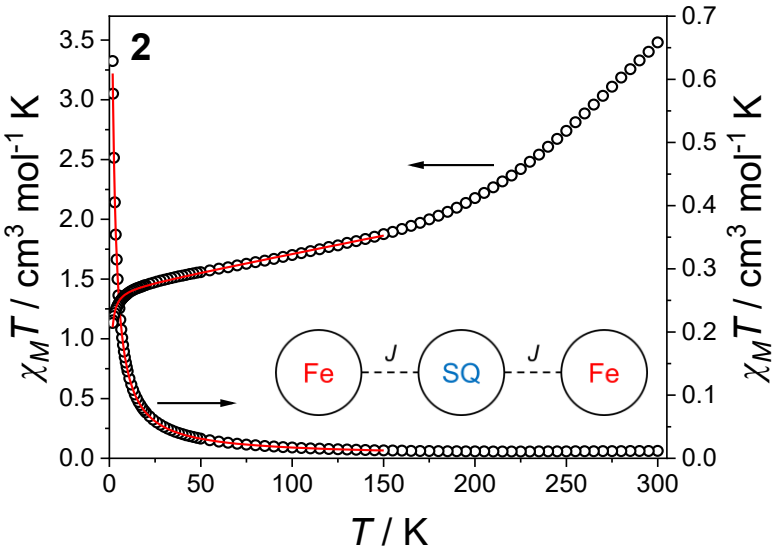

Figure S24. Plots of $\chi_M T$ vs T for **2**·0.5toluene·3H_2O on first cooling (open circles) with fit (red line) with $J = -0.56(1)$ cm^{-1}, TIP = 3.35(3) $\times 10^{-3}$ cm^3 mol^{-1} and ρ ($S = 5/2$) = 8.72(7)% using the Heisenberg exchange $\hat{H}_{ex} = -2J(\hat{S}_{Fe1} \cdot \hat{S}_{SQ} + \hat{S}_{Fe2} \cdot \hat{S}_{SQ})$, where $\hat{S}_{SQ}$ is the $SQ^{\bullet -}$ spin center and $\hat{S}_{Fe1}$ and $\hat{S}_{Fe2}$ are the two LS-Fe^{III} spin centers, assuming $g = 2.0$ for all spins, and J is the exchange interaction between the LS-Fe^{III} centers and $SQ^{\bullet -}$ in *PHI*.[15] Inset is the magnetic coupling diagram.

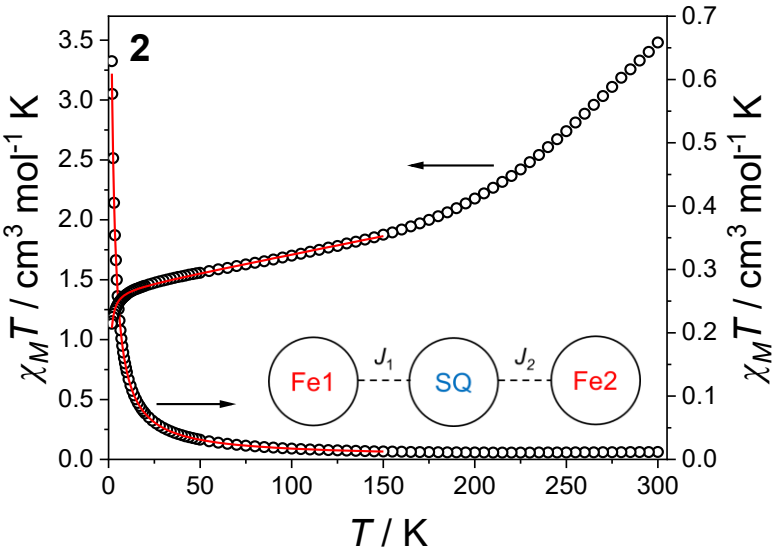

Figure S25. Plots of $\chi_M T$ vs T for **2**·0.5toluene·3H_2O on first cooling (open circles) with fit (red line) with $J_1 = -0.56(7)$ cm^{-1}, $J_2 = -0.56(7)$ cm^{-1}, TIP = 3.35(3) ×10^{-3} cm^3 mol^{-1} and ρ ($S = 5/2$) = 8.72(7)% using the Heisenberg exchange Hamiltonian $\hat{H}_{ex} = -2J_1(S_{SQ} \cdot S_{Fe1}) - 2J_2(S_{SQ} \cdot S_{Fe2})$ where J_1 is the exchange interactions between the $SQ^{\bullet-}$ spin center and one LS-Fe^{III} spin center (S_{Fe1}) and J_2 is the exchange interactions between the $SQ^{\bullet-}$ spin center and the other LS-Fe^{III} spin center (S_{Fe2}), with g = 2.0 fixed for all spins using *PHI*.[15] Inset is the magnetic coupling diagram.

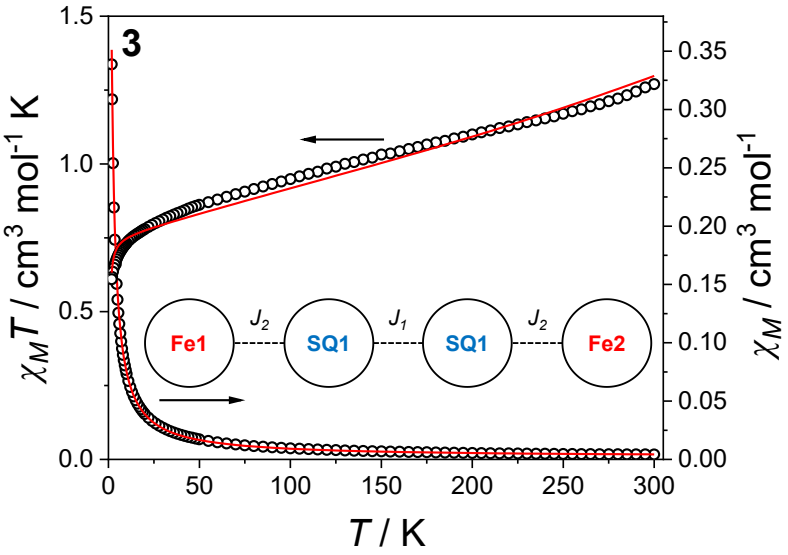

Figure S26. Plot of $\chi_M T$ vs T for **3**·0.5MeCN on first cooling (open circles) with fit (red line) with J_1 = −430(20) cm^{-1}, J_2 = −17.1(7) cm^{-1}, and TIP = 1.69(2) × 10^{-3} cm^3 mol^{-1} using the Heisenberg exchange Hamiltonian $\hat{H}_{ex} = -2J_1(S_{SQ1}\cdot S_{SQ2}) - 2J_2(S_{Fe1}\cdot S_{SQ2} + S_{Fe2}\cdot S_{SQ2})$, where J_1 is the exchange interactions between the two (S = 1/2) SQ$^{\bullet-}$ spin centers and J_2 is the exchange interactions between the LS-Fe^{III} center and the directly coordinated SQ$^{\bullet-}$ spin center, with g = 2.0 fixed for all spins using *PHI*.[15] Inset is the magnetic coupling diagram.

Variable Temperature Crystallography

Table S10. Selected Interatomic Distances (Å) and Distortion Parameters for **2**·3toluene·2MeCN at 100, 150, 200, 250, 275, 285, 290, 295, 300, 305, 310, 315, 325 and 350 K.

	2·3toluene·2MeCN													
	100 K	150 K	200 K	250 K	275 K	285 K	290 K	295 K	300 K	305 K	310 K	315 K	325 K	350 K
	Interatomic Distances / Å													
$Fe_1–O_1$	1.885(1)	1.886(1)	1.884(1)	1.887(1)	1.890(1)	1.893(1)	1.893(1)	1.894(2)	1.890(1)	1.894(2)	1.897(2)	1.897(2)	1.898(2)	1.905(2)
$Fe_1–O_2$	1.891(1)	1.891(1)	1.889(1)	1.893(1)	1.899(1)	1.900(1)	1.903(1)	1.900(2)	1.905(1)	1.901(2)	1.903(2)	1.905(2)	1.902(2)	1.907(2)
$Fe–O_{av}$	1.888(1)	1.889(1)	1.887(1)	1.890(1)	1.895(1)	1.897(1)	1.898(1)	1.897(3)	1.898(1)	1.898(3)	1.900(3)	1.901(3)	1.900(3)	1.906(3)
$Fe_1–N_1$	1.992(1)	1.989(1)	1.989(1)	2.007(1)	2.023(1)	2.032(1)	2.034(1)	2.031(2)	2.034(1)	2.034(2)	2.038(2)	2.044(2)	2.045(2)	2.050(2)
$Fe_1–N_2$	1.936(2)	1.937(1)	1.942(1)	1.957(2)	1.972(2)	1.981(2)	1.986(2)	1.981(2)	1.990(2)	1.986(2)	1.991(2)	1.997(2)	2.029(2)	2.007(3)
$Fe_1–N_3$	1.963(2)	1.964(1)	1.968(1)	1.984(2)	1.997(2)	2.006(2)	2.010(2)	2.004(2)	2.013(2)	2.014(2)	2.028(2)	2.021(2)	2.033(2)	2.040(3)
$Fe_1–N_4$	1.971(1)	1.973(1)	1.976(1)	1.991(2)	2.008(2)	2.018(2)	2.020(2)	2.017(2)	2.018(2)	2.023(2)	2.033(2)	2.030(2)	2.034(2)	2.041(2)
$Fe–N_{av}$	1.966(2)	1.966(2)	1.969(2)	1.985(4)	2.000(4)	2.009(4)	2.013(4)	2.008(4)	2.014(4)	2.014(4)	2.023(4)	2.023(4)	2.028(4)	2.035(4)
$Fe–O/N_{av}$	1.940(3)	1.941(2)	1.942(2)	1.953(4)	1.966(4)	1.972(4)	1.974(4)	1.971(5)	1.975(4)	1.975(5)	1.982(5)	1.983(5)	1.985(5)	1.992(5)
$C_1–O_1$	1.307(2)	1.303(2)	1.304(2)	1.304(2)	1.308(2)	1.310(2)	1.311(2)	1.311(2)	1.315(2)	1.313(2)	1.310(2)	1.314(3)	1.314(3)	1.312(3)
$C_2–O_2$	1.301(2)	1.303(2)	1.301(2)	1.300(2)	1.302(2)	1.303(2)	1.302(2)	1.298(2)	1.304(2)	1.301(2)	1.302(2)	1.307(3)	1.305(3)	1.313(3)
Fe···Fe	10.910(2)	10.920(3)	10.922(3)	10.947(3)	10.961(2)	10.969(2)	10.970(2)	10.955(2)	10.965(2)	10.958(2)	10.962(2)	10.970(2)	10.972(2)	10.974(2)
r_{ab} [a]	7.385(2)	7.390(2)	7.396(2)	7.412(2)	7.418(2)	7.422(2)	7.421(2)	7.411(2)	7.420(2)	7.412(2)	7.414(2)	7.419(3)	7.419(3)	7.419(3)
	Distortion Parameters													
SHAPE (O_h)[b]	0.462	0.471	0.484	0.550	0.618	0.650	0.674	0.654	0.674	0.676	0.683	0.715	0.730	0.759
Σ/° [c]	48.6	49.0	49.7	53.8	57.5	59.4	60.1	59.6	60.5	60.3	60.7	62.6	63.2	65.6
Θ/° [c]	141.9	143.3	145.1	155.0	164.7	169.2	171.7	169.5	172.9	172.1	173.2	177.3	178.4	181.5
θ/° [d]	114.6(4)	114.82(5)	115.05(9)	115.5(1)	115.76(9)	115.95(4)	116.0(2)	115.4(1)	115.88(5)	115.56(8)	115.57(5)	115.75(8)	115.78(8)	115.8(1)
MOS [e]	−1.22(9)	−1.20(9)	−1.20(9)	−1.2(1)	−1.2(1)	−1.2(1)	−1.3(1)	−1.2(1)	−1.3(1)	−1.2(1)	−1.2(1)	−1.3(2)	−1.3(1)	−1.3(2)

[a]Average distance (Å) between the two O-C-C-O centroids. [b]*SHAPE* index for octahedral geometry in SHAPE 2.1.[39,40] A value of 0 represents a perfect octahedron. [c]∑ = sum of the deviation of the 12 N/O−Co−N/O angles from 90°. Θ = sum of the deviation of 24 unique torsional angles between the N/O atoms on opposite triangular faces of the octahedron from 60°, providing the degree of trigonal distortion from an octahedron to trigonal prism. These were calculated using OctaDist - a program for determining the structural distortion of the octahedral complexes. For a perfect octahedron, ∑ and Θ are zero.[41] [d]Dihedral angle between the least square planes of the thea^{n-} dioxolene rings. [e]Dioxolene metrical oxidation state as defined by Brown.[42]

Table S11. Selected Interatomic Distances (Å) and Distortion Parameters for **3**·2MeCN·3*i*Pr$_2$O at 100, 150, 200, 250, 300 and 350 K.

	3·2MeCN·3*i*Pr$_2$O											
	100 K		150 K		200 K		250 K		300 K		350 K	
	Fe1	Fe2	Fe1	Fe2	Fe1	Fe2	Fe1	Fe2	Fe1	Fe2	Fe1	Fe2
	Interatomic Distances / Å											
$Fe_1–O_1/Fe_2–O_3$	1.868(2)	1.863(2)	1.873(3)	1.880(3)	1.872(2)	1.866(2)	1.876(2)	1.868(2)	1.866(2)	1.869(2)	1.861(2)	1.864(2)
$Fe_1–O_2/Fe_2–O_4$	1.910(2)	1.906(2)	1.910(4)	1.915(4)	1.907(2)	1.911(2)	1.902(2)	1.906(2)	1.903(2)	1.909(2)	1.901(2)	1.907(2)
$Fe–O_{av}$	1.889(3)	1.885(3)	1.892(5)	1.898(5)	1.890(3)	1.889(3)	1.889(3)	1.887(3)	1.885(3)	1.889(3)	1.881(3)	1.886(3)
$Fe_1–N_1/Fe_2–N_5$	1.982(3)	1.975(3)	1.944(4)	1.987(4)	1.982(3)	1.973(3)	1.981(2)	1.976(2)	1.985(3)	1.971(3)	1.975(3)	1.975(3)
$Fe_1–N_2/Fe_2–N_6$	1.941(2)	1.935(2)	1.941(4)	1.949(4)	1.944(2)	1.936(3)	1.948(2)	1.941(2)	1.950(3)	1.939(3)	1.936(3)	1.941(3)
$Fe_1–N_3/Fe_2–N_7$	1.952(3)	1.948(3)	1.938(5)	1.988(5)	1.953(3)	1.951(3)	1.949(2)	1.950(3)	1.948(3)	1.947(3)	1.934(4)	1.946(3)
$Fe_1–N_4/Fe_2–N_8$	1.957(3)	1.956(3)	1.960(5)	1.966(5)	1.954(3)	1.962(3)	1.961(2)	1.958(3)	1.973(3)	1.973(3)	1.990(4)	1.961(4)
$Fe–N_{av}$	1.958(6)	1.954(6)	1.946(9)	1.973(9)	1.958(6)	1.956(6)	1.960(4)	1.956(4)	1.964(6)	1.958(6)	1.959(7)	1.956(7)
$Fe–O/N_{average}$	1.935(6)	1.931(6)	1.93(1)	1.95(1)	1.935(6)	1.934(6)	1.936(5)	1.933(6)	1.938(7)	1.935(7)	1.933(8)	1.933(8)
$C_1–O_1/C_3–O_3$	1.293(3)	1.298(3)	1.301(6)	1.291(6)	1.288(3)	1.291(3)	1.283(3)	1.291(3)	1.270(3)	1.282(3)	1.291(4)	1.280(4)
$C_2–O_2/C_4–O4$	1.291(3)	1.281(3)	1.309(6)	1.297(6)	1.286(3)	1.288(3)	1.295(3)	1.292(3)	1.288(3)	1.287(4)	1.296(4)	1.268(4)
Fe···Fe	10.215(4)		10.272(4)		10.254(4)		10.277(4)		10.306(4)		10.348(4)	
r_{ab} [a]	7.259(3)		7.285(6)		7.289(3)		7.309(3)		7.328(3)		7.352(4)	
	Distortion Parameters											
SHAPE (O_h)[b]	0.424	0.477	0.426	0.458	0.457	0.521	0.471	0.527	0.477	0.533	0.505	0.541
Σ/° [c]	46.2	53.6	45.9	53.5	49.2	56.6	50.3	56.8	51.5	56.5	52.7	56.1
Θ/° c	138.5	144.9	138.1	142.1	144.4	150.9	146.2	151.8	147.0	152.5	149.3	154.1
θ/° [a]	111.1(1)		111.0(1)		112.0(3)		112.7(2)		113.0(2)		114.1(2)	
MOS [d]	−1.0(2)	−0.9(1)	−1.0(2)	−1.0(2)	−0.9(1)	−0.9(1)	−1.0(1)	−1.0(1)	−1.1(1)	−0.9(1)	−1.1(1)	−0.8(2)

[a]Average distance (Å) between the two O-C-C-O centroids. [b]*SHAPE* index for octahedral geometry in SHAPE 2.1.[39,40] A value of 0 represents a perfect octahedron. [c]∑ = sum of the deviation of the 12 N/O−Co−N/O angles from 90°. Θ = sum of the deviation of 24 unique torsional angles between the N/O atoms on opposite triangular faces of the octahedron from 60°, providing the degree of trigonal distortion from an octahedron to trigonal prism. These were calculated using OctaDist - a program for determining the structural distortion of the octahedral complexes. For a perfect octahedron, ∑ and Θ are zero.[41] [d]Dihedral angle between the least square planes of the thea^{n-} dioxolene rings. [e]Dioxolene metrical oxidation state as defined by Brown.[42]

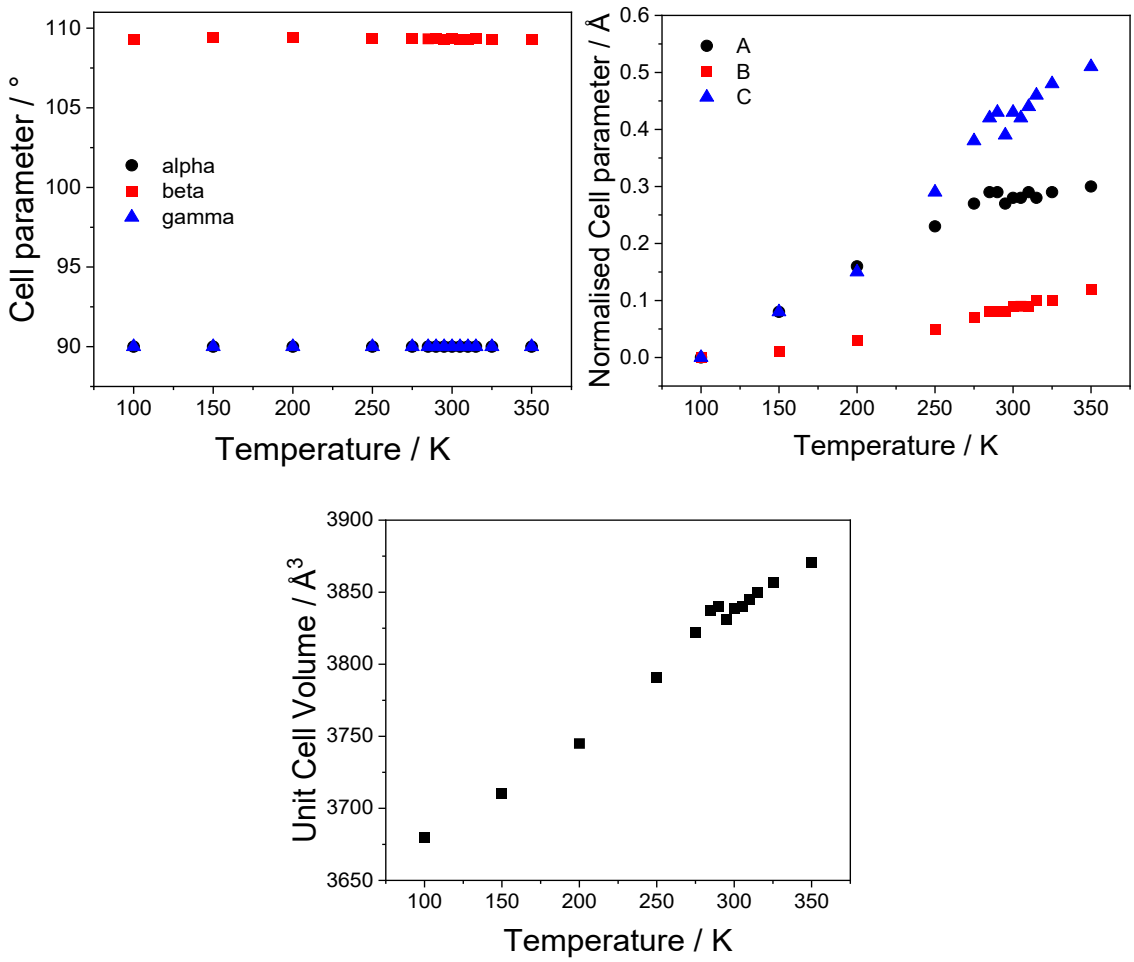

Figure S27. Temperature dependence of $a/a_{300\ K}$, $b/b_{300\ K}$ and $c/c_{300\ K}$ cell parameters, α, β and γ cell parameters, and unit cell $V/V_{300\ K}$ in **2**·3toluene·2MeCN.

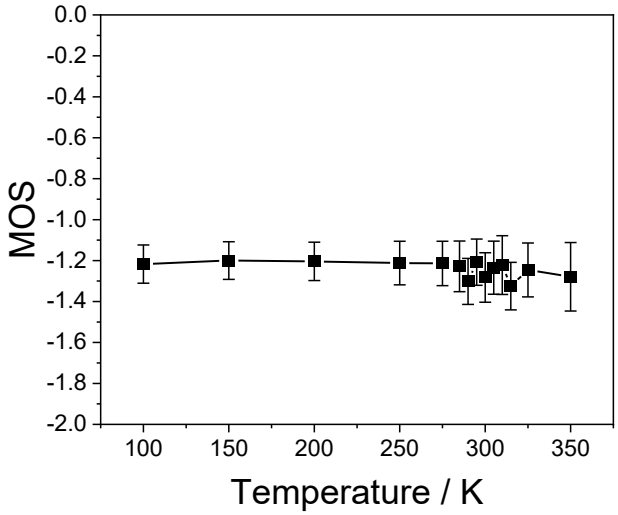

Figure S28. Temperature dependence of the metrical oxidation state for the thea$^{3\bullet-}$ ligand in **2**·3toluene·2MeCN.[42,43]

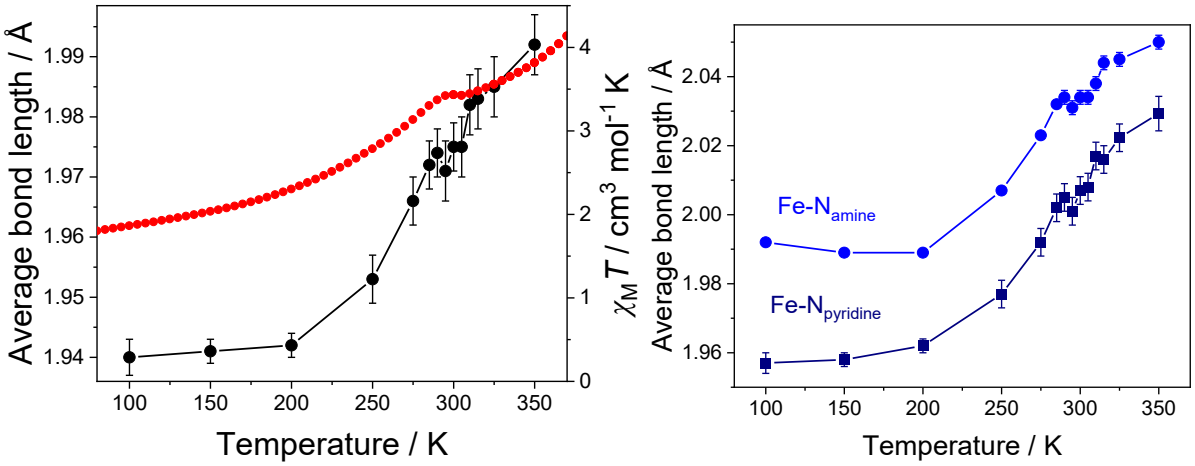

Figure S29. Left: Temperature dependence of the average Fe−N/O bond lengths for **2**·3toluene·2MeCN (left axis) overlaid with the plot of a $\chi_M T$ vs T (open black circles) for **2**·0.5toluene·3H_2O (right axis). Right: Temperature dependence of the Fe−N_{amine} (blue) and average Fe−$N_{pyridine}$ (dark blue) bond lengths for **2**·3toluene·2MeCN.

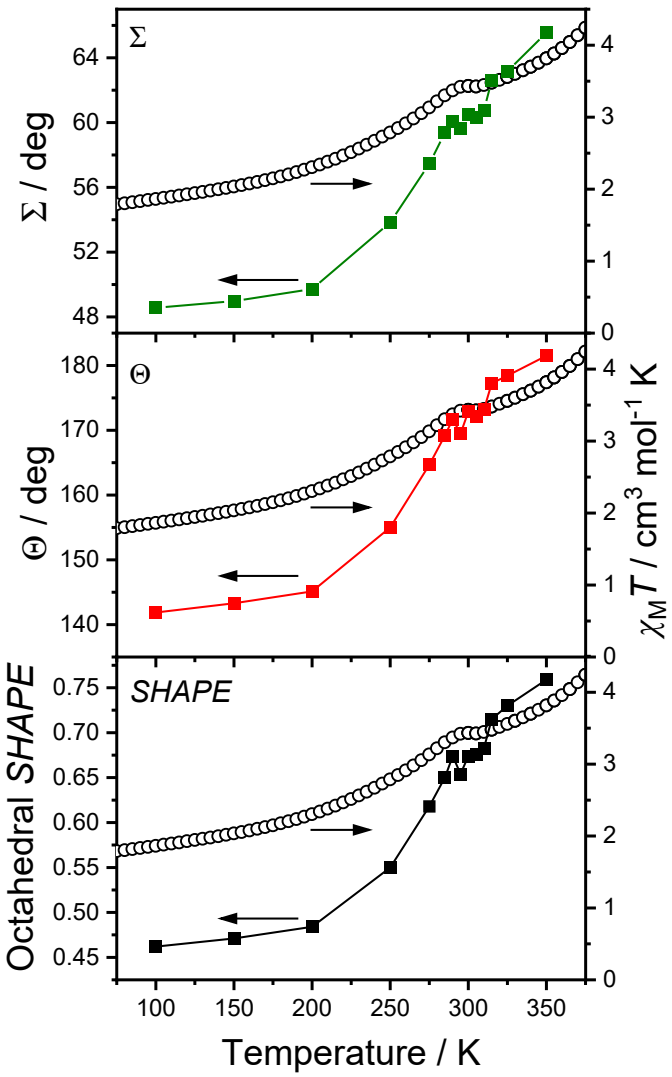

Figure S30. Temperature dependence of the octahedral *SHAPE* parameter, Σ and Θ distortion parameters for **2**·3toluene·2MeCN (left axis), overlaid with the plot of a $\chi_M T$ vs T (open black circles) for **2**·0.5toluene·3H_2O (right axis).

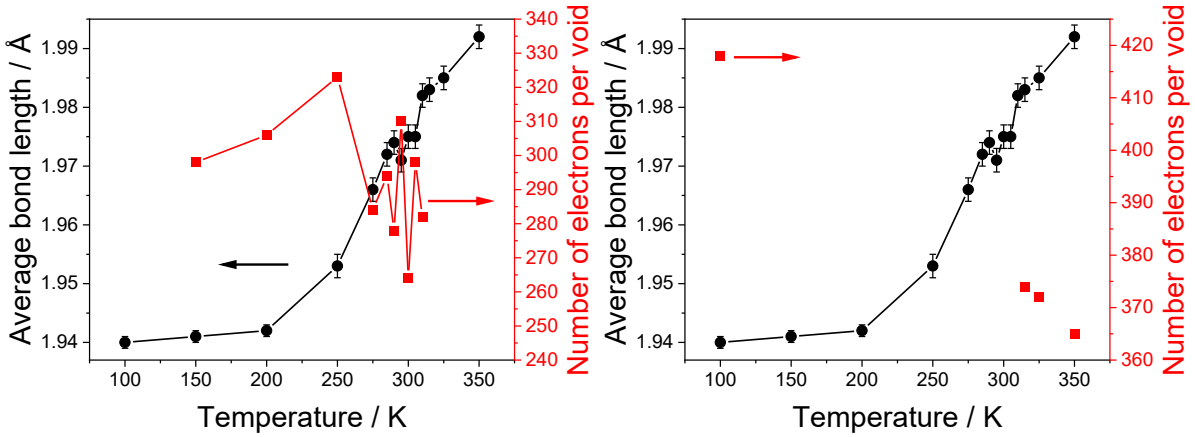

Figure S31. Left: Temperature dependence of the average Fe−N/O bond lengths for **2**·3toluene·2MeCN (left axis) overlaid with the number of electrons per void as determined using the OLEX2 solvent mask routine.[10]

Evolution of Intermolecular Interactions with Increasing Temperature

In the structure of **2**·3toluene·2MeCN, both PF_6^- anions are disordered over three orientations across all temperatures, and one MeCN and one toluene molecule were too severely disordered to model reliably. A second toluene molecule was ordered only between 150–310 K, becoming disordered at the lowest and highest temperatures examined.

To assess for any possible contributions of anion/solvent dynamics to the observed magnetic plateau, we analyzed the shortest P−F···H−C contacts. We chose the PF_6^- component that has the shortest interaction with the cation. For the complete PF_6^- anion in the asymmetric unit, three short contacts (Figure S32, S33 labels A–C, ~2.6 Å at 100 K) were identified: A expands steadily with increasing temperature while B and C remain essentially flat with only minor fluctuations, consistent with smooth thermal expansion. The second PF_6^-, which sits on a center of symmetry, engages in multiple contacts (Figure S32, S33 labels D–G, ~2.5 – 2.9 Å at 100 K) that likewise increase in length gradually with increasing temperature. Between 290 – 305 K, some of these interactions (notably E and G) show slight contractions that coincide with the magnetic plateau. However, these changes are modest (<0.1 Å) and reversible, with no evidence of abrupt jumps or discontinuities. Importantly, the displacement and occupancies of the PF_6^- disorder components vary smoothly across the plateau, indicating dynamic disorder and not any form of ordering. Therefore, while the PF_6^- anions provide a weak network of contacts, including bridging interactions between neighboring dimers (Figure S32, D–H), these evolve continuously with temperature and do not seem to account for the two-step SCO. Instead, the minor contraction of the cation-anion contacts at the plateau likely reflects the plateau in the Fe−N/O bond lengths in the cation, which minimizes the lattice expansion during the SCO interconversion.

In addition to direct cation-PF_6^- contacts, we also identified a network of interactions involving PF_6^- anions (Figure S32, S33 contacts 1–9), the modelled toluene molecule, and adjacent cations. The P−F···H−C(toluene) contacts (~2.5 – 3.0 Å) connect the dimers in the unit cell, establishing weak but extended intermolecular bridges. These interactions lengthen gradually with temperature (Figure S32, S33), with no significant discontinuities at the plateau region, , again consistent with smooth thermal expansion rather than a discrete reorganization. However, it is possible these interactions (along with interactions D–H) play a role in mediating cooperative elastic coupling between neighbouring dimers: the PF_6^- anions act as flexible linkers, and the inclusion of toluene enhances this bridging network. This framework possibly plays a role in the two-step SCO of **2**, with the cooperative interactions supporting stabilization of the [LS-HS] state, but with the absence of any sharp structural transition, we suggest the two-step phenomenon is intrinsic to the molecular framework and therefore the MV state of the bridging ligand.

In the structure of **3**·2MeCN·3*i*Pr$_2$O, one PF_6^- was localized, two PF_6^- anions were disordered over two orientations, and the last PF_6^- anion was disordered over three orientations. The solvent molecules were too severely disordered to be modelled reliably. We therefore analyzed the PF_6^- components that has the shortest interaction with the cation. All four PF_6^- anions form multiple P−F···H−C interactions (Figure S38, S39 labels 1–16, ~2.5–2.9 Å at 100 K). Across 100–350 K, many of these contacts increase smoothly with temperature, consistent with thermal expansion, while others show modest fluctuations attributed to local anion disorder. This is consistent with the absence of SCO for **3**·2MeCN·3*i*Pr$_2$O in the 100 – 350 K region.

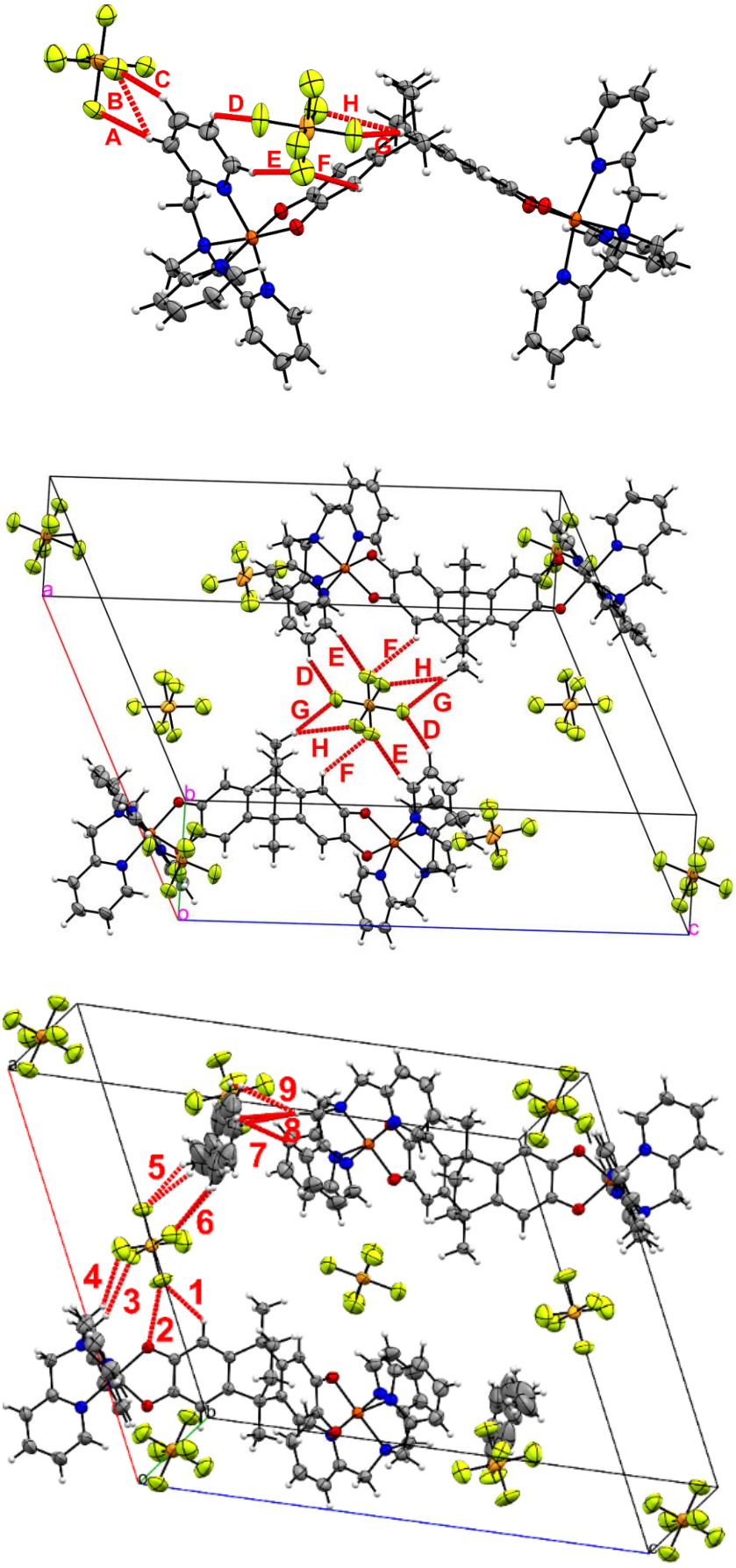

Figure S32. Supramolecular interactions in the structure of **2**·3toluene·2MeCN between the cations and the PF_6^- anions and toluene molecules (labelled A–G for those just between the cations and PF_6^-, and labelled 1–9 for those involving PF_6^-, toluene and the cations).

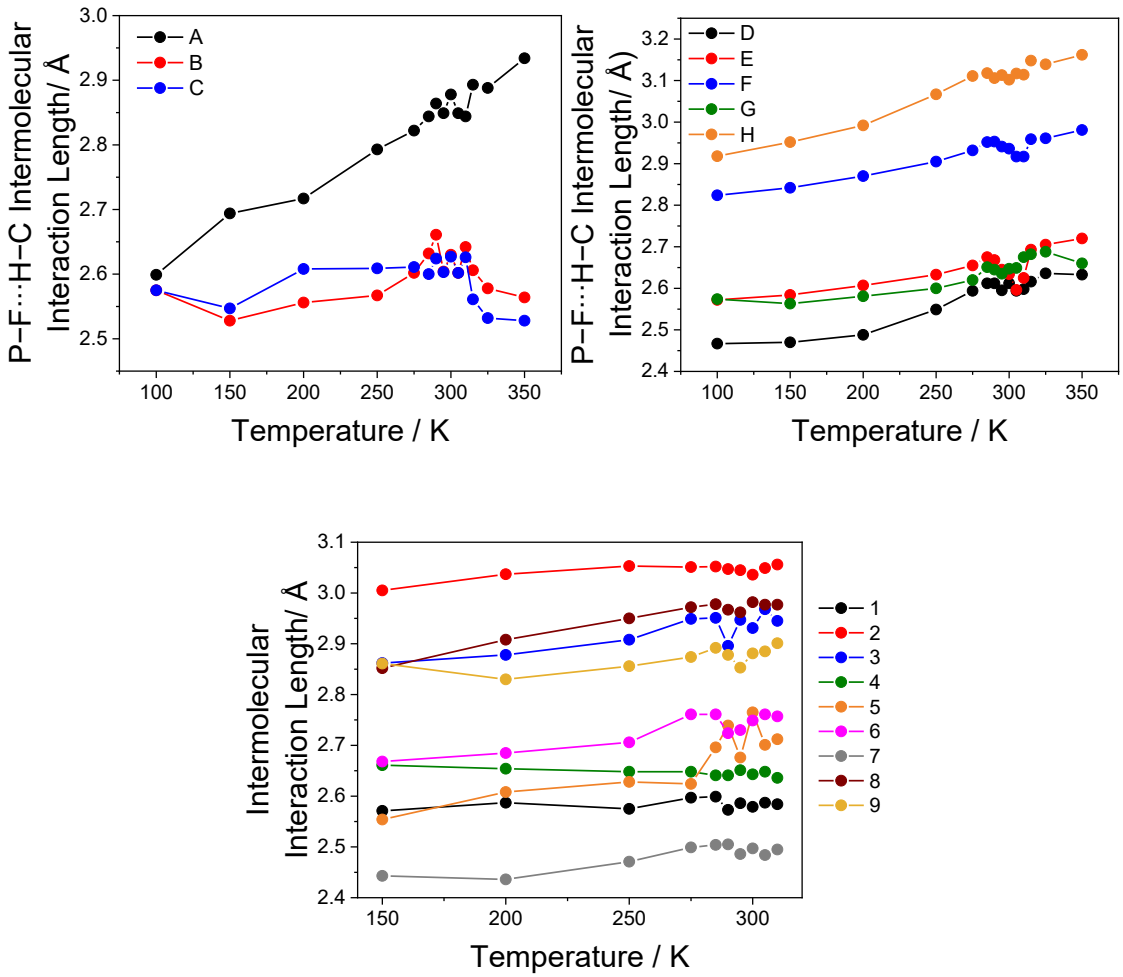

Figure S33. Evolution of the supramolecular interactions in structure of **2**·3toluene·2MeCN between the cations and the PF_6^- anions and toluene molecules (labelled A–G for those just between the cations and PF_6^-, and labelled 1–9 for those involving PF_6^-, toluene and the cations, Figure S30) with increasing temperature. For interactions 1–9, only the temperature 150–310 K are analyzed as at all other temperatures, the toluene molecule is too disordered to be effectively modelled.

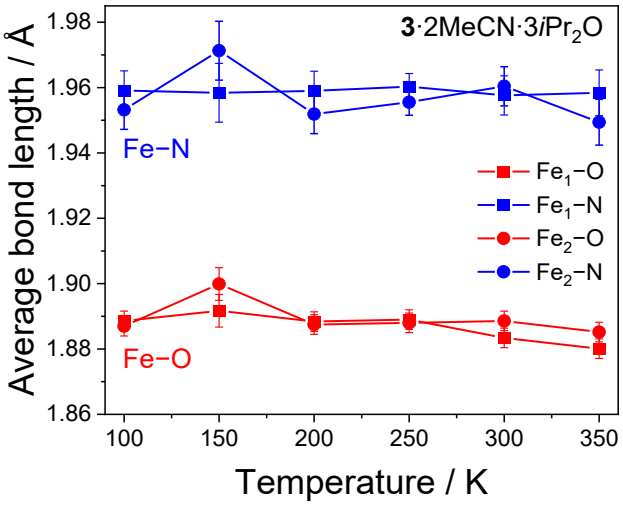

Figure S34. Temperature dependence of the Fe–N (blue) and Fe–O (red) bond lengths of the two Fe^{III} centers for **3**·2MeCN·3*i*Pr_2O.

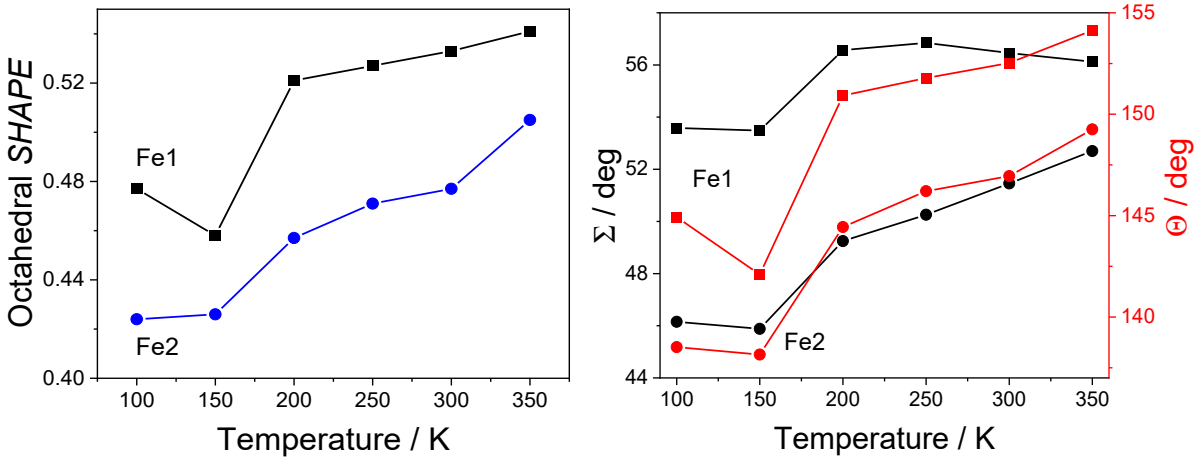

Figure S35. Temperature dependence of the octahedral *SHAPE* parameter, Σ and Θ distortion parameters for two Fe^{III} centers for **3**·2MeCN·3*i*Pr_2O.

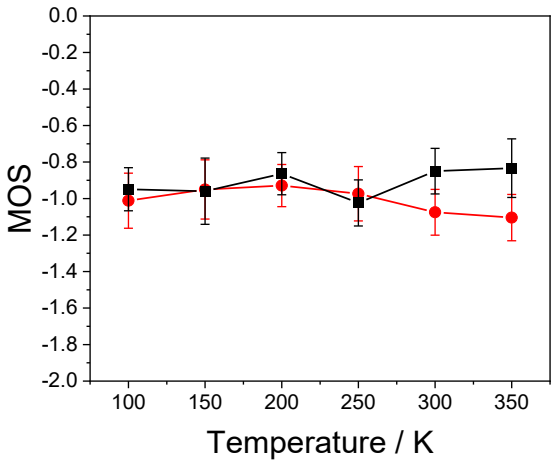

Figure S36. Temperature dependence of the metrical oxidation state for two dioxolene moieties in the thea^{2-} ligand in **3**·2MeCN·3*i*Pr$_2$O.[42,43]

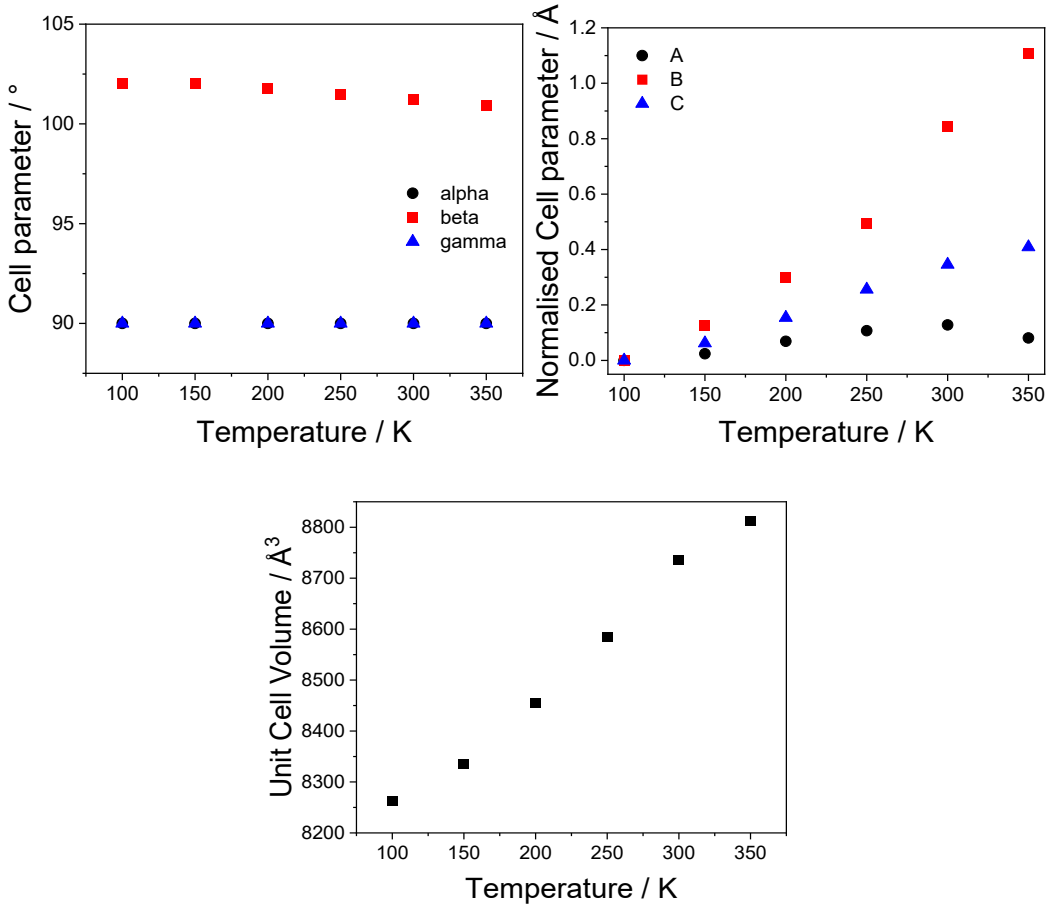

Figure S37. Temperature dependence of $a/a_{300\ K}$, $b/b_{300\ K}$ and $c/c_{300\ K}$ cell parameters, α, β and γ cell parameters, and unit cell $V/V_{300\ K}$ in in **3**·2MeCN·3*i*Pr$_2$O.

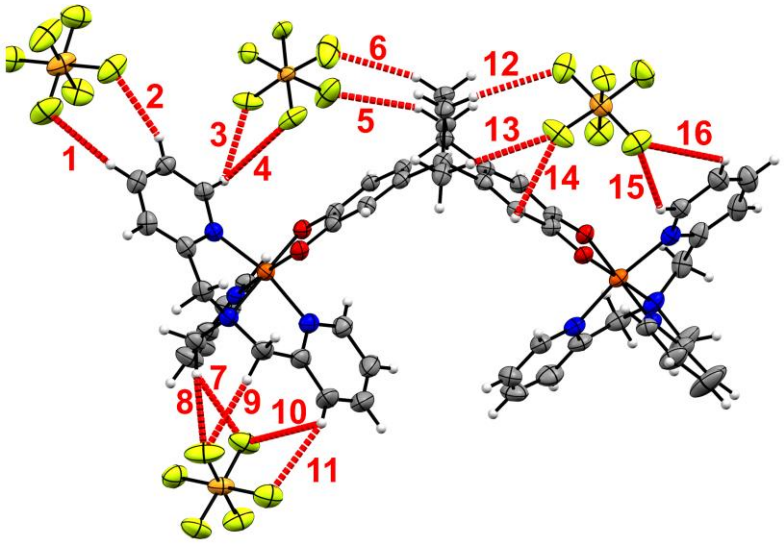

Figure S38. Supramolecular interactions in the structure of **3**·2MeCN·3*i*Pr$_2$O between the cations and the PF_6^- anions (labelled 1–16)

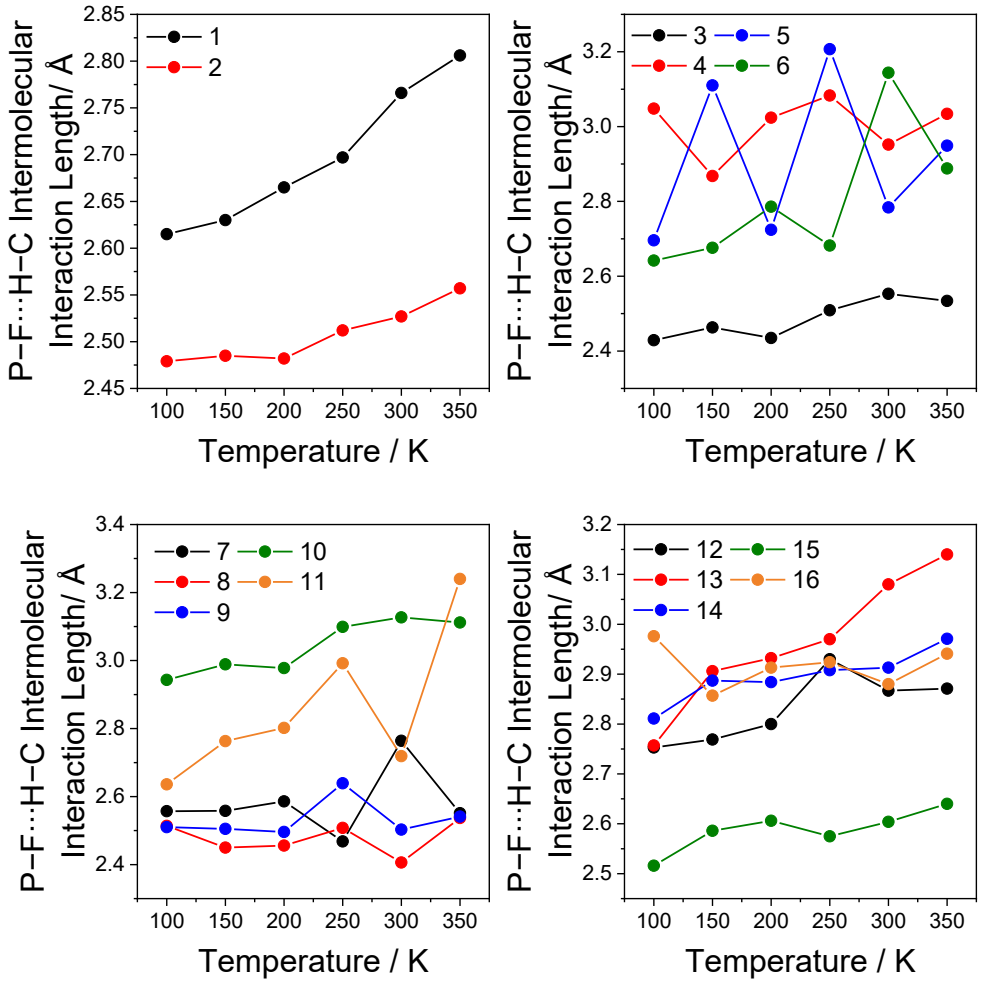

Figure S39. Evolution of the supramolecular interactions in structure of **3**·2MeCN·3*i*Pr$_2$O between the cations and the PF_6^- anions (Figure S36, labelled 1–16) with increasing temperature.

Solution-State Magnetic Data

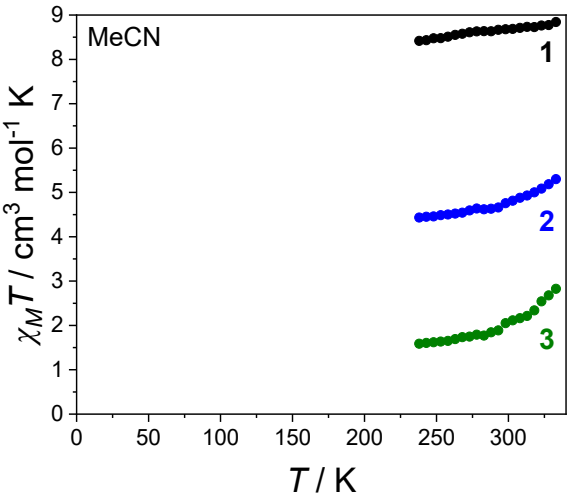

Figure S40. Plots of $\chi_M T$ vs T for solution state magnetic data for **1** (black), **2** (blue), and **3** (green) in d_3-MeCN.

EPR Spectroscopy

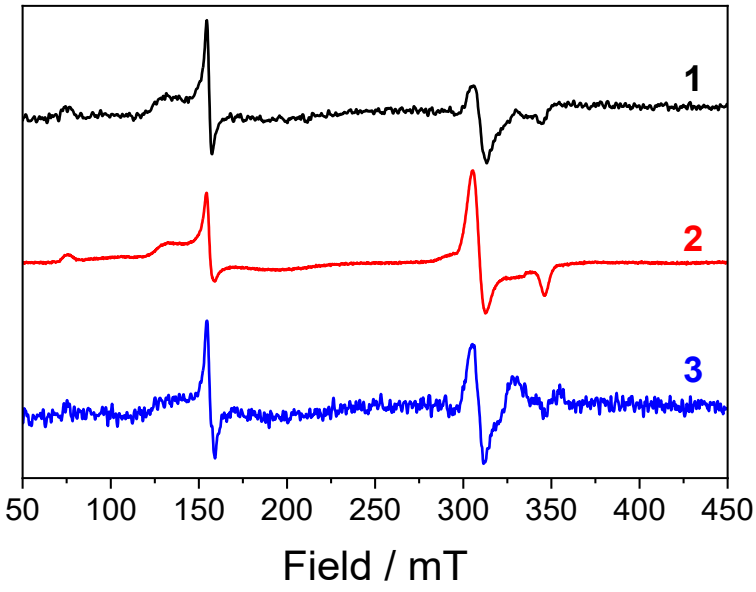

Figure S41. Frozen solution X-band EPR spectra of **1** (ν = 9.372944 GHz), **2** (ν = 9.374712 GHz) and **3** (ν = 9.378217 GHz) in a 1:1 DCM:toluene mixture measured at 10 K.

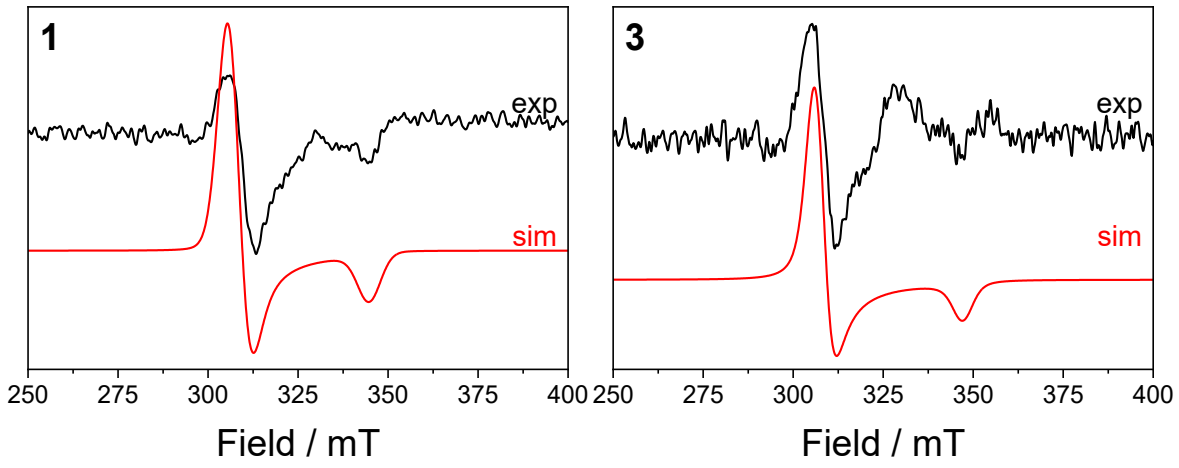

Figure S42. Left: frozen solution X-band (ν = 9.372944 GHz) EPR spectrum of **1** as presented in Figure S41 focusing on the LS-Fe^{III} region in 1:1 DCM:toluene mixture measured at 10 K (black) and simulation (red) using the parameters indicated in Table S12. Right: frozen solution X-band (ν = 9.378217 GHz) EPR spectrum of **3** as presented in Figure S41 focusing on the LS-Fe^{III} region in 1:1 DCM:toluene mixture measured at 10 K (black) and simulation (red) using the parameters indicated in Table S12.

Table S12. EPR simulation parameters for the solution-state (1:1 DCM:toluene) X-band spectra of **1**, **2** and **3**. The two components of the linewidth refer to the Lorentzian and Gaussian components of pseudo-Voigtian lineshape, as implemented in EasySpin

1	
$g_{\perp}$	2.180
$g_{\parallel}$	1.942
Line width / mT	[6, 0.5]
J / cm^{-1}	0
2	
$g_{\perp}$ (Fe1)	2.264
$g_{\parallel}$ (Fe1)	1.870
$g_{\perp}$ (Fe2)	2.268
$g_{\parallel}$ (Fe2)	1.920
Line width / mT	[4.8, 3.3]
$J_{\text{Fe1-SQ}}$ / cm^{-1}	−2.0
$J_{\text{Fe2-SQ}}$ / cm^{-1}	−0.25
3	
$g_{\perp}$	2.18
$g_{\parallel}$	1.93
g (SQ$^{\bullet-}$)	2.0
Line width / mT	[4, 2]
$J_{\text{Fe-SQ}}$ / cm^{-1}	−17
$J_{\text{SQ-SQ}}$ / cm^{-1}	−430

Simulation of the EPR spectrum of 2

We note at the outset that EPR simulations are inherently model-dependent and interpretative, with small variations in parameters potentially yielding simulations of different quality. To assess the accuracy of simulation of the 10 K frozen solution spectrum of **2**, we systematically tested a range of models ([LS-LS] state). First, simulation assuming identical $g_\perp$ and $g_\parallel$ for both Fe^{III} centers and equal exchange with the bridging $SQ^{\bullet-}$ ($J = -0.5$ cm^{-1} ($-2J\hat{S}_1\cdot\hat{S}_2$ formalism), as determined from the fit of the magnetic data of **2**, Figure S43) yielded $g_\perp = 2.270$ and $g_\parallel = 1.893$, but failed to reproduce the experimental spectrum, particularly the peaks at 290 and ~330 mT. Attempts with different identical $g_\perp$ and $g_\parallel$ values for both Fe^{III} centers and different J values that is equal for both Fe^{III} sites and $SQ^{\bullet-}$ likewise gave poor simulations (Figure S44).

Allowing the two Fe^{III} centers to have distinct g-values and a difference in the exchange between the bridging $SQ^{\bullet-}$ and the two Fe^{III} centers produced the best simulation, with $g_\perp = 2.264$ and $g_\parallel = 1.870$ for Fe1, $g_\perp = 2.268$ and $g_\parallel = 1.920$ for Fe2, and $J_1 = -2.0$ cm^{-1} and $J_2 = -0.25$ cm^{-1} ($-2J\hat{S}_1\cdot\hat{S}_2$ formalism) (Figure 4). To test the robustness of this solution, we carried out additional simulations constraining either the g-values (identical for both Fe^{III} centers) while allowing anisotropic J, or enforcing isotropic J while allowing distinct g-values. None adequately reproduced the data (Figures S45–S47, Table S13). Finally, swapping the J_1 and J_2 values while keeping the best-fit g-values also produced a poorer simulation (Figure S48).

Together, these tests demonstrate that accurate reproduction of the spectrum requires both slight differentiation in g-values and distinct exchange interactions. This supports electronic asymmetry between the Fe centers, consistent with localization of the $SQ^{\bullet-}$, and underpins the interpretative but well-justified assignment of an [LS-HS] state for **2** discussed in the main text.

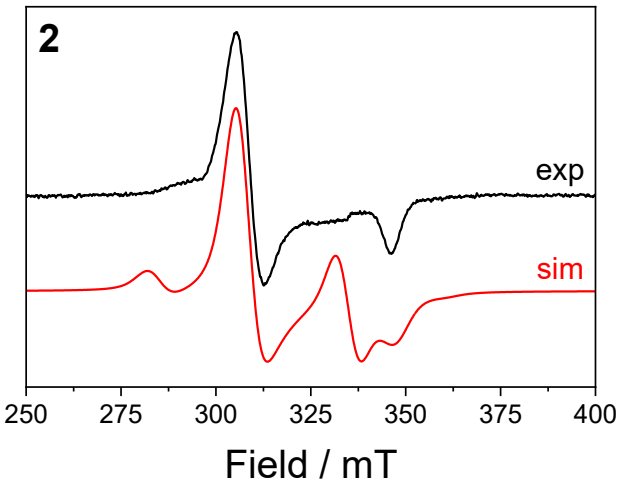

Figure S43. Frozen solution X-band (ν = 9.374712 GHz) EPR spectrum of **2** in 1:1 DCM:toluene mixture measured at 10 K (black) and best simulation (red) obtained by keeping exchange interactions between the two Fe^{III} sites and $SQ^{\bullet-}$ as equal and fixed to $J = -0.5$ cm^{-1} as determined from magnetic measurements. Parameters: $g_{\perp} = 2.270$, $g_{\parallel} = 1.893$, $g_{SQ} = 2.0$, $J_{Fe\text{-}SQ} = -0.5$ cm^{-1}, line width (mT) = [4.8 3.3]. This fit fails to reproduce the observed spectral features, illustrating that assuming equal exchange for both Fe centers, and identical *g* value parameters for both Fe centers is insufficient and highlighting the need for differentiated *g*-values and exchange constants in the final, best-fit simulation.

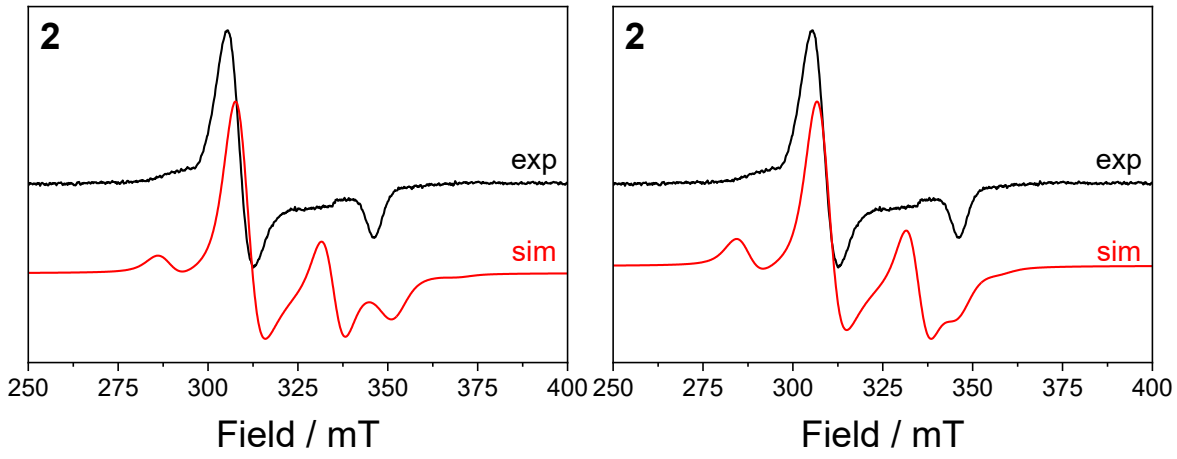

Figure S44. Illustrative simulations with same *g* values for both Fe^{III} centers, and isotropic *J*. Left: Frozen solution X-band (ν = 9.374712 GHz) EPR spectrum of 2 in 1:1 DCM:toluene mixture measured at 10 K (black) and best simulation (red) with $g_{\perp} = 2.245$ and $g_{\parallel} = 1.859$ (both Fe^{III} sites) , $g_{SQ} = 2.0$, $J_{Fe\text{-}SQ} = -0.25$ cm^{-1}, line width (mT) = [4.8 3.3]. Right: Frozen solution X-band (ν = 9.374712 GHz) EPR spectrum of 2 in 1:1 DCM:toluene mixture measured at 10 K (black) and best simulation (red) with $g_{\perp} = 2.255$ and $g_{\parallel} = 1.905$ (both Fe^{III} sites) , g_{SQ} = 2.0, $J_{Fe\text{-}SQ} = -1.5$ cm^{-1}, line width (mT) = [4.8 3.3]. These fits fail to reproduce the observed spectral features, illustrating that assuming equal exchange for both Fe centers, and identical *g* value parameters for both Fe centers is insufficient and highlighting the need for differentiated *g*-values and exchange constants in the final, best-fit simulation.

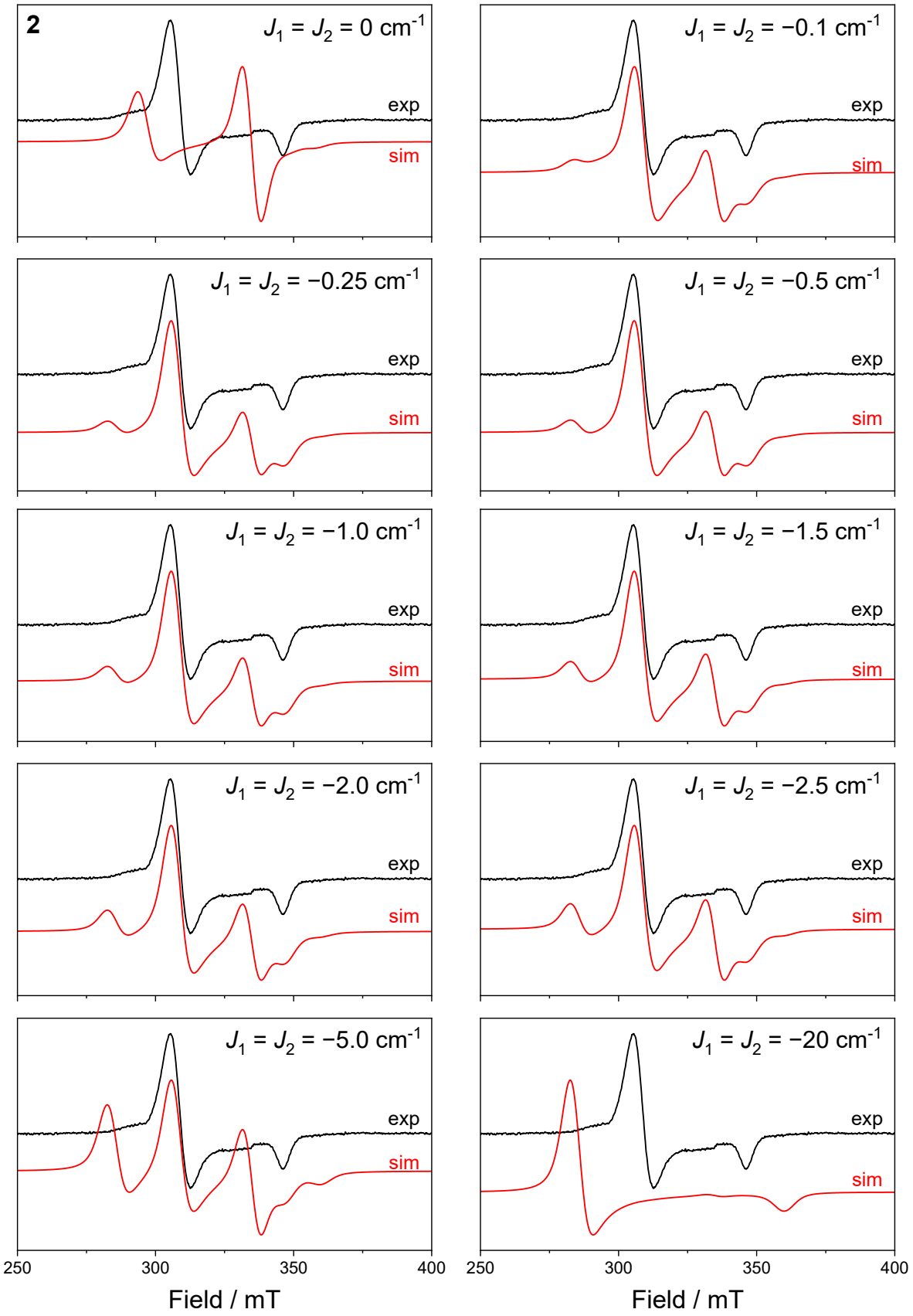

Figure S45. Solution-state X-band (ν = 9.374712 GHz) EPR spectrum of **1** in 1:1 DCM:toluene mixture measured at 10 K (black) and simulations (red) varying the value of *J* using the parameters indicated in Table S13. These simulations illustrate that using identical *J* for both Fe^{III} centers fails to reproduce the experimental spectrum, highlighting that differentiation in both *g*-values and exchange interactions is required to accurately model the data.

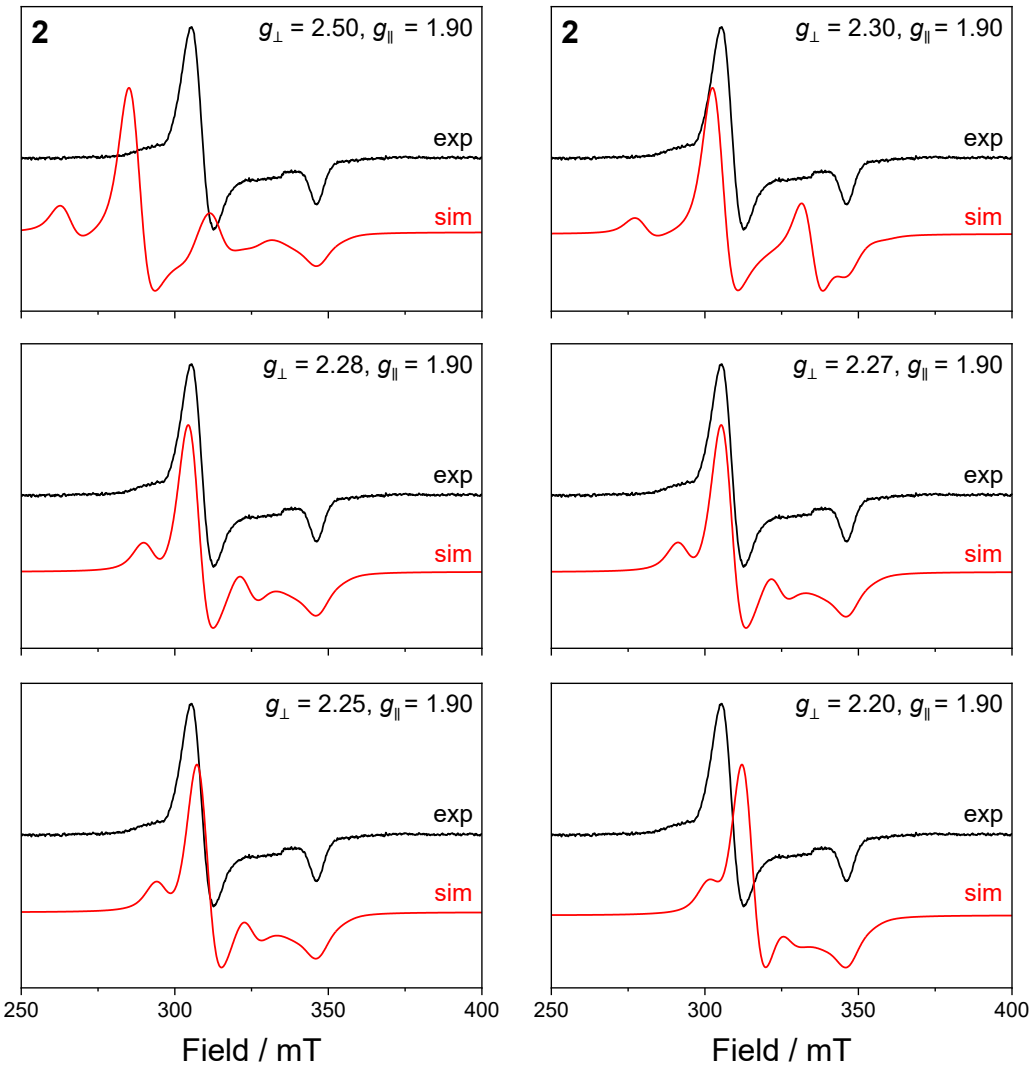

Figure S46. Solution-state X-band (ν = 9.374712 GHz) EPR spectrum of **1** in 1:1 DCM:toluene mixture measured at 10 K (black) and simulations (red) varying the value of $g_\perp$ using the parameters indicated in Table S13. These simulations illustrate that using identical $g_\parallel$ for both Fe^{III} centers fails to well reproduce the experimental spectrum, highlighting that differentiation in both *g*-values and exchange interactions is required to accurately model the data.

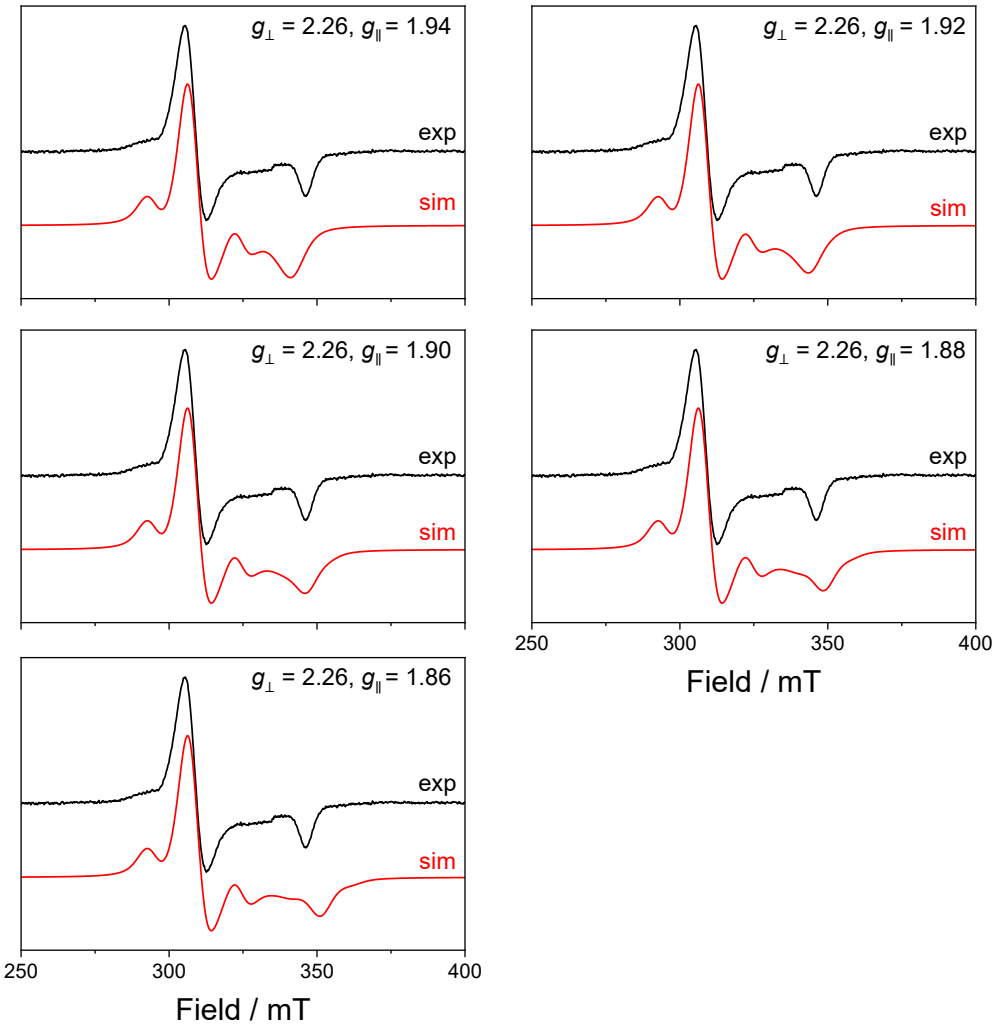

Figure S47. Solution-state X-band (ν = 9.374712 GHz) EPR spectrum of **1** in 1:1 DCM:toluene mixture measured at 10 K (black) and simulations (red) varying the value of $g_\parallel$ using the parameters indicated in Table S13. These simulations illustrate that using identical $g_\perp$ for both Fe^{III} centers fails to well reproduce the experimental spectrum, highlighting that differentiation in both *g*-values and exchange interactions is required to accurately model the data.

Table S13. Investigated parameter space in Figures S45-S47 for the frozen solution (1:1 DCM:toluene) X-band EPR spectrum of **2**. The two components of the linewidth refer to the Lorentzian and Gaussian components of pseudo-Voigtian lineshape, as implemented in EasySpin.

2 – variation of $g_{\perp}$										
$g_{\perp}$ (Fe1, Fe2)	2.50	2.30	2.28	2.27	2.25	2.20				
$g_{\parallel}$ (Fe1, Fe2)	1.90	1.90	1.90	1.90	1.90	1.90				
g ($SQ^{\bullet-}$)	2.0	2.0	2.0	2.0	2.0	2.0				
Line width / mT	[4.8, 3.3]	[4.8, 3.3]	[4.8, 3.3]	[4.8, 3.3]	[4.8, 3.3]	[4.8, 3.3]				
$J_{Fe1\text{-}SQ}$ / cm^{-1}	−2.0	−2.0	−2.0	−2.0	−2.0	−2.0				
$J_{Fe2\text{-}SQ}$ / cm^{-1}	−0.25	−0.25	−0.25	−0.25	−0.25	−0.25				
2 – variation of $g_{\parallel}$										
$g_{\perp}$ (Fe1, Fe2)	2.26	2.26	2.26	2.26	2.26					
$g_{\parallel}$ (Fe1, Fe2)	1.94	1.92	1.90	1.88	1.86					
g ($SQ^{\bullet-}$)	2.0	2.0	2.0	2.0	2.0					
Line width / mT	[4.8, 3.3]	[4.8, 3.3]	[4.8, 3.3]	[4.8, 3.3]	[4.8, 3.3]					
$J_{Fe1\text{-}SQ}$ / cm^{-1}	−2.0	−2.0	−2.0	−2.0	−2.0					
$J_{Fe2\text{-}SQ}$ / cm^{-1}	−0.25	−0.25	−0.25	−0.25	−0.25					
2 – variation of J										
$g_{\perp}$ (Fe1)	2.264	2.264	2.264	2.264	2.264	2.264	2.264	2.264	2.264	2.264
$g_{\parallel}$ (Fe1)	1.870	1.870	1.870	1.870	1.870	1.870	1.870	1.870	1.870	1.870
$g_{\perp}$ (Fe2)	2.268	2.268	2.268	2.268	2.268	2.268	2.268	2.268	2.268	2.268
$g_{\parallel}$ (Fe2)	1.920	1.920	1.920	1.920	1.920	1.920	1.920	1.920	1.920	1.920
g ($SQ^{\bullet-}$)	2.0	2.0	2.0	2.0	2.0	2.0	2.0	2.0	2.0	2.0
Line width / mT	[4.8, 3.3]	[4.8, 3.3]	[4.8, 3.3]	[4.8, 3.3]	[4.8, 3.3]	[4.8, 3.3]	[4.8, 3.3]	[4.8, 3.3]	[4.8, 3.3]	[4.8, 3.3]
$J_{Fe1\text{-}SQ}$ / cm^{-1}	0	−0.1	−0.25	−0.5	−1.0	−1.5	−2.0	−2.5	−5.0	−20
$J_{Fe2\text{-}SQ}$ / cm^{-1}	0	−0.1	−0.25	−0.5	−1.0	−1.5	−2.0	−2.5	−5.0	−20

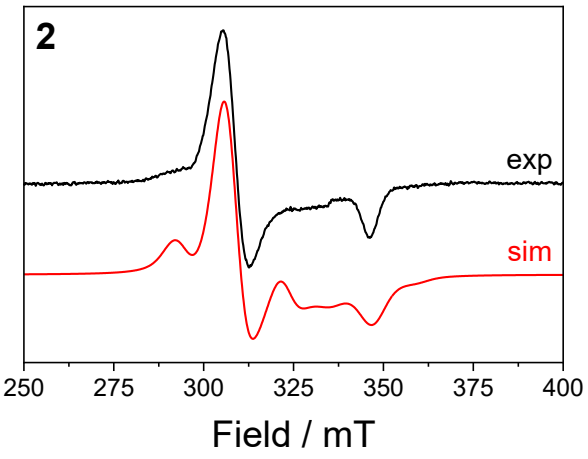

Figure S48. Frozen solution X-band (ν = 9.374712 GHz) EPR spectrum of **2** in 1:1 DCM:toluene mixture measured at 10 K (black) and best simulation (red) obtained using $g_{\perp}$ = 2.264 and $g_{\parallel}$ = 1.870 for Fe1, $g_{\perp}$ = 2.268 and $g_{\parallel}$ = 1.920 for Fe2 and exchange values J_1 = −0.25 cm^{-1} and J_2 = −2.0 cm^{-1}, line width (mT) = [4.8 3.3]. This simulation keeps the g-values of the two Fe centers the same as the best-fit model in the main text (Figure 4) but swaps the *J*-values, illustrating that the more anisotropic Fe center (Fe1) must have the stronger exchange with the $SQ^{\bullet-}$ to reproduce the experimental spectrum. This confirms that the observed differences in $g_{\perp}-g_{\parallel}$ correlate with exchange differences, supporting localization of the $SQ^{\bullet-}$and measurable electronic differentiation between the two Fe^{III} centers.

UV-Vis-NIR Spectroscopy

Table S14. Electronic absorption band assignment of **1**, **2** and **3**

Assignment	λ / nm (ε / mol L^{-1} cm^{-1})	Ref	Assignment	λ / nm (ε / mol L^{-1} cm^{-1})	Ref	Assignment	λ / n (ε / mol L^{-1} cm^{-1})	Ref
1 (MeCN)			**1** (BuCN)			**1** (DCE)		
LMCT cat^{2-} → HS-Fe^{III}	520 (2720)	[2]	LMCT cat^{2-} → HS-Fe^{III}	532 (2650)	[2]	LMCT cat^{2-} → HS-Fe^{III}	543 (3150)	[2]
LMCT cat^{2-} → HS-Fe^{III}	1020 (5660)	[2]	LMCT cat^{2-} → HS-Fe^{III}	1042 (6200)	[2]	LMCT cat^{2-} → HS-Fe^{III}	1054 (7606)	[2]
LMCT cat^{2-} → LS-Fe^{III}	1144 (3310), 1190 (1960)	[2]	LMCT cat^{2-} → LS-Fe^{III}	1170 (3260), 1200 (2430)	[2]	LMCT cat^{2-} → LS-Fe^{III}	1146 (5910), 1200 (3210)	[2]
2 (MeCN)			**2** (BuCN)			**2** (DCE)		
$SQ^{\bullet-}$ π → π*	360 (5600), 394 (5710)	[27,28]	$SQ^{\bullet-}$ π → π*	360 (8640), 386 (8660)	[27,28]	$SQ^{\bullet-}$ π → π*	366 (6930), 376 (4740), 390 (3360)	
LMCT	512 (2880)		LMCT	520 (4230)		LMCT	524 (2350)	
MLCT	604 (2000)		MLCT	615 (3000)		-	-	
LMCT	842 (2680)		LMCT	870 (4080)		LMCT	817 (5770)	
LMCT cat^{2-} → LS-Fe^{III}	1048 (1200), 1204 (260)	[27,44–46]	LMCT cat^{2-} → LS-Fe^{III}	1020 (2000), 1110 (1170), 1190 (590)	[27,44–46]	IVCT	1096 (7220)	
3 (MeCN)			**3** (BuCN)			**3** (DCE)		
$SQ^{\bullet-}$ π → π*	359 (2920sh), 396 (3430)	[27,28]	$SQ^{\bullet-}$ π → π*	358 (4890sh), 392 (5660)	[27,28]	$SQ^{\bullet-}$ π → π*	349 (3320)	[27,28]
d-d	519 (160)[a]		d-d	524 (340)[a]		LMCT	760 (5480)	[27,28]
$SQ^{\bullet-}$ n → π*	754 (60), 941 (30)[a]	[27,44–46]	$SQ^{\bullet-}$ n → π*	778 (210), 971 (70)[a]	[27,44–46]	$SQ^{\bullet-}$ n → π*	1083 (480)	[27,44–46]

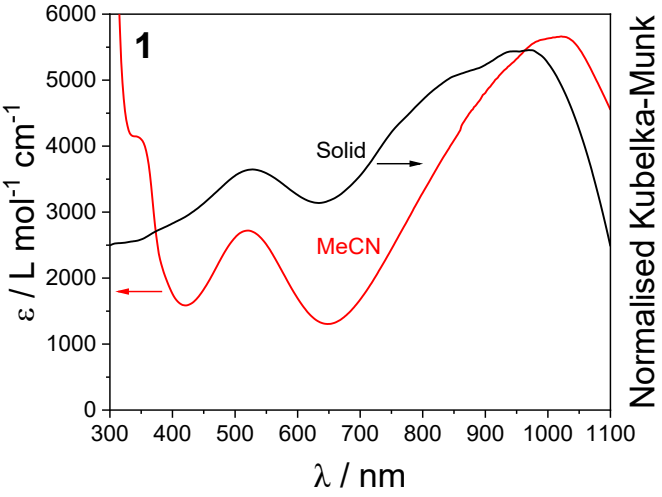

Figure S49. UV-Vis spectra of **1** in MeCN (red) vs **1**·2H_2O·0.5*i*Pr_2O measured as diffuse reflectance at room temperature (black), diluted ~5% in KBr.

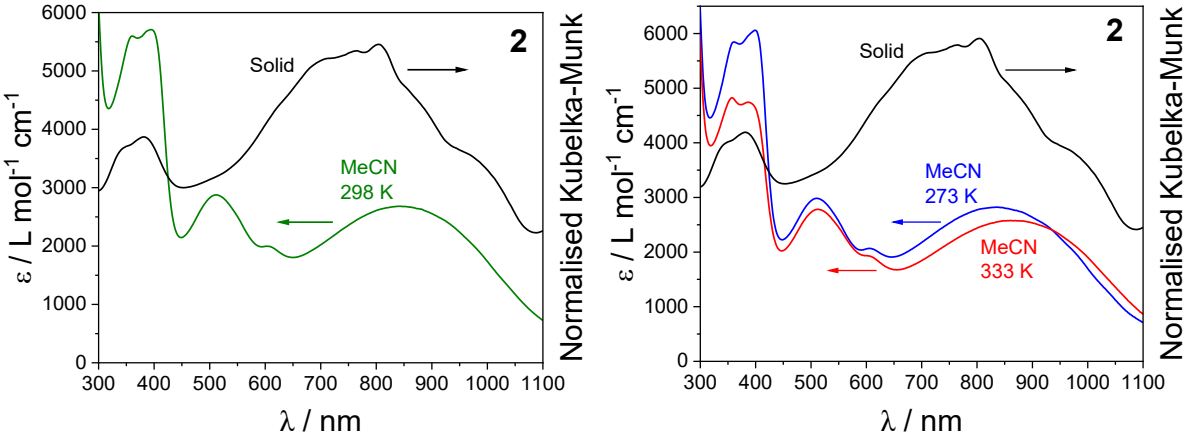

Figure S50. (Left) UV-Vis spectra of **2** in MeCN at 298 K (green) vs **2**·0.5toluene·3H_2O measured as diffuse reflectance at room temperature (black), diluted ~5% in KBr. (Right) UV-Vis spectra of **2** in MeCN at 273 K (blue) and 333 K (red) vs **2**·0.5toluene·3H_2O measured as diffuse reflectance at room temperature (black), diluted ~5% in KBr

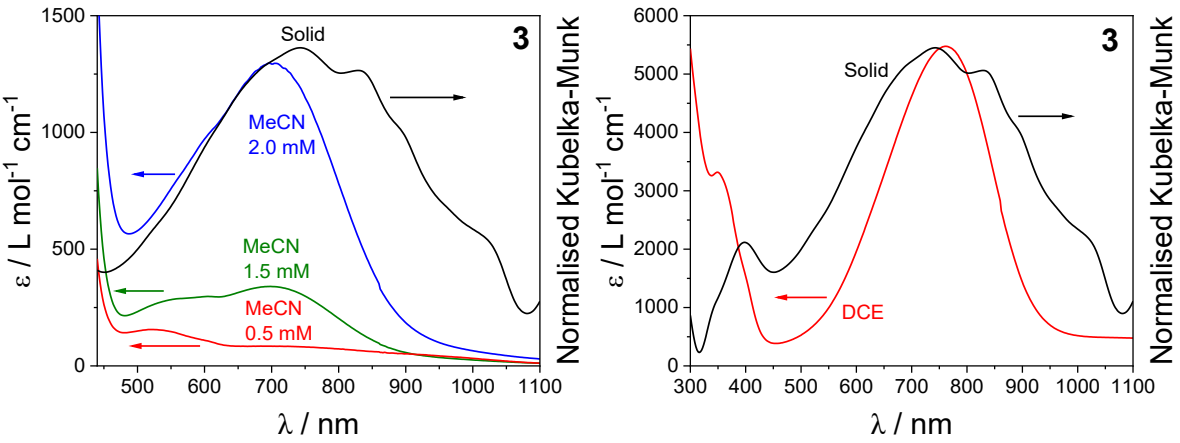

Figure S51. (Left) UV-Vis spectra of **3** in MeCN at 0.5 (red), 1.5 (green) and 2.0 mM (blue) vs **3**·0.5MeCN measured as diffuse reflectance at room temperature (black), diluted ~5% in KBr. (Right) UV-Vis spectra of **3** in DCE vs **3**·0.5MeCN measured as diffuse reflectance at room temperature (black), diluted ~5% in KBr.

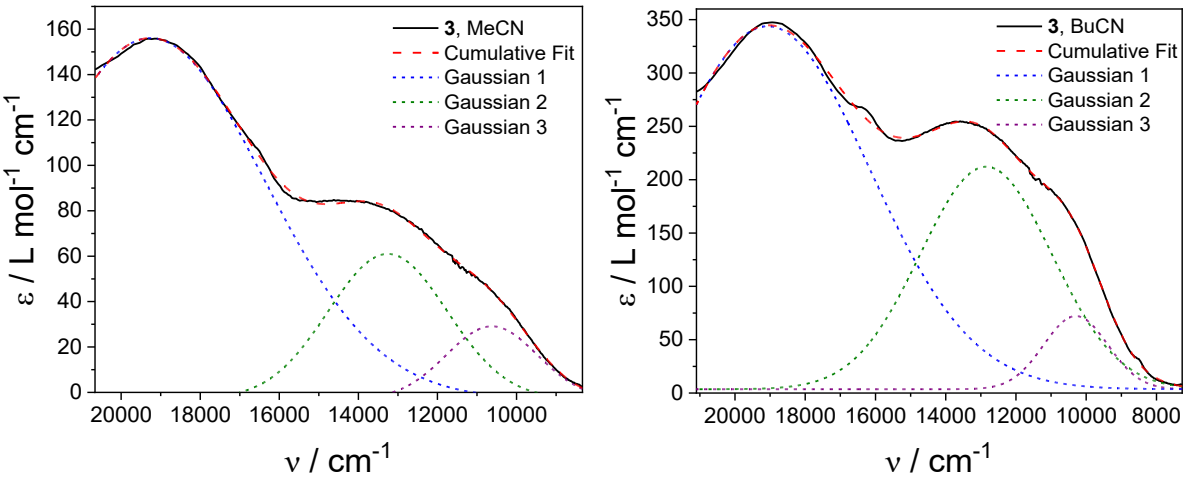

Figure S52. Low energy region of **3** in MeCN (left) and BuCN (right) fit with a three peak Gaussian fit (MeCN: R^2 = 1.000; BuCN: R^2 = 1.000).

Additional Electronic Spectroscopy Discussion

As the electronic structure of SCO compounds can be markedly solvent-dependent,[47–49] we collected ultraviolet-visible (UV-Vis) absorption spectra for **1**, **2** and **3** at room temperature in various solvents with a range of dielectric constants (κ): MeCN (κ = 37.5), butyronitrile (BuCN) (κ = 20.7), and dichloroethane (DCE) (κ = 10.4) (Figure S53, Table S14). As discussed in the main text, compound **1** in MeCN is dominated by $cat^{2-} \rightarrow$ HS-Fe^{III} ligand-to-metal charge transfer (LMCT) bands at 520–530 and 1020–1050 nm (Figure 5, S53).[2,31,50] This LMCT band is conserved in **2**, but shifted to higher energy as a result of oxidation of $thea^{4-}$ to $thea^{3\bullet-}$.[28] In addition in MeCN, **2** displays a $Fe^{III} \rightarrow SQ^{\bullet-}$ metal-to-ligand charge transfer (MLCT) band at 600 nm,[3,28,51,52] and two $SQ^{\bullet-}$ $\pi \rightarrow \pi^*$ transitions between 360–400 nm.[27,28,45] For compound **3**, no LMCT bands are observed in MeCN, with the spectrum dominated by the $SQ^{\bullet-}$ $\pi \rightarrow \pi^*$ transitions at ~400 nm (Figure 5, S53).[27,28,45]

The spectra of **1** is similar across all three solvents (Figure S53, Table S14). The LMCT bands are slightly influenced by the solvent, shifting to lower energy following MeCN > BuCN > DCE. This red-shifting of the LMCT follows the trend of decreasing dielectric constant, likely occurring from stabilization of the Fe^{II}-SQ state by the less polar solvents,[53,54] which has a lower dipole moment compared to Fe^{III}-cat. Across all three solvents, **2** features the LMCT band (Figure S53). In both MeCN and BuCN, two $SQ^{\bullet-}$ $\pi \rightarrow \pi^*$ peaks are observed, whereas in DCE, only a shoulder is observed. Notably, the most significant differences is the broad and intense peak at 1100 nm in DCE that is not observed in MeCN and BuCN, assigned as a intervalence charge transfer (IVCT) process. This is discussed in the main text.

In all three solvents, **3** exhibits $SQ^{\bullet-}$ n $\rightarrow \pi^*$ transitions between 360–400 nm (Figure S53, Table S14). Interestingly, the spectrum of **3** in DCE features a dominant intense peak at 760 nm that is not observed in MeCN or BuCN. This transition is discounted as a $SQ^{\bullet-}$ n $\rightarrow \pi^*$

transition as it is too sharp/intense and lacks vibronic structure,[27,44–46] and is assigned as a $SQ^{\bullet-}$ → Fe^{III} LMCT. Only the spectrum in DCE matches with the solid-state spectrum (Figure S51). The difference of the spectrum of **3** in MeCN and BuCN compared with that in DCE and the solid-state could be due to decomposition. However, decomposition is discounted by the ability to recover **3** after dissolution in MeCN, followed by removal of the solvent. We performed additional analysis to understand the solvatochromism of **3** (see below, "Solution Properties of Compound 3").

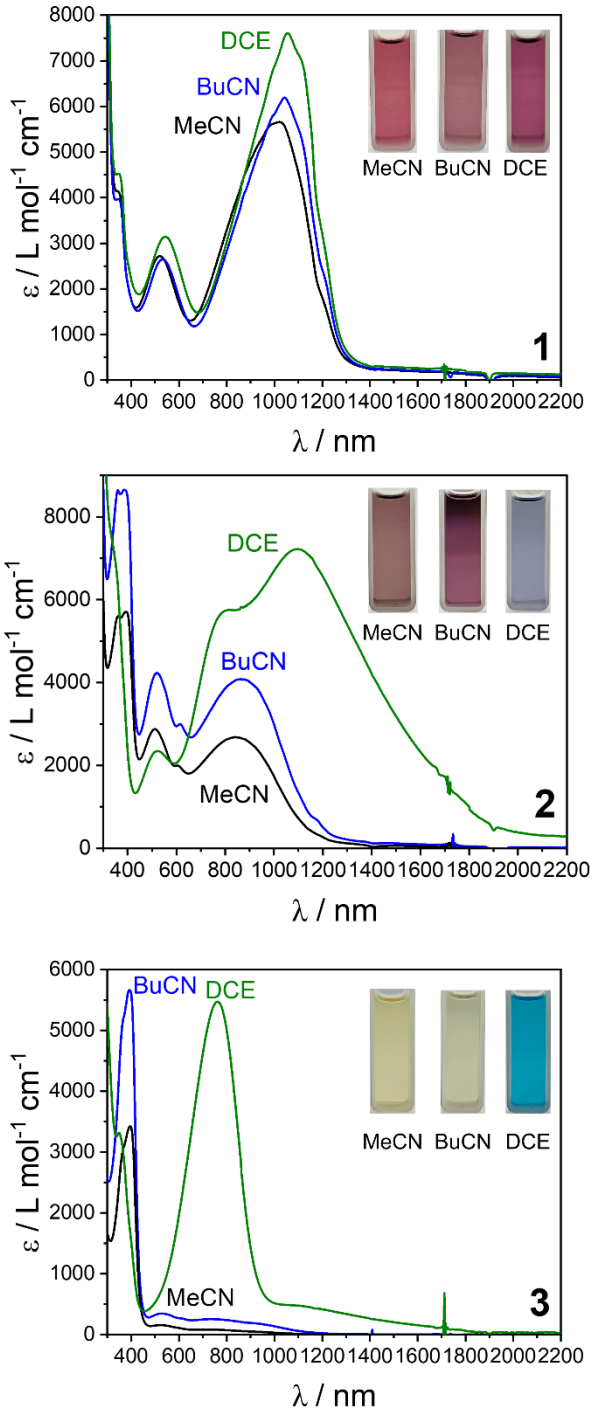

Figure S53. UV-Vis-NIR absorption spectra for MeCN, BuCN and DCE solutions of **1**, **2** and **3** at 298 K. Inset photographs of **1**, **2** and **3** in MeCN, BuCN and DCE at 298 K.

Solution Properties of Compound 3

To study the origin of the solvatochromism of **3**, we conducted additional UV-Vis-NIR, variable temperature UV-Vis, and variable temperature ^{1}H NMR spectroscopy studies (Figure S54-S66, Table S15). In this process, we first noticed that the color of **3** in MeCN is dependent on the concentration (Figure S54): yellow at low concentrations, green at medium concentrations, and blue at high concentrations. The solid sample of **3** is blue. Upon increasing the concentration from 0.5 mM (concentration discussed in main text and above) to 1.5 and 2.0 mM results in an increase in the intensity of a peak at 700 nm (Figure S54), with the spectrum approaching that observed in DCE and the solid-state (Figure S51, S53). This peak at 700 nm is likely a $SQ^{\bullet-} \rightarrow Fe^{III}$ LMCT process, which increases in intensity with increasing concentration. The number and positions of the processes in the CV of **3** is the same at 0.5 and 1.0 mM (Figure S56), suggesting the presence of similar species in solution at these different concentrations. The change in the spectrum of **3** in MeCN with increasing concentration could be arising from the formation of supramolecular dimers in solutions, as observed in the solid-state structure for $[\{Pt(1,2\text{-bis(diphenyl-phosphino)ethane}\}_2(thea^{cat\text{-}SQ})]^+$.[55] However, no concentration-dependent effects are observed for the spectrum of the cobalt analogue $[\{Co^{III}(tpa)\}_2(thea)](PF_6)_4$ (**3-Co**) (Figure S57),[3] discounting supramolecular dimer formation as the source of the effect concentration has on the spectrum of **3** in MeCN.

Complex **3** could be undergoing a concentration-dependent equilibrium in MeCN. The mononuclear complex $[Fe^{III}(L\text{-}N_4Me_2)(dbSQ)]^{2+}$ (L-N_4Me_2 = N,N'-dimethyl-2,11-diaza[3.3]-(2,6)pyridinophane, $dbSQ^{\bullet-}$ = 3,5-di-*tert*-butyl-semiquinonate) in MeCN was found to undergo the equilibrium $[Fe^{III}(L\text{-}N_4Me_2)(dbsq)]^{2+} + 2MeCN \rightleftharpoons [Fe^{II}(L\text{-}N_4Me_2)(MeCN)_2]^{2+}$ + 3,5-di-*tert*-butyl-benzoquinone.[56] The right-hand side of this process is favored at higher temperatures and at lower concentrations. The increase in intensity of the $SQ^{\bullet-} \rightarrow Fe^{III}$ LMCT

feature in **3** upon increasing concentration and decreasing temperature (see Variable Temperature Solution Measurement section, Figure S60, S66) would support a similar equilibrium of **3** in MeCN: $[\{Fe^{III}(tpa)\}_2(thea^{SQ\text{-}SQ})]^{4+}$ + 4MeCN ⇌ $2[Fe^{II}(tpa)(MeCN)_2]^{2+}$ + $thea^{Q\text{-}Q}$ (Q = quinone). However, the presence of a $SQ^{\bullet-}$ $\pi \rightarrow \pi^*$ transition in MeCN at 0.5 mM suggests a more likely mechanism only involves half the complex: $[\{Fe^{III}(tpa)\}_2(thea^{SQ\text{-}SQ})]^{4+}$ +2MeCN ⇌ $[Fe^{III}(tpa)(thea^{SQ\text{-}Q})]^{2+}$ + $[Fe^{II}(tpa)(MeCN)_2]^{2+}$. This process would not occur in DCE, hence the spectrum of **3** in DCE matching the solid-state spectrum due to the presence of only $[\{Fe^{III}(tpa)\}_2(thea^{SQ\text{-}SQ})]^{4+}$.

To support this postulated this equilibrium of **3** in MeCN, we performed variable temperature ^{1}H NMR of **3** in d_3-MeCN (Figure S58). The ^{1}H NMR spectrum of **3** in d_3-MeCN at 0.5 mM at 253 K consists of four peaks in the aromatic region and three peaks in the aliphatic region (Figure S58). Comparing with the spectra of free tpa and $theaH_4$,[1,27] the peak at 1.46 ppm (2, 6H) is assigned as the $thea^{2-}$ $-CH_2-$, 2.32 ppm (s, 8H) assigned as $thea^{2-}$ $-CH_3$, 4.76 ppm (s, 12H) as tpa $-CH_2-$, 6.24 ppm (s, 4H) as $thea^{2-}$ Ar-H, and 7.40 (s, 12H), 7.72 (t, J = 6 Hz) and 8.97 (s, 6H) ppm as tpa Ar-H (Table S15).

Upon increasing the temperature up to 333 K, the five tpa signals broaden and undergo a significant change in their chemical shift (Figure S58, Table S15). This would occur from increasing paramagnetism due to SCO occurring for $[\{Fe^{III}(tpa)\}_2(thea^{SQ\text{-}SQ})]^{4+}$. In the $[\{Fe^{III}(tpa)\}_2(thea^{SQ\text{-}SQ})]^{4+}$ +2MeCN ⇌ $[Fe^{III}(tpa)(thea^{SQ\text{-}Q})]^{2+}$ + $[Fe^{II}(tpa)(MeCN)_2]^{2+}$ equilibrium, $[Fe^{III}(tpa)(thea^{SQ\text{-}Q})]^{2+}$ likely also undergoes SCO and, $[Fe^{II}(tpa)(MeCN)]^{2+}$ could also show SCO. In solution, compound $[Fe^{II}(tpa)(MeCN)](OTf)_2$ (OTf^- = trifluoromethanesulfonate) displays an increase in magnetic moment with increasing temperature, either due to SCO or replacement of MeCN with OTf^-.[57] To determine if the ligand field of $[Fe^{II}(tpa)(MeCN)]^{2+}$ is correct for SCO, we synthesized the previously reported[58]

$[Ni(tpa)(MeCN)_2](OTf)_2$, and determined the Δ_o to be 11,900 cm^{-1} from the $^3A_{2g} \rightarrow {}^3T_{2g}$ transition in the UV-Vis spectrum. It has been shown that a Δ_o of 11,200–12,400 cm^{-1} can lead to the observation of Fe^{II} SCO.[59] Therefore, it is possible that $[Fe^{II}(tpa)(MeCN)]^{2+}$ also exhibits SCO. The $thea^{2-}$ aromatic proton peak also broadens upon increasing the temperature from 253 to 298 K, with further increasing the temperature resulting in the peaks becoming sharper. The broadening from 253 to 298 K is likely linked to SCO. The subsequent sharpening would suggest minimization of a paramagnetic effect, supporting dissociation of the paramagnetic Fe center from $thea^{2-}$ in the proposed equilibrium. The two aliphatic $thea^{2-}$ peaks do not broaden or shift significantly upon increasing temperature, consistent with protons being removed from the paramagnetic Fe^{III} centers.

To confirm that the observed spectral changes of **3** in d_3-MeCN are a result from both SCO and the proposed equilibrium, we also performed variable temperature ^1H NMR measurements of **3** in CD_2Cl_2 at 0.5 mM (Figure S59). Between 253 and 303 K, the spectra are essentially the same, consistent with the lack of dissociation in DCM. Therefore, **3** in MeCN undergoes a concentration- and temperature-dependent $[\{Fe^{III}(tpa)\}_2(thea^{SQ\text{-}SQ})]^{4+} + 2MeCN \rightleftharpoons [Fe^{III}(tpa)(thea^{SQ\text{-}Q})]^{2+} + [Fe^{II}(tpa)(MeCN)_2]^{2+}$ equilibrium process.

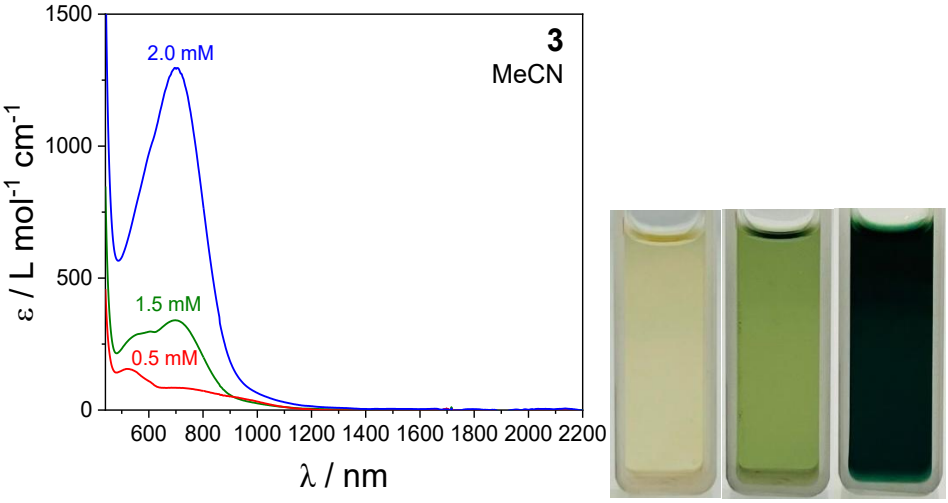

Figure S54. UV-Vis-NIR spectra of **3** in MeCN measured at 0.5 (red), 1.5 (green) and 2.0 mM (blue) at 298 K, with corresponding photographs of 0.5 (left), 1.5 (middle) and 2.0 (right) mM solutions.

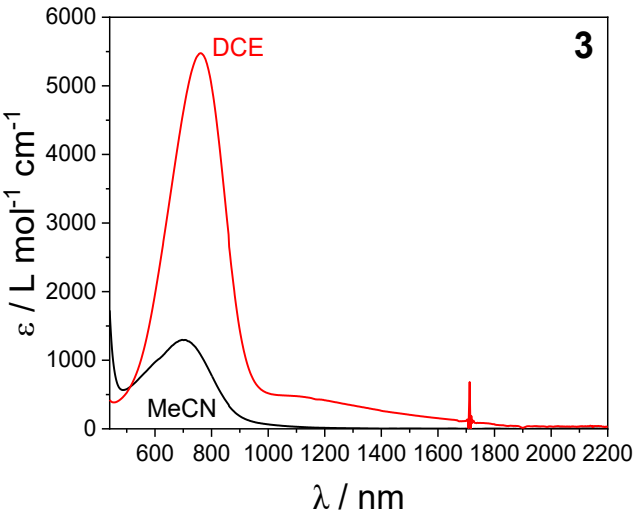

Figure S55. UV-Vis-NIR spectra of **3** in DCE and MeCN (measured at 2.0 mM) at 298 K.

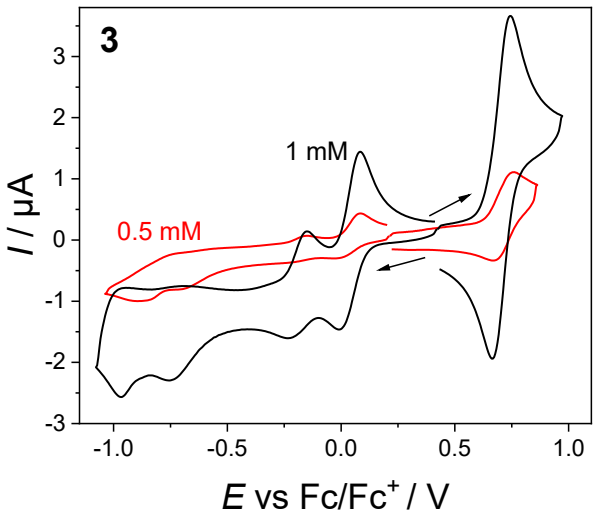

Figure S56. Cyclic voltammograms of MeCN solutions of compounds **3** and 1.0 (black) and 0.5 mM (red) concentrations (0.25 M Bu_4NPF_6) obtained with a scan rate of 100 mV s^{-1}. Arrows indicate the starting point and direction of the scan.

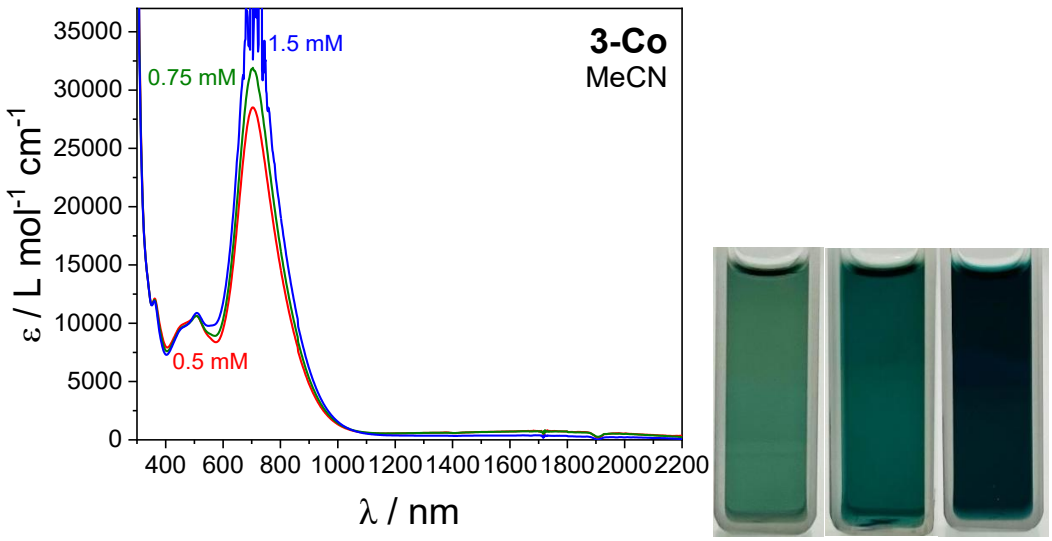

Figure S57. UV-Vis-NIR spectra of **3-Co** in MeCN measured at 0.5 (red), 0.75 (green) and 1.5 mM (blue) at 298 K, with corresponding photographs of 0.5 (left), 0.75 (middle) and 1.5 (right) mM solutions.

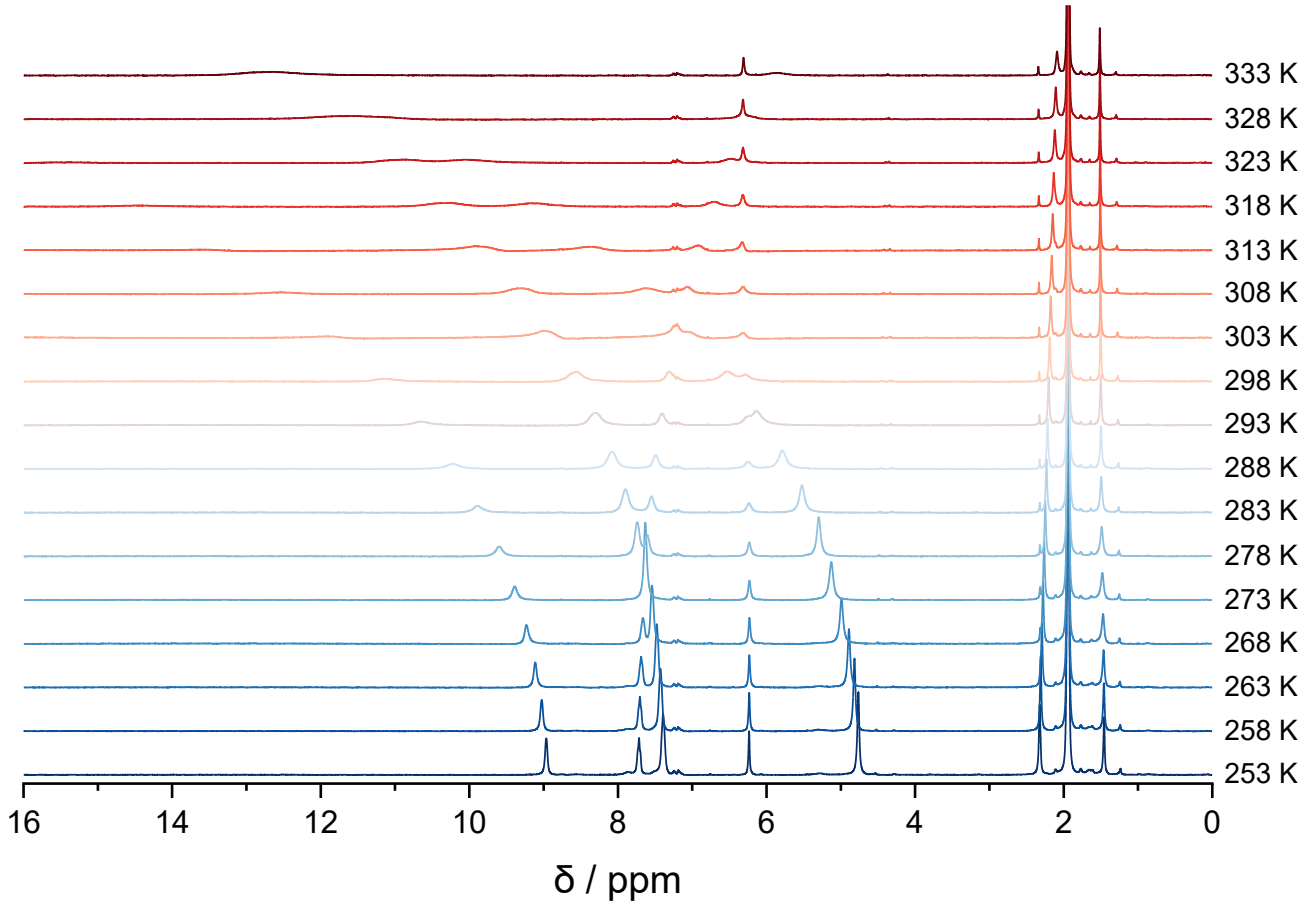

Figure S58. ^{1}H NMR spectra of **3** in d_3-MeCN (0.5 mM) between 253–333 K in 5 K increments.

Table S15. Temperature dependence of the observed chemical shifts (δ) of **3** in d_3-MeCN (0.5 mM) between 253 – 333 K in 5 K increments.

Temperature	δ / ppm						
	tpa_{Ar}	tpa_{Ar}	tpa_{Ar}	$thea_{Ar}$	tpa_{-CH2-}	$thea_{CH3}$	$thea_{-CH2-}$
253 K	8.965	7.716	7.395	6.235	4.764	2.323	1.456
258 K	9.026	7.705	7.428	6.233	4.816	2.309	1.459
263 K	9.113	7.688	7.478	6.231	4.890	2.293	1.463
268 K	9.231	7.665	7.542	6.230	4.991	2.278	1.470
273 K	9.389	7.631	7.631	6.230	5.127	2.264	1.479
278 K	9.600	7.604	7.740	6.232	5.297	2.248	1.488
283 K	9.891	7.549	7.898	6.234	5.525	2.232	1.495
288 K	10.22	7.491	8.077	6.246	5.788	2.218	1.499
293 K	10.65	7.408	8.298	6.270	6.139	2.202	1.501
298 K	11.14	7.310	8.559	6.284	6.528	2.188	1.503
303 K	11.88	7.203	8.972	6.315	7.040	2.174	1.505
308 K	12.54	7.605	9.300	6.316	7.621	2.161	1.507
313 K	13.57	6.917	9.885	6.325	8.366	2.147	1.508
318 K	14.42	6.702	10.317	6.317	9.120	2.134	1.510
323 K	15.46	6.476	10.910	6.316	10.047	2.120	1.511
328 K	>16	6.250	11.622	6.316	11.622	2.107	1.512
333 K	>16	5.841	12.663	6.310	12.663	2.089	1.515

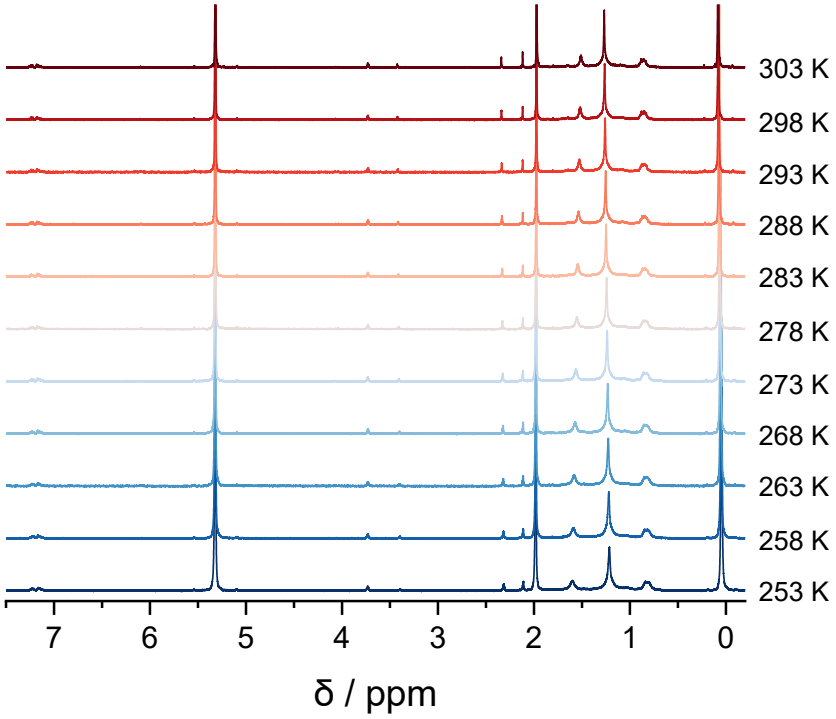

Figure S59. ^{1}H NMR spectra of **3** in CD_2Cl_2 (0.5 mM) between 253–333 K in 5 K increments.

Variable Temperature Electronic Spectroscopy

To support the solution SCO suggested by solution-state magnetic measurements, we performed variable temperature solution UV-Vis measurements on **1**, **2** and **3**. Spectra were recorded in MeCN (273–333 K, Figure S60) and BuCN (273–358 for **1** and **2**, 273–333 K for **3**, Figure S61). The 298 K spectra were recovered for each compound after the complete measurement (Figure S62-S64), indicating reversible interconversion and thermal stability. Upon lowering the temperature, the LMCT bands in **1** undergo a small increase in energy and intensity, with isosbestic points (555, 660 and 1040 nm in MeCN) indicating multiple absorbing species (Figure S60, S61). For **2**, a single isosbestic point is observed (930 nm in MeCN), with cooling resulting in an increase in the intensity and energy of the LMCT bands, and more pronounced $cat^{2-} \rightarrow$ LS-Fe^{III} LMCT shoulders below 900 nm (Figure S60). The low energy $SQ^{\bullet-}$ $\pi \rightarrow \pi^*$ band increases in intensity upon cooling, supporting assignment of the low and high energy $SQ^{\bullet-}$ $\pi \rightarrow \pi^*$ transitions being related to LS-Fe^{III} and the HS-Fe^{III}, respectively. The spectrum of **2** upon cooling approaches the room temperature solid-state spectrum (Figure S50), reflecting increased population of LS-Fe^{III} in the solid-state. For compound **3**, all major features decrease in intensity with increasing temperature across all concentrations (Figure S60, S61, S65, S66), representing a decrease in the *d-d* band intensity and the $SQ^{\bullet-}$ $\pi \rightarrow \pi^*$ process associated with LS-Fe^{III}. However, the observed spectral changes are also likely associated with the products favored in the $[\{Fe^{III}(tpa)\}_2(thea^{SQ\text{-}SQ})]^{4+}$ +2MeCN $\rightleftharpoons$ $[Fe^{III}(tpa)(thea^{SQ\text{-}Q})]^{2+}$ + $[Fe^{II}(tpa)(MeCN)_2]^{2+}$ equilibrium at higher temperatures.

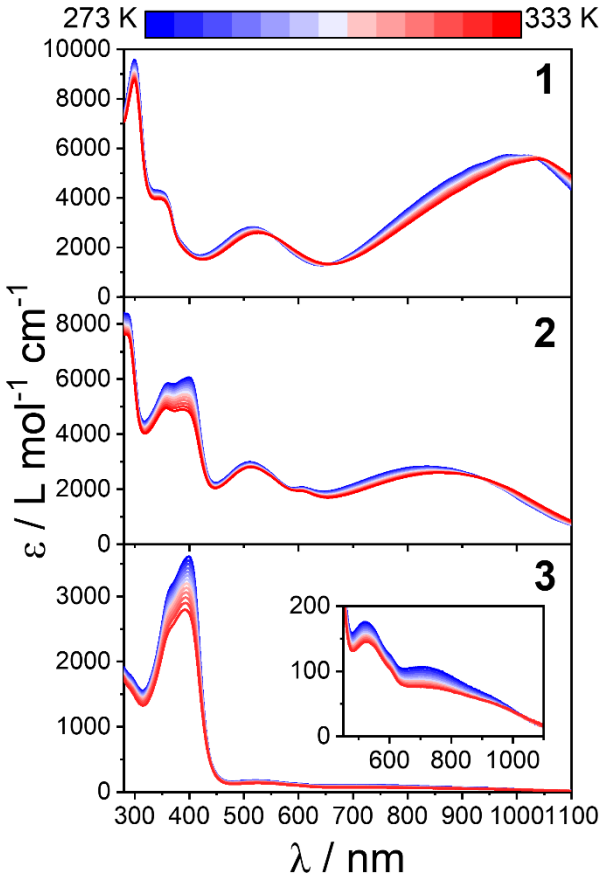

Figure S60. Variable-temperature absorption spectra of **1**, **2** and **3** in MeCN between 273 (blue) and 333 K (red) in 5 K increments.

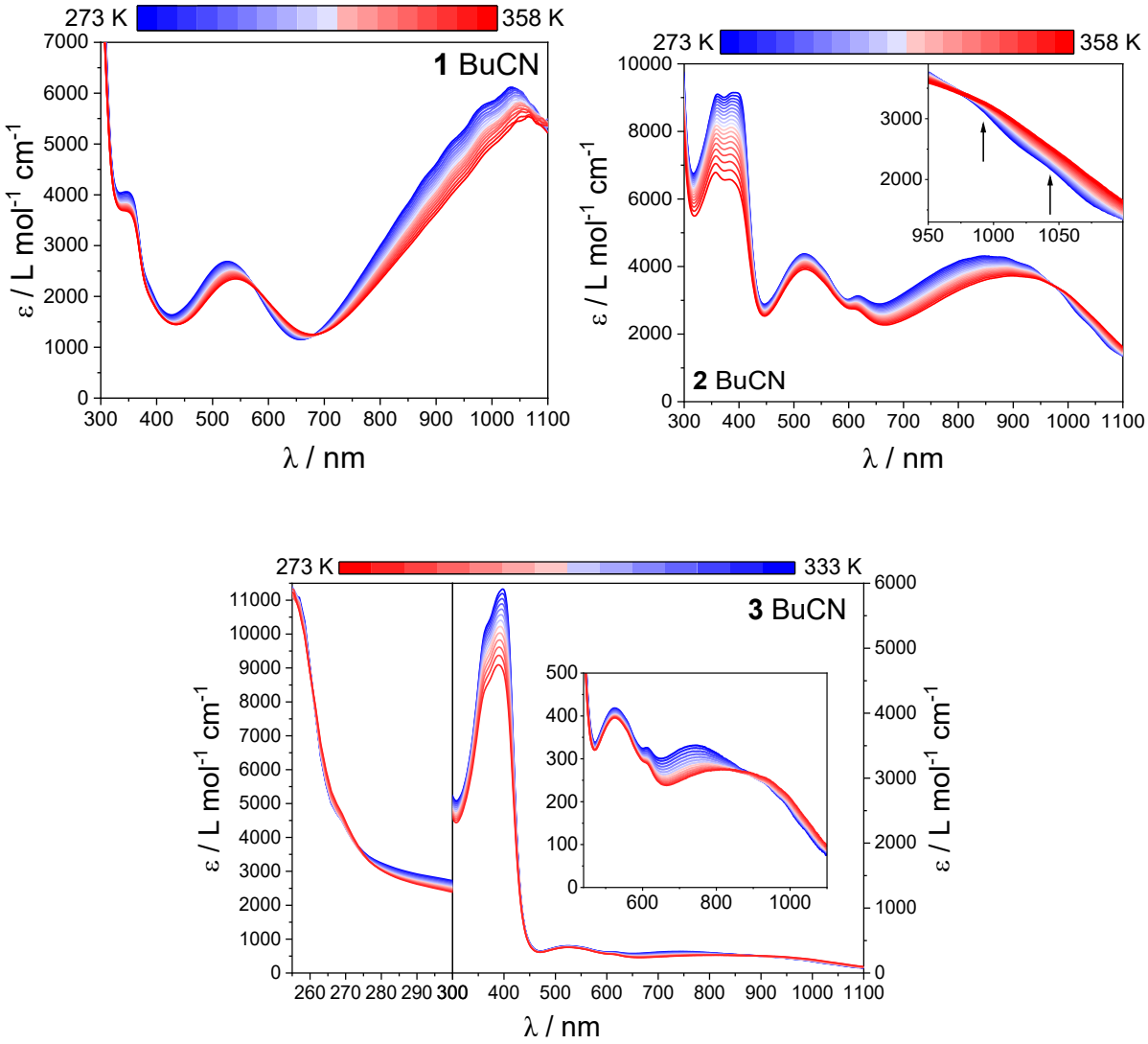

Figure S61. Variable-temperature absorption spectra of **1**, **2** and **3** (0.4 mM) in BuCN between 273 K and 358 K (**1** and **2**) and 333 K (**3**) in 5 K increments.

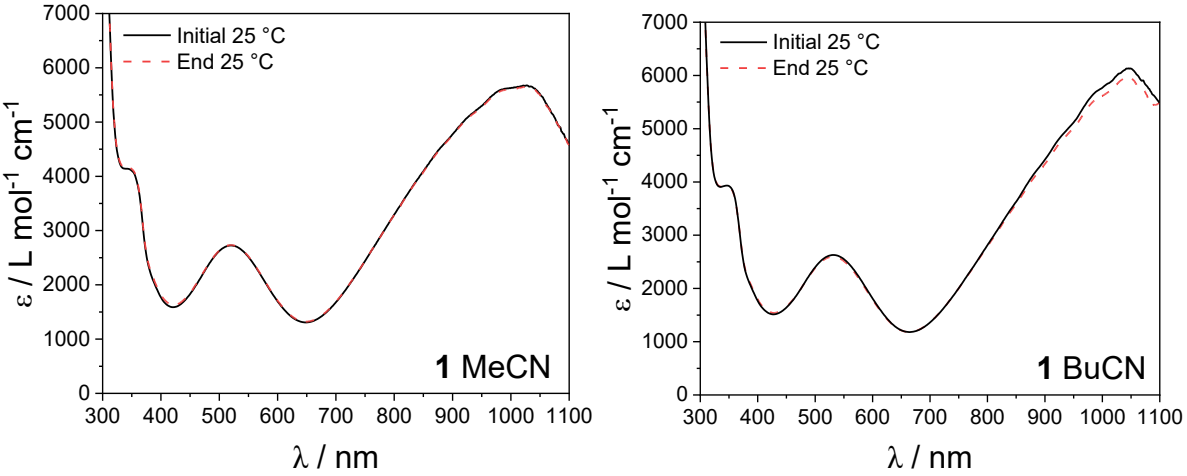

Figure S62. UV-Vis sample of **1** in MeCN and BuCN or DCE at 298 K measured immediately following dissolution (black solid line) and after heating from 273 to 333 (MeCN) or 358 K (BuCN) (red dashed line).

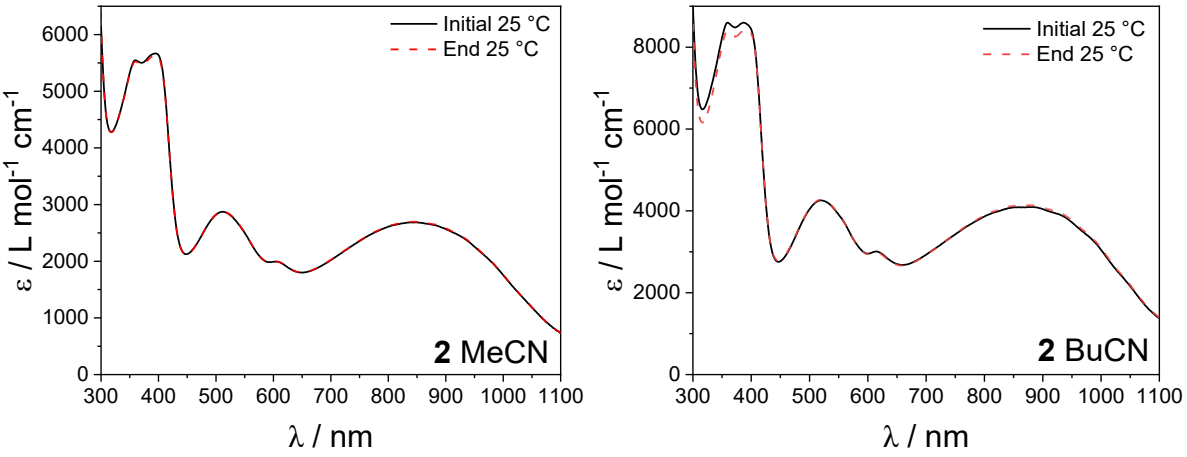

Figure S63. UV-Vis sample of **2** in MeCN and BuCN at 298 K measured immediately following dissolution (black solid line) and after heating from 273 to 333 (MeCN) or 358 K (BuCN) (red dashed line).

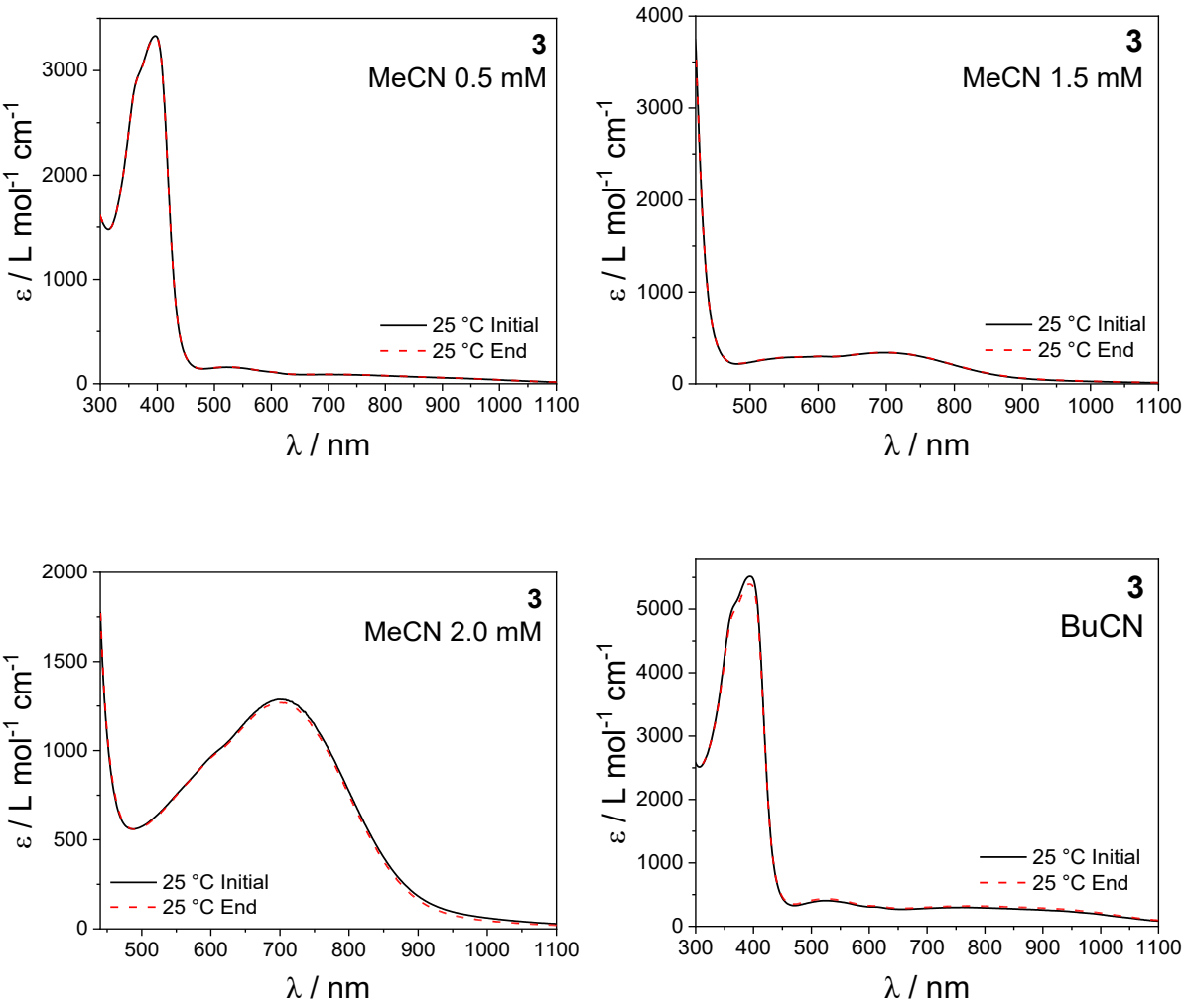

Figure S64. UV-Vis sample of **3** in MeCN and BuCN at 298 K measured immediately following dissolution (black solid line) and after heating from 273 to 333 K (red dashed line).

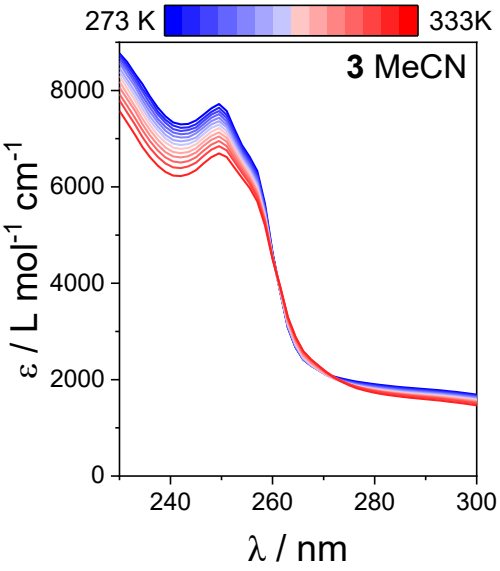

Figure S65. Variable-temperature absorption spectra of **3** in MeCN (0.5 mM) between 273 (blue) and 333 K (red) in 5 K increments in the region 230 – 300 nm, highlighting isosbestic points.

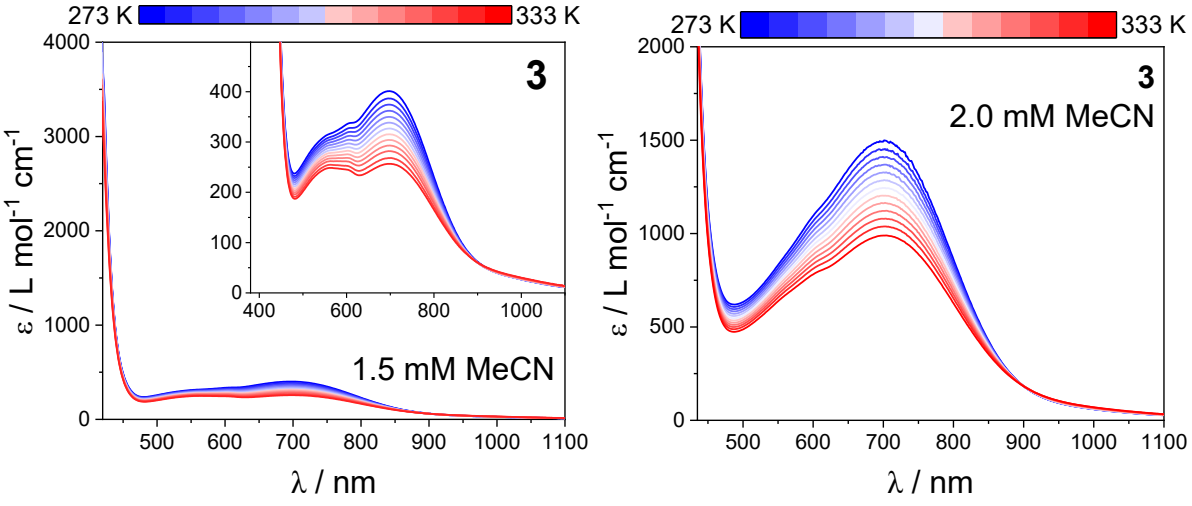

Figure S66. Variable-temperature absorption spectra of **3** in MeCN at 1.5 mM (left) and 2.0 mM (right) between 273 (blue) and 333 K (red) in 5 K increments.

Near-Infrared Spectroscopy

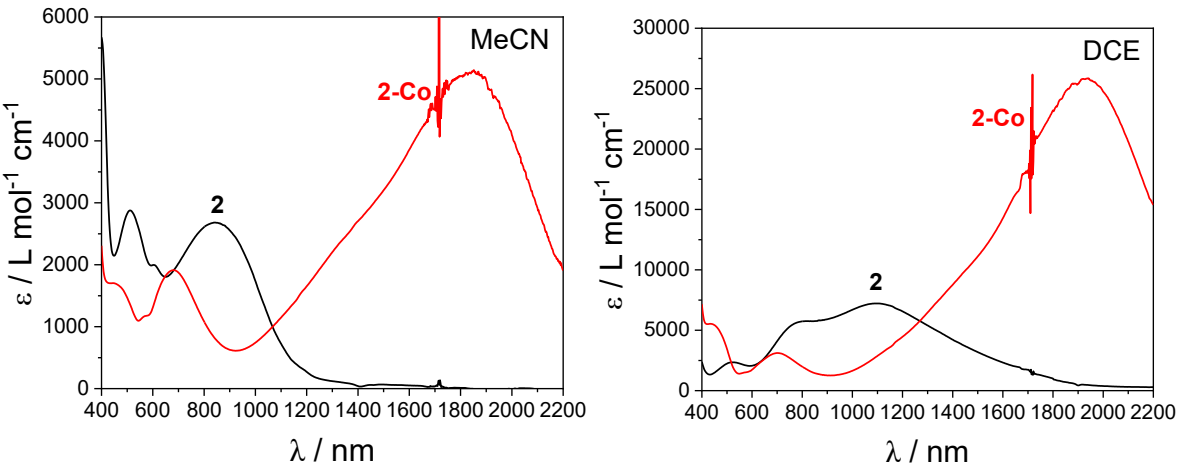

Figure S67. UV-Vis-NIR absorption spectra, of MeCN and DCE solutions of **2** and **2-Co** at 298 K.

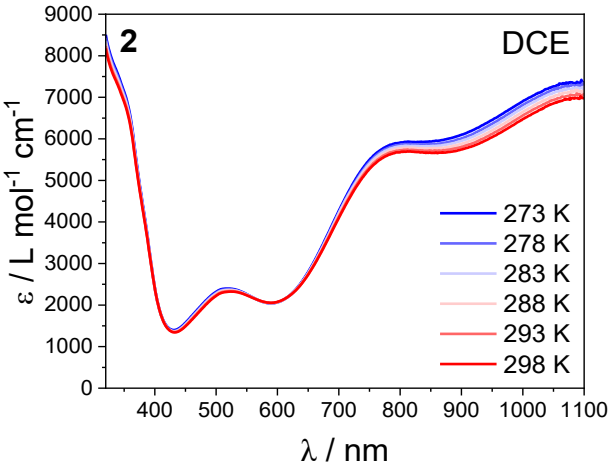

Figure S68. Variable-temperature absorption spectra of **2** in DCE between 273 and 298 K, in 5 K increments.

Robin-Day Mixed-Valence Classification Analysis

The degree of electronic communication can be measured by the Robin and Day mixed-valence (MV) class of ligands.[60] Class I systems have a fully localized electronic structure and therefore have no interactions and electron transfer between the centers, with the electronic coupling parameter (H_{AB}) equal to zero. Class II corresponds to a localized electronic structure and solvent interaction, with a non-zero H_{AB} and a IVCT band with energy $h\nu_{max}$ and full width at half maximum, $\Delta\nu_{1/2}$. The IVCT band for class II are typically solvent-dependent ($\Delta\nu_{max}$ > 200 cm^{-1} for a range of dielectric constant of 30), weak in intensity (ε_{max} < 5000 L mol^{-1} cm^{-1}), broad ($\Delta\nu_{1/2}$ > 2000 cm^{-1}), H_{AB} < 800 cm^{-1}, and $2H_{AB}/\nu_{max} \ll 1$.[61–64] Class II-III correspond to localized electronic structure and averaged solvent interactions, with $0.7 < 2H_{AB}/\nu_{max} < 1$, and class III represent electronic and solvent delocalization with $2H_{AB}/\nu_{max} \gg 1$.[61,65] Both MV class II-III and III contain IVCT that are solvent independent ν_{max} < 200 cm^{-1} for a range of dielectric constant of 30), narrow ($\Delta\nu_{1/2}$ < 2000 cm^{-1}), and intense (ε_{max} > 5000 L mol^{-1} cm^{-1}).[62]

The MV class can be determined by parameter Γ, given by:

$$\Gamma = 1 - (\Delta\upsilon_{1/2})/(\Delta\upsilon_{1/2}^{\circ}) \qquad \text{(eq. S2)}$$

where $\nu_{1/2}^{\circ}$ is the theoretical bandwidth at half maximum (in cm^{-1}) of the IVCT band as given by:[65]

$$(\Delta\upsilon_{1/2}^{\circ})^2 = 16k_{\mathrm{B}}T\nu_{\mathrm{max}}\ln 2 \qquad \text{(eq. S3)}$$

where k_B is the Boltzmann constant and T is the temperature in K. For a spectrum measured at 298 K, this gives:

$$\Delta\upsilon_{1/2}^{\circ} = 47.93\sqrt{\nu_{max}} \qquad \text{(eq. S4)}$$

A value of Γ < 0.5 indicate class II, $\Gamma \approx 0.5$ indicate class II-III and Γ > 0.5 indicate class III.

For organic MV compounds, the H_{AB} is 0 for MV class I, up to ~800 cm^{-1} for MV class II,[63,64]~1000-2000 cm^{-1} for MV class II-III[27,55,63] and 2500-5500 cm^{-1} for MV class III.[63,64]

According to the Hush model,[60,66] H_{AB} can be calculated using:

$$H_{AB1} = \frac{2.06\times10^{-2}(\nu_{max}\varepsilon_{max}\Delta\nu_{1/2})^{1/2}}{r_{ab}} \quad \text{(eq. S5)}$$

Where ε_{max} (L mol^{-1} cm^{-1}) is the molar absorptivity at ν_{max} and r_{AB} is the distance (Å) between the two centers, approximated as the average distance between the centroids of the three N-C-C-N (r_{AB} = 7.4 Å for **2**).[27,64]

According to the Brunschwig-Sutin model,[67] which uses complementary electrochemistry data to calculate the comproportionation equilibrium constant (K_c) for the reaction: $SQ^{\bullet-}$-$SQ^{\bullet-}$ + cat^{2-}-cat^{2-} ⇌ 2(cat^{2-}-$SQ^{\bullet-}$):

$$\Delta G_c^\circ = -RTlnk_c = -F(\Delta diox) \quad \text{(eq. S6)}$$

Where G_c° is the Gibbs free energy of the comproportionation reaction (J mol^{-1}), F is Faraday's constant (95485 C mol^{-1}), and $\Delta diox$ is the separation (0.25 V) between the redox processes I and II in **2** as detailed in the main text. For partially delocalized complexes, H_{AB} is calculated using:

$$H_{AB2} = (\frac{-\Delta G_r^\circ \nu_{max}}{2})^{1/2} \approx (\frac{-\Delta G_c^\circ \nu_{max}}{2})^{1/2} \quad \text{(eq. S7)}$$

where ΔG_c° is the Gibbs free energy of the comproportionation reaction (cm^{-1}), approximated as the Gibbs free energy due to the electronic interactions by delocalized, ΔG_r°, in the case of small non-resonance contributions. In the case for a fully delocalized system, H_{AB} is calculated using:

$$H_{AB2} = \frac{-\Delta G_r^\circ}{2} + \frac{\nu_{max}}{4} \approx \frac{-\Delta G_c^\circ}{2} + \frac{\nu_{max}}{4} \quad \text{(eq. S8)}$$

Values above the upper limit of H_{AB}:

$$H_{AB3} = \frac{\nu_{max}}{2} \quad \text{(eq. S9)}$$

Correspond to MV class III complexes.

Table S16. Mixed-valence and IVCT parameters for complex **2** in DCE.

ν_{max} / cm^{-1}	$\Delta\nu_{1/2}$ / cm^{-1}	$\Delta\nu_{1/2}°$ / cm^{-1}	Γ			
8770(2)[a]	3960(30)[a]	4490[b]	0.12[c]			
$\Delta diox$ / mV	**$\Delta G_c°$ / kJ mol^{-1}**	**H_{AB1} / cm^{-1}**	**($2H_{AB1}/\nu_{max}$)**	**H_{AB2} / cm^{-1}**	**($2H_{AB2}/\nu_{max}$)**	**H_{AB3} / cm^{-1}**
250	−23.9[d]	1330[e]	0.30	2960[f] (3190)[g]	0.68	4390[h]

[a]From Gaussain fit. [b] Determined using eq. S4. [c] Determined using eq. S2. [d] Determined using eq. S6. [e] Determined using eq. S5. [f] Determined using eq. S7. [g] Value in bracket represents a fully delocalized system, calculated using eq. S8. [h] calculated using eq S9.

Electrochemistry

Table S17. Cyclic Voltammetry and Rotating Disk Electrode Voltammetric Data for Compounds **1**, **2**, **3** in MeCN (1.0 mM analyte with 0.25 M Bu_4NPF_6).[a]

	Cyclic Voltammetry E_m or E_{pa} / V (ΔE_p / mV)[b]				**Rotating Disk Electrode Voltammetry $E_{1/2}$ / V (i_L / µA)[c]**		
	I	II	III	IV	I	II	III
1	−0.23 (155)	0.04 (103)	0.70 (95)	−0.98[d]	−0.20 (10)	0.06 (18)	0.72 (35)
2	−0.20 (100)	0.05 (90)	0.71 (90)	−0.94[d]	−0.18 (22)	0.13 (21)	0.72 (53)
3	−0.19 (83)	0.04 (90)	0.70 (80)	−0.76, −0.97[d]	−0.17 (10)	0.06 (22)	0.70 (52)

[a] Potentials reported vs Fc/Fc^+ couple. [b] Mid-point potentials (E_m) determined by taking average of peak anodic potential (E_{pa}) and peak cathodic potential (E_{pc}). Peak separation (ΔE_p) between the E_{pa} and E_{pc} is given when possibile. [c] half-wave potentials ($E_{1/2}$) and limiting currents (i_L) are given for processes I, II, III. Process IV not included as it is irreversible. [d] E_{pa} rather than E_m due to irreversibility.

Density Functional Theory: Geometry Optimization, Spin Density, Exchange Coupling

To ensure that the UOPBE/6-311+ +G(d,p) method captures the experimental observations correctly, we compared the calculated and experimentally determined geometry (at 100 K) of **1**, **2** and **3**. The experimental structure at 100 K of **1**, **2** and **3** match well with the calculated [LS-HS], [LS-LS], and [LS-LS] state, respectively (Figure S73-S75). For **2**, the average calculated Fe−N/O bond lengths for the [LS-HS] and [HS-HS] states now compare with the structures of **2** between 300 and 350 K, and 350 K, respectively (Figure S74).

As expected, the spin density (q_s) distribution of **1**, **2** and **3** in all three spin states is primarily located on the Fe^{III} centers (Figure S76, Table S19). The expected q_s value for LS-Fe^{III} and HS-Fe^{III} is 1 and 5, respectively. For **1**, the q_s values of 0.39 and 3.56 for the LS-Fe^{III} and HS-Fe^{III} centers in all three states, respectively, are lower than the expected values (Table S19). This is due to partial shift of the spin density onto $thea^{4-}$, and formation of some Fe^{II}-SQ character. This multiconfigurational ground state is supported by EPR measurements. For **2**, the q_s values for the LS-Fe^{III} (0.82–0.87) and HS-Fe^{III} (3.70–3.73) across all the spin states are higher than **1**, consistent with suppression of formation of Fe^{II}-SQ. For **3**, the q_s values for LS-Fe^{III} (1.23–1.24) are now higher than expected for LS-Fe^{III}, indicating mixing of the spin on the iron and $SQ^{\bullet-}$ centers. For HS-Fe^{III}, the values (3.87–3.89) are still lower than the expected value of 5.

It was expected that the spin density distribution in $thea^{3\bullet-}$ in **2** would be localized on one dioxolene unit, reflecting the experimentally verified localized cat^{2-}-$SQ^{\bullet-}$ description. However, across all three spin states the geometry converges such that the bond lengths of the two dioxolene units in **2** are similar (Figure S70) and the spin-density distribution is delocalized across the $thea^{3\bullet-}$ bridge (Figure S76). It was also expected that the spin density distribution in

the of **2** would increasingly localize in the [LS-HS] state. However, minimal change to the spin distribution is observed across the three states. In the previous study of **2-Co**,[3] the utilized UTPSSh/6-311++G(d,p) method reproduced the localized spin distribution of thea$^{3\bullet-}$. However, the UTPSSh significantly over-stabilizes LS-Fe^{III} states,[32,34] and was therefore unsuitable for reliable describing the spin state energies of **1**, **2** and **3**. We instead employed the UOPBE/6-311++G(d,p) method, which is more accurately captured Fe^{III} spin state energies.[2,68–70] While OPBE improves spin-state energetics, it appears to result in increased electron delocalization, likely due to the commonly observed self-interaction error,[71,72] in which electrons display unphysical interaction with themselves. Correcting this error is non-trivial,[73] and is beyond the scope of this study.

We performed additional calculations on **2** to observe if changes occurred to the radical delocalization. The [LS-LS], [LS-HS], and [HS-HS] states of **2** were reoptimized using OPBE/Def2-TZVP within the SMD continuum solvation model (acetonitrile, butyronitrile, dichloroethane, and toluene).[24] In all cases, bond-length equalization and spin delocalization persisted (Figure S78-S81). Inclusion of the PF_6^- anion was also examined. The [LS-HS] state of **2** was optimized with inclusion of the three PF_6^- anions, using two different initial configurations (two anions close to either the LS-Fe^{III} or HS-Fe^{III} center). Calculations were first performed using the combined b97-3c approximation, which includes the def2-mTZVP basis and the GD3BJ dispersion correction (SMD, solvent = acetonitrile). When the two anions are placed initially near the LS-Fe^{III} center, there are no significant changes in geometry during optimization. However, when two anions were initially placed near the HS-Fe^{III} center, one anion migrated toward the molecular center during optimization, yielding a structure favored by ~4 kcal mol^{-1} (Figure S82). Recalculation at the OPBE/Def2-TZVP level reduced this energetic preference to <1 kcal mol^{-1} (Figure S83), suggesting that dispersion corrections exaggerate this effect. In all cases, the optimized geometries favored a symmetric arrangement

of the anions and retained delocalized spin density across the bridge. Thus, irrespective of solvent model, counterion inclusion, or starting geometry, this DFT method consistently converges to a symmetric, delocalized electronic structure for **2**. The persistence of this solution indicates that the delocalized state represents the lowest-energy solution within the chosen DFT method. The discrepancy with the experimentally determined localized cat^{2-}-$SQ^{\bullet-}$ state is therefore attributed to intrinsic limitations of approximate DFT methods in treating mixed-valent systems.

The estimation of the exchange spin coupling J (in cm^{-1}; $= -JS_1 \cdot S_2$ formalism) was carried out by means of calculation of all possible charge distributions with the use of UTPSSh[74,75] functional and 6-311++G(d,p) basis set in the framework of 'broken symmetry' (BS) formalism with the generalized spin-projection method developed by Yamaguchi.[76,77] The exchange coupling parameters J ($-2J\hat{S}_1 \cdot \hat{S}_2$ formalism) between the two Fe^{III} centers (**1**, **2** and **3**), Fe^{III} center and $SQ^{\bullet-}$ (**2** and **3**) and the two $SQ^{\bullet-}$ (**3**) for the three spin states was calculated to be antiferromagnetic (Table S20), consistent with experimental observation. The overlap of the magnetic π-orbitals produces effective antiferromagnetic exchange channels (Figure S77). The calculated values are a magnitude larger than experimentally determined, and we note that while the signs of these calculated coupling constants are likely reliable, the accuracy of the absolute value is uncertain.[78–82]

Table S18. Spin states (S), total energies without (E) and with (E^{ZPE}) zero-point harmonic vibrations, total enthalpies (H^{298}) and expectation values of the spin-squared operator ($\hat{S}^2$) of the compounds **1**, **2** and **3** as calculated by the DFT UOPBE/6-311++G(d,p) method.

Charge Distribution		S	E / a.u.	E^{ZPE} / a.u.	H^{298} / a.u.	$\hat{S}^2$
1	[LS-cat-cat-LS]	1	-5353.892842	-5352.955345	-5352.898395	2.014
	[LS-cat-cat-HS]	3	-5353.890673	-5352.956048	-5352.897479	12.037
	[HS-cat-cat-HS]	5	-5353.888247	-5352.956837	-5352.896585	30.065
2	[LS-cat-SQ-LS]	3/2	-5353.561080	-5352.622759	-5352.567427	3.779
	[LS-cat-SQ-HS]	7/2	-5353.556788	-5352.621113	-5352.562496	15.781
	[HS-cat-SQ-HS]	11/2	-5353.551722	-5352.620402	-5352.560221	35.779
2-*meso*	[LS-cat-SQ-LS]	3/2	-5353.561281	-5352.622650	-5352.565625	3.779
	[LS-cat-SQ-HS]	7/2	-5353.557138	-5352.621094	-5352.563282	15.781
	[HS-cat-SQ-HS]	11/2	-5353.552752	-5352.620456	-5352.561795	35.779
3	[LS-SQ-SQ-LS]	2	-5353.135927	-5352.197014	-5352.139836	6.040
	[LS-SQ-SQ-HS]	4	-5353.125156	-5352.189601	-5352.130691	20.030
	[HS-SQ-SQ-HS]	6	-5353.113736	-5352.181363	-5352.121774	42.019

Table S19. Spin states (S), relative energies (ΔE), relative energies with zero-point harmonic vibrations (ΔE^{ZPE}), relative enthalpies (ΔH^{298}) (all values are given in kcal mol^{-1}) and the amount of spin density at the metal centers (q_s^{Fe1}, q_s^{Fe2}) of the compounds **1**, **2** and **3** as calculated by the DFT UOPBE/6-311++G(d,p) method.

Charge Distribution		S	ΔE	ΔE^{ZPE}	ΔH^{298}	q_s^{Fe1}	q_s^{Fe2}
1	[LS-cat-cat-LS]	1	0.0	0.9	0.0	0.39	0.39
	[LS-cat-cat-HS]	3	1.4	0.5	0.6	0.39	3.56
	[HS-cat-cat-HS]	5	2.9	0.0	1.1	3.56	3.56
2	[LS-cat-SQ-LS]	3/2	0.0	0.0	0.0	0.83	0.82
	[LS-cat-SQ-HS]	7/2	2.7	1.0	3.1	0.87	3.70
	[HS-cat-SQ-HS]	11/2	5.9	1.5	4.5	3.73	3.73
2-*meso*	[LS-cat-SQ-LS]	3/2	0.0	0.0	0.0	0.83	0.83
	[LS-cat-SQ-HS]	7/2	2.6	1.0	1.5	0.89	3.70
	[HS-cat-SQ-HS]	11/2	5.4	1.4	2.4	3.73	3.73
3	[LS-SQ-SQ-LS]	2	0.0	0.0	0.0	1.23	1.23
	[LS-SQ-SQ-HS]	4	6.8	4.7	5.7	1.24	3.87
	[HS-SQ-SQ-HS]	6	13.9	9.8	11.3	3.89	3.89

Table S20. Spin states (*S*), total energies (*E*), expectation values of the spin-squared operator ($\hat{S}^2$) and exchange spin parameters (*J*) of the compounds **1**, **2** and **3** as calculated by the DFT UTPSSh/6-311++G(d,p) method. [a] α corresponds to spin-up, β corresponds to spin-down.

	Charge Distribution	*S*	*E* / a.u.	$\hat{S}^2$	$J_{Fe1\text{-}Fe2}$ / cm^{-1}	$J_{Fe1\text{-}SQ1}$ / cm^{-1}	$J_{SQ1\text{-}Fe2}$ / cm^{-1}	$J_{SQ\text{-}SQ}$ / cm^{-1}
1	[LS-cat-cat-LS]	1	-5354.937570	2.038	-187	–	–	–
	[LS-cat-cat-LS] βα[a]	0	-5354.938477	0.972				
	[LS-cat-cat-HS]	3	-5354.920405	12.048	-36	–	–	–
	[LS-cat-cat-HS] βα	2	-5354.921238	6.993				
	[HS-cat-cat-HS]	5	-5354.903194	30.059	-5	–	–	–
	[HS-cat-cat-HS] βα	0	-5354.903804	5.015				
2	[LS-cat-SQ-LS]	3/2	-5354.595884	3.831	-201	-1096	-1096	–
	[LS-cat-SQ-LS] ααβ	1/2	-5354.603634	1.266				
	[LS-cat-SQ-LS] αβα	1/2	-5354.609120	1.180				
	[LS-cat-SQ-LS] βαα	1/2	-5354.603634	1.266				
	[LS-cat-SQ-HS]	7/2	-5354.579199	15.812	-37	-1087	-240	–
	[LS-cat-SQ-HS] ααβ	3/2	-5354.585881	5.252				
	[LS-cat-SQ-HS] αβα	5/2	-5354.591617	9.165				
	[LS-cat-SQ-HS] βαα	5/2	-5354.586694	9.227				
	[HS-cat-SQ-HS]	11/2	-5354.560336	35.785	-13	-281	-281	–
	[HS-cat-SQ-HS] ααβ	1/2	-5354.568670	5.199				
	[HS-cat-SQ-HS] αβα	9/2	-5354.573982	25.137				
	[HS-cat-SQ-HS] βαα	1/2	-5354.568670	5.199				
3	[LS-SQ-SQ-LS]	2	-5353.279197	6.074	-11	-484	-478	-1549
	[LS-SQ-SQ-LS] βααα	1	-5353.280923	2.197				
	[LS-SQ-SQ-LS] αβαα	1	-5353.286805	2.623				
	[LS-SQ-SQ-LS] ββαα	0	-5353.291259	1.344				
	[LS-SQ-SQ-LS] αββα	0	-5353.289591	1.329				
	[LS-SQ-SQ-LS] αβαβ	0	-5353.291369	1.324				

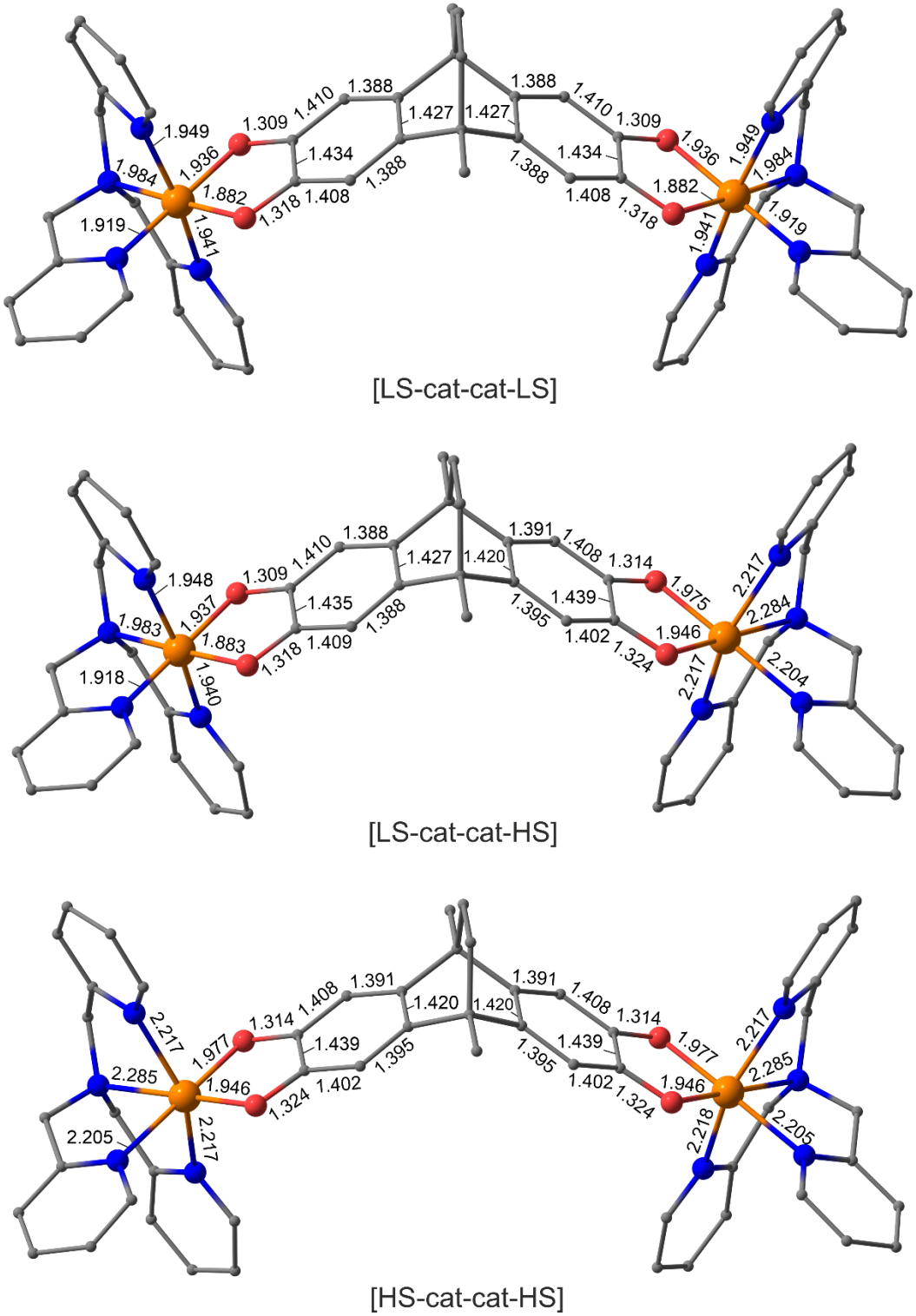

Figure S69. Optimized geometries of the [LS-LS], [LS-HS], and [HS-HS] states of **1** as calculated by the DFT UOPBE/6-311++G(d,p) method. Hydrogen atoms have been omitted for clarity.

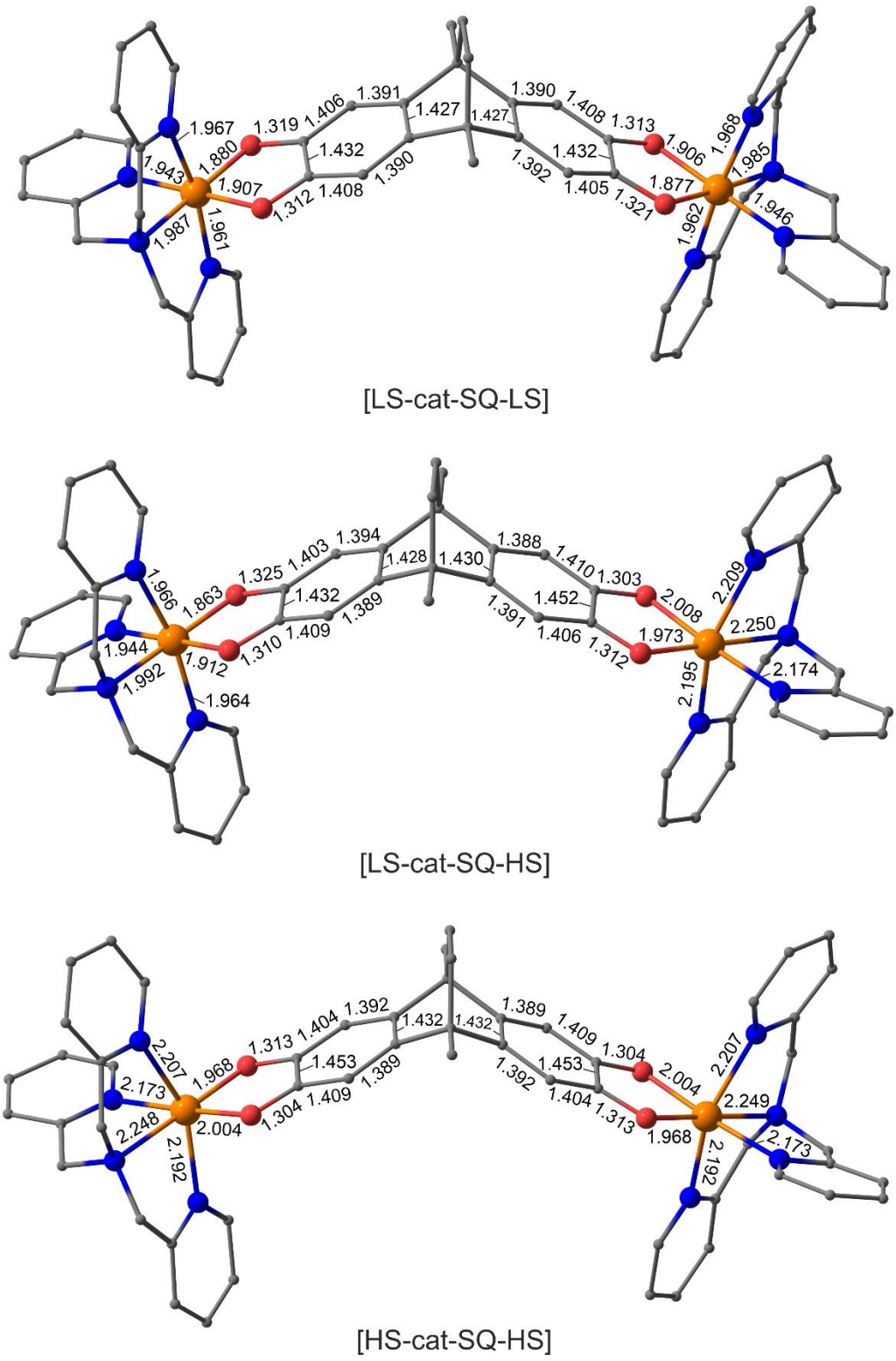

Figure S70. Optimized geometries of the [LS-LS], [LS-HS], and [HS-HS] states of **2** as calculated by the DFT UOPBE/6-311++G(d,p) method. Hydrogen atoms have been omitted for clarity.

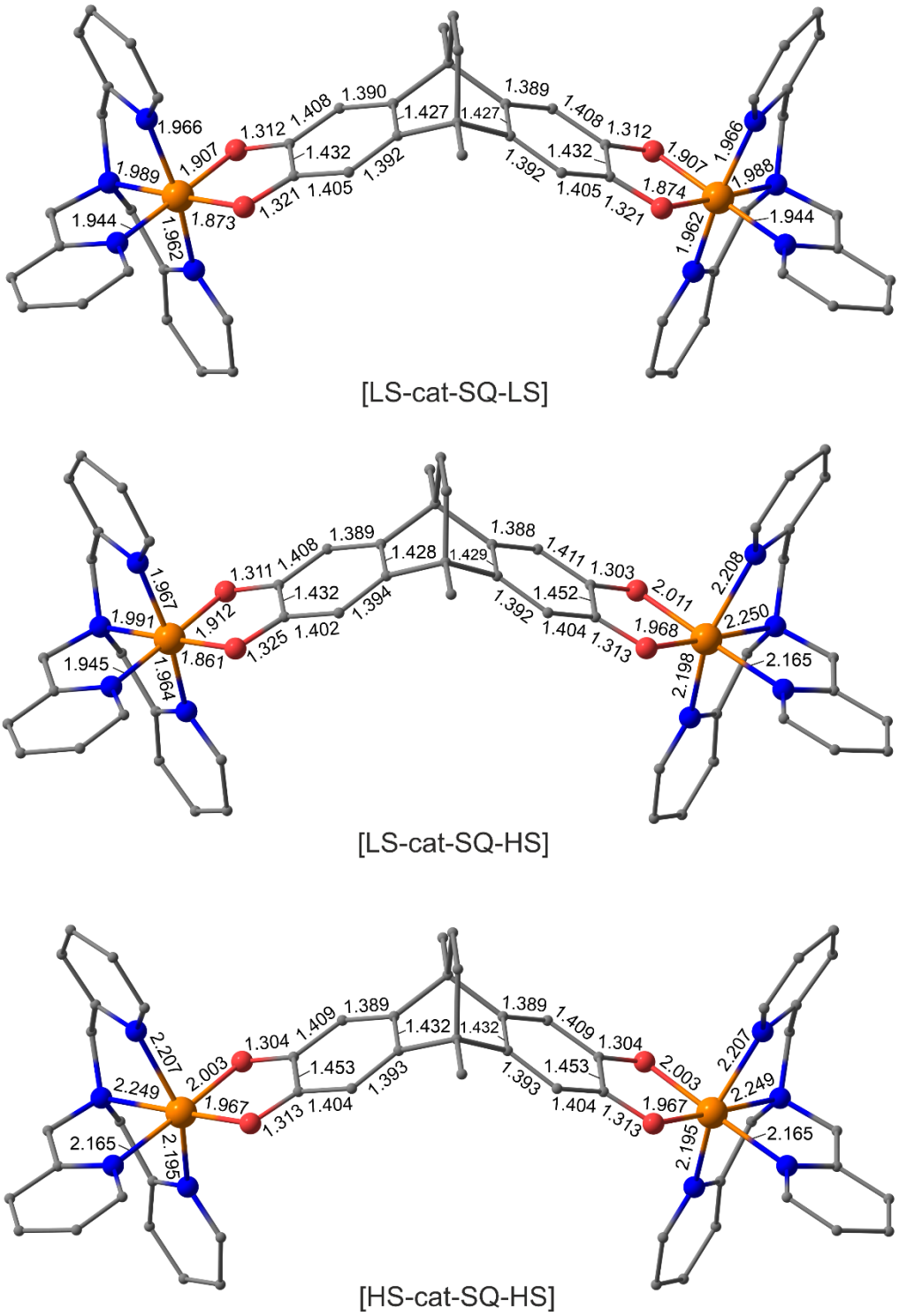

Figure S71. Optimized geometries of the [LS-LS], [LS-HS], and [HS-HS] states of **2-*meso*** as calculated by the DFT UOPBE/6-311++G(d,p) method. Hydrogen atoms have been omitted for clarity.

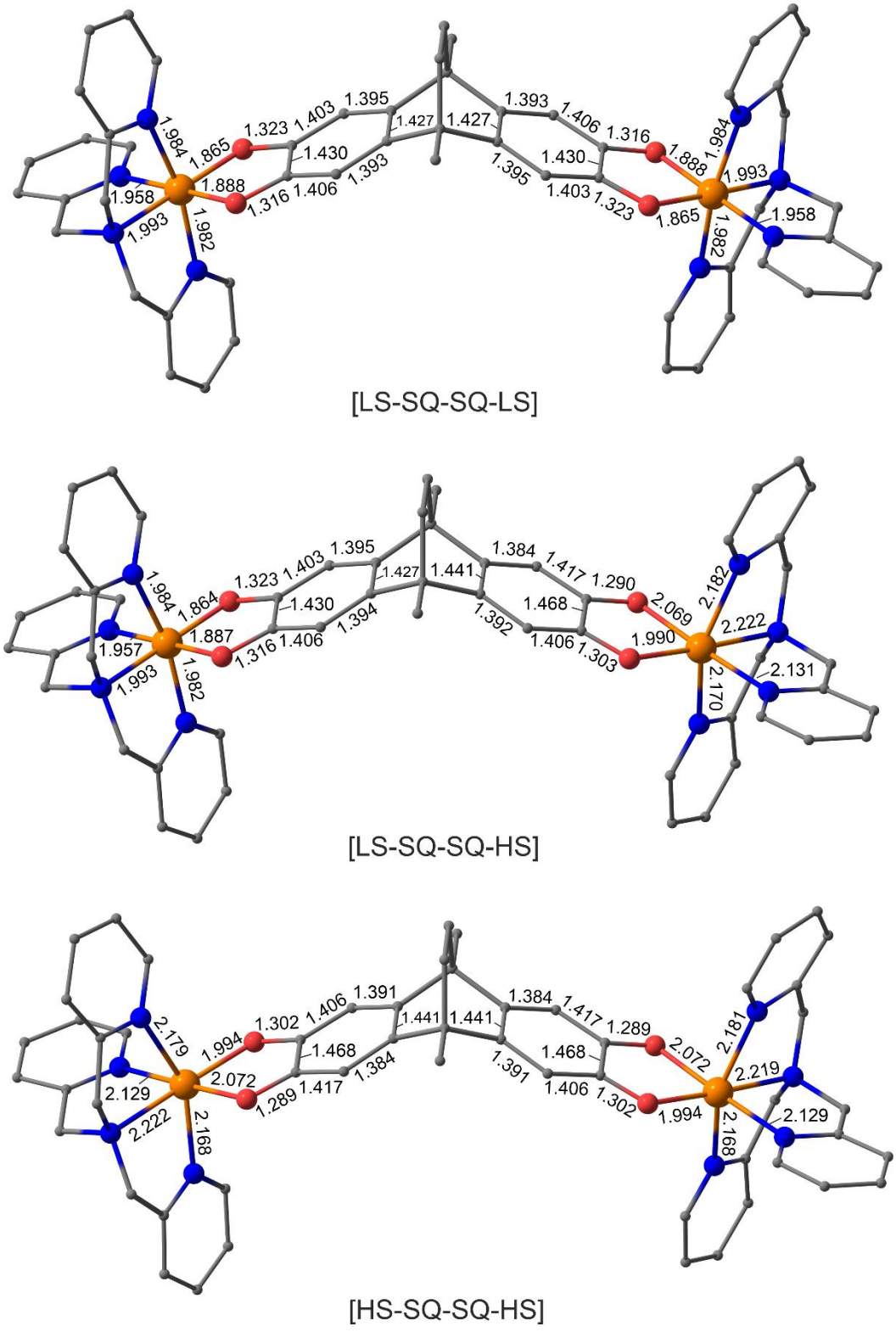

Figure S72. Optimized geometries of the [LS-LS], [LS-HS], and [HS-HS] states of **3** as calculated by the DFT UOPBE/6-311++G(d,p) method. Hydrogen atoms have been omitted for clarity.

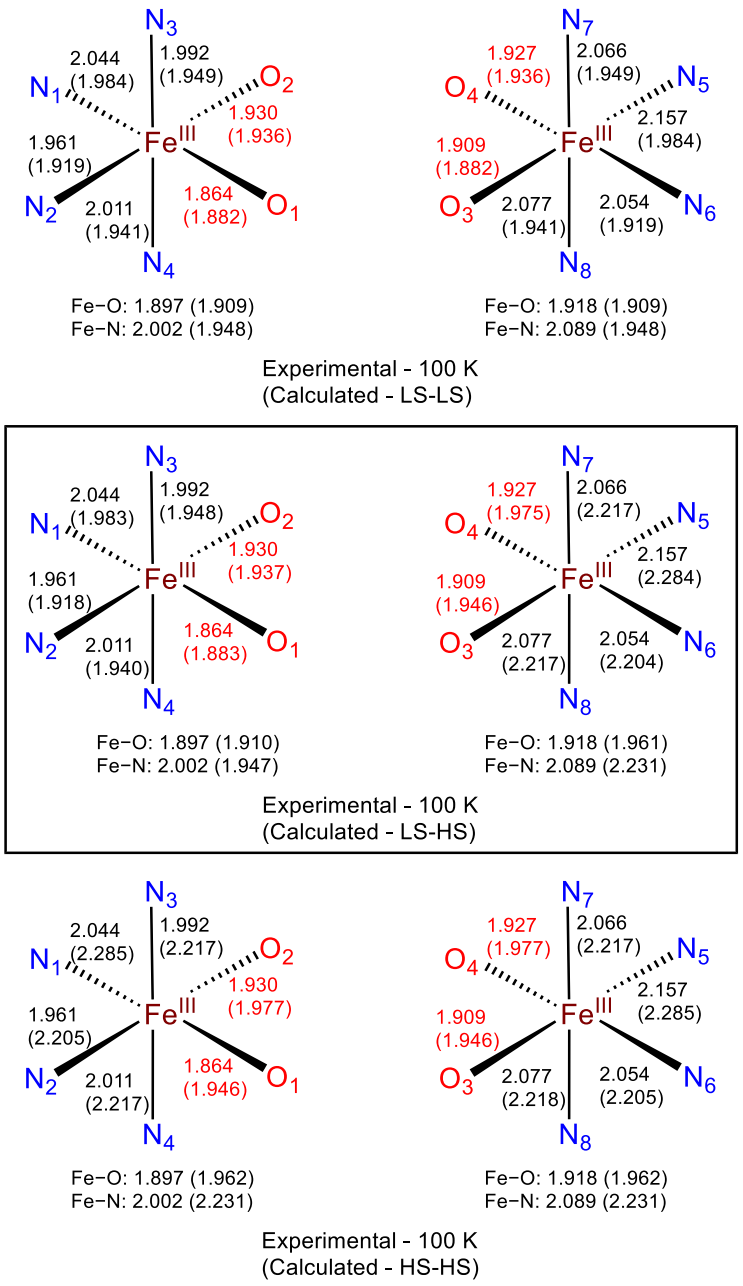

Figure S73. Comparison of the average experimental bond length of the two complexes (100 K) for compound **1**·Et_2O with the gas phase calculated bond length values for the [LS-LS] (top), [LS-HS] (middle) and [HS-HS] (bottom) states for **1**. Experimental values listed above and calculated values listed below in brackets. Best match between experimental and calculated geometries are highlighted in boxes.

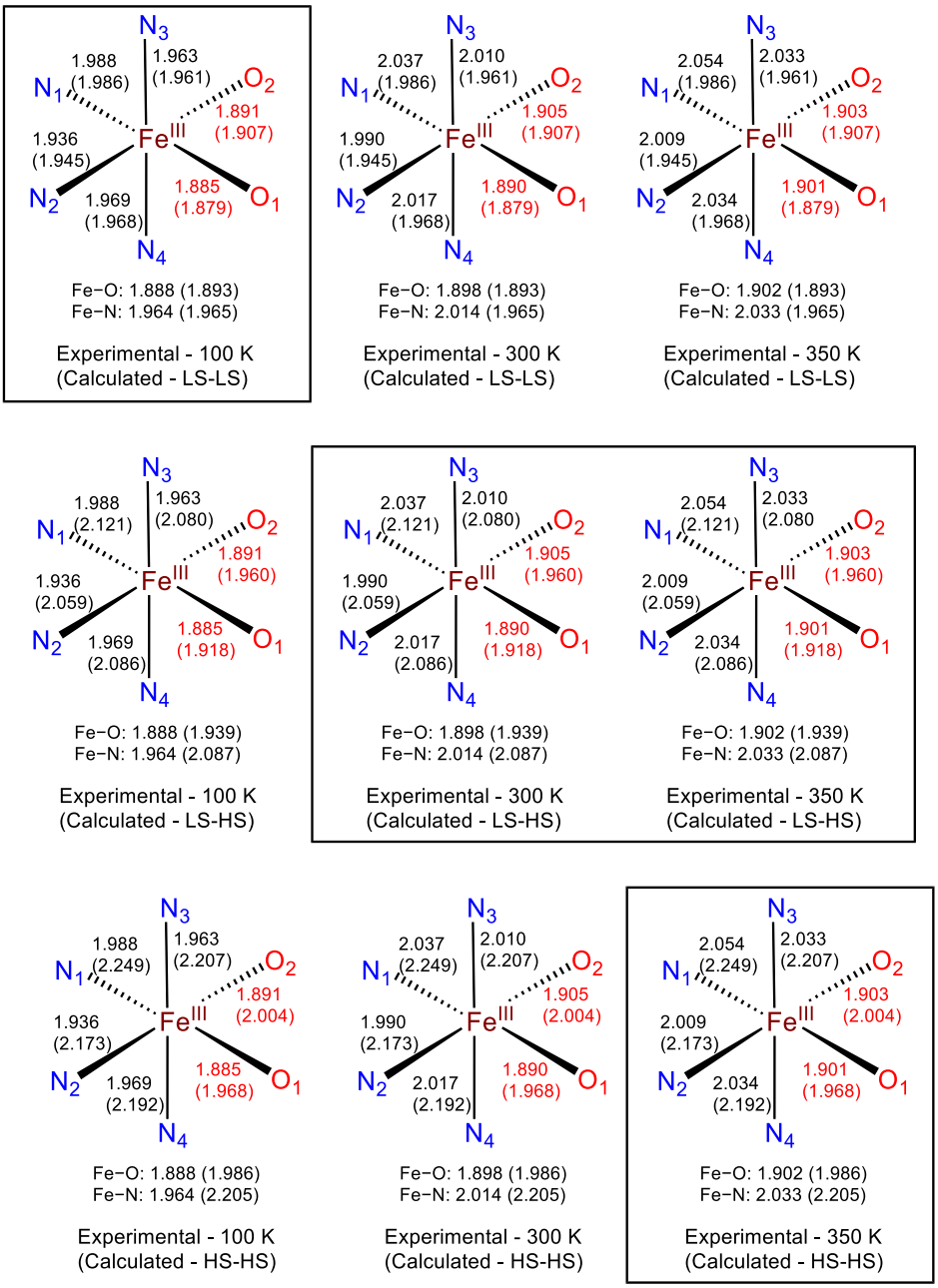

Figure S74. Comparison of the experimental bond length (100, 300 and 350 K) for compound **2**·3toluene·2MeCN with the average gas phase calculated bond length values for the [LS-LS] (top), [LS-HS] (middle) and [HS-HS] (bottom) states for **2**. Experimental values listed above and calculated values listed below in brackets. Best match between experimental and calculated geometries are highlighted in boxes.

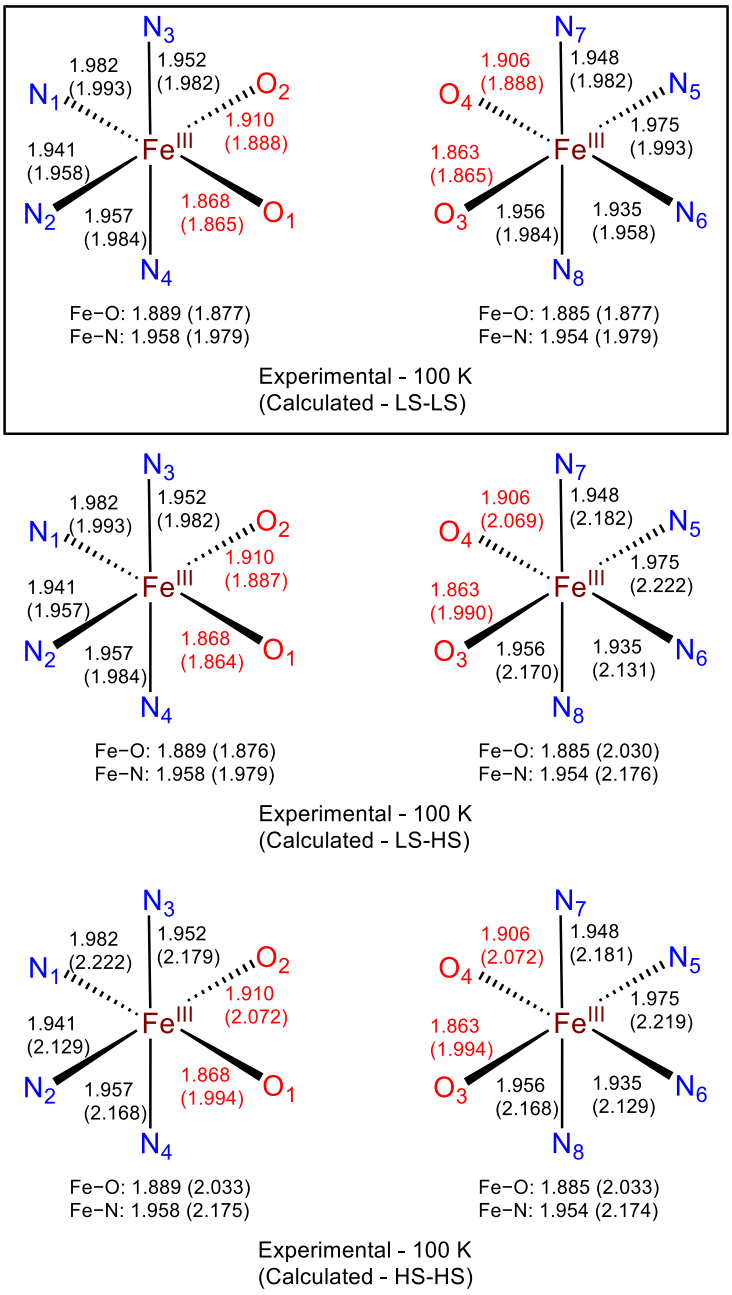

Figure S75. Comparison of the experimental bond length (100 K) for compound **3**·2MeCN·3*i*Pr$_2$O with the gas phase calculated bond length values for the [LS-LS] (top), [LS-HS] (middle) and [HS-HS] (bottom) states for **3**. Experimental values listed above and calculated values listed below in brackets. Best match between experimental and calculated geometries are highlighted in boxes.

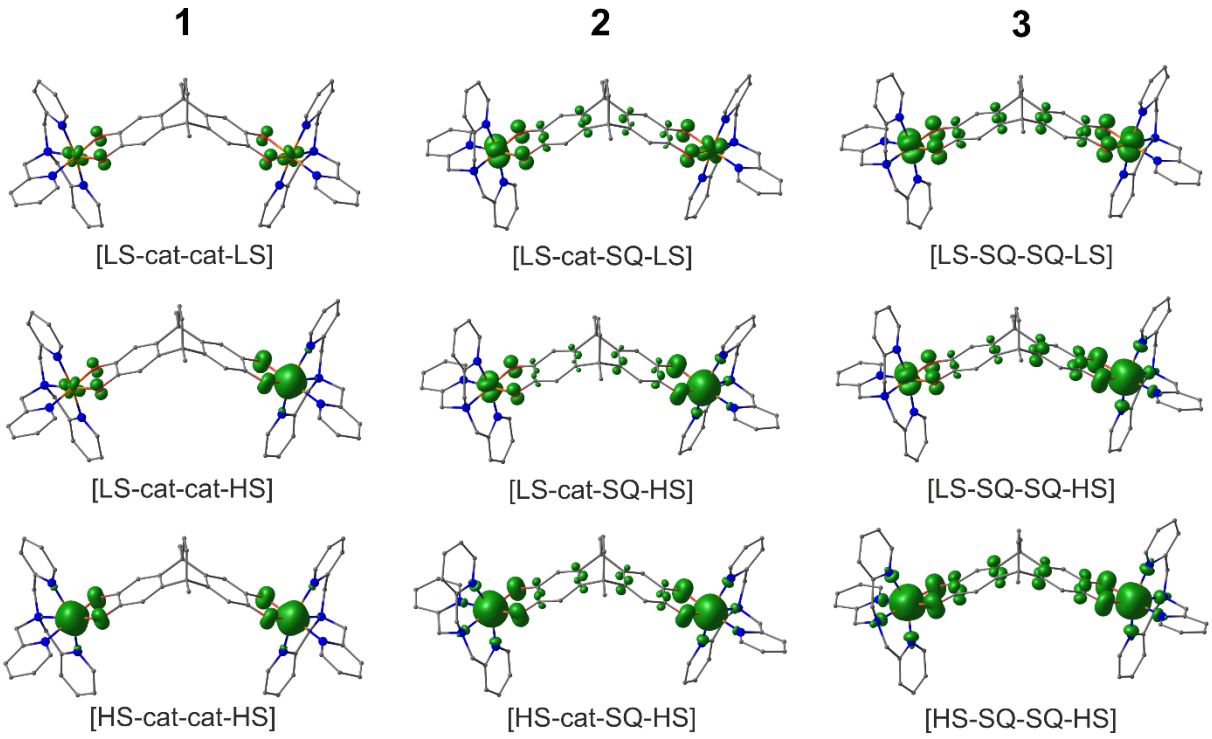

Figure S76. Spin density distribution in the [LS-LS], [LS-HS], and [HS-HS] states of **1**, **2** and **3** as calculated by the DFT UOPBE/6-311++G(d,p) method (contour value = 0.015 e/Å^3).

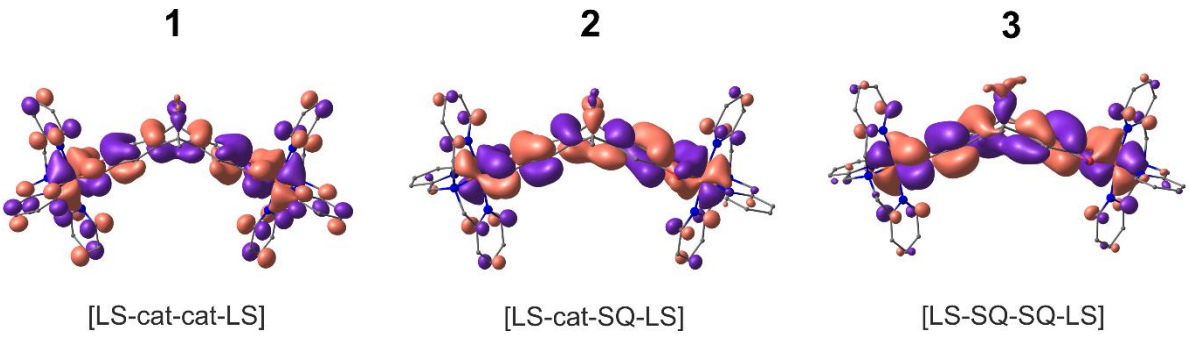

Figure S77. Magnetic orbitals in the [LS-LS] states of **1**, **2** and **3** illustrating antiferromagnetic exchange channels as calculated by the DFT UOPBE/6-311++G(d,p) method (contour value = 0.015 e/Å^3).

Table S21. Spin states (S), total energies (E), relative energies (ΔE), the amount of spin density at the metal centers (q_s^{Fe1}, q_s^{Fe2}) and expectation values of the spin-squared operator ($\hat{S}^2$) of the [LS-LS], [LS-HS], and [HS-HS] states of the compound **2** as calculated by the DFT UOPBE/Def2-TZVP (SMD, solvent = MeCN, BuCN, DCE, toluene) method.

Charge Distribution		S	E, a.u.	ΔE, kcal mol^{-1}	q_s^{Fe1}	q_s^{Fe2}	$\hat{S}^2$
$\mathbf{2}_{\mathbf{MeCN}}$	[LS-cat-SQ-LS]	3/2	-5354.313744	0.0	0.92	0.92	3.783
	[LS-cat-SQ-HS]	7/2	-5354.307250	4.1	1.12	4.12	15.784
	[HS-cat-SQ-HS]	11/2	-5354.298994	9.3	4.17	4.17	35.775
$\mathbf{2}_{\mathbf{BuCN}}$	[LS-cat-SQ-LS]	3/2	-5354.313509	0.0	0.92	0.92	3.783
	[LS-cat-SQ-HS]	7/2	-5354.306005	4.7	1.13	4.11	15.783
	[HS-cat-SQ-HS]	11/2	-5354.298983	9.1	4.17	4.17	35.775
$\mathbf{2}_{\mathbf{DCE}}$	[LS-cat-SQ-LS]	3/2	-5354.292642	0.0	0.91	0.91	3.783
	[LS-cat-SQ-HS]	7/2	-5354.285161	4.7	1.10	4.12	15.782
	[HS-cat-SQ-HS]	11/2	-5354.278605	8.8	4.17	4.17	35.775
$\mathbf{2}_{\mathbf{toluene}}$	[LS-cat-SQ-LS]	3/2	-5354.179412	0.0	0.86	0.86	3.781
	[LS-cat-SQ-HS]	7/2	-5354.172783	4.2	0.97	4.12	15.782
	[HS-cat-SQ-HS]	11/2	-5354.168347	6.9	4.16	4.16	35.777

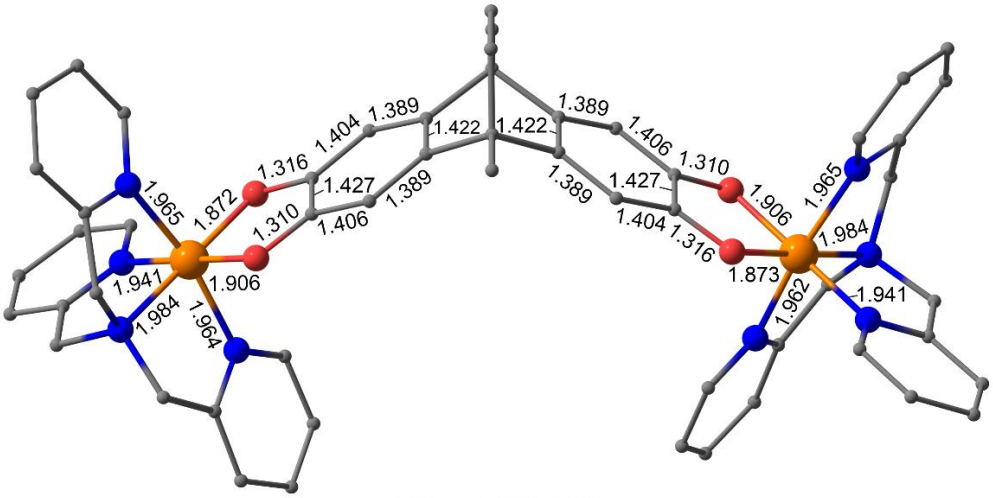

[LS-cat-SQ-LS]

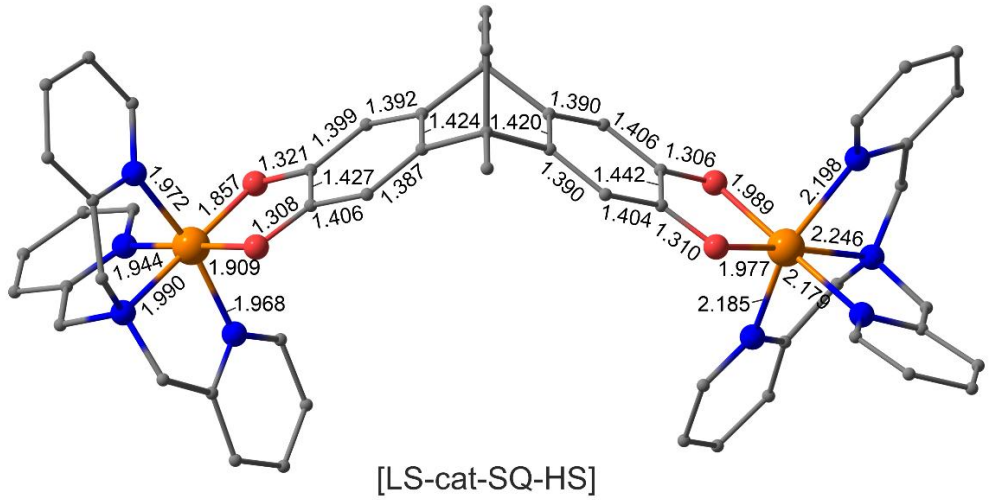

[LS-cat-SQ-HS]

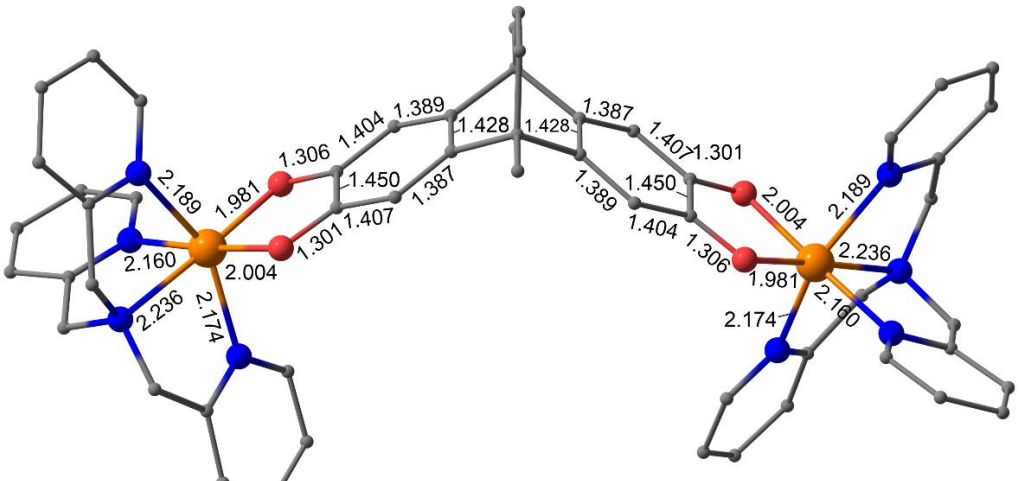

[HS-cat-SQ-HS]

Figure S78. Optimized geometries of the [LS-LS], [LS-HS], and [HS-HS] states of **2** as calculated by the DFT UOPBE/Def2-TZVP (SMD, solvent = MeCN) method. Hydrogen atoms have been omitted for clarity.

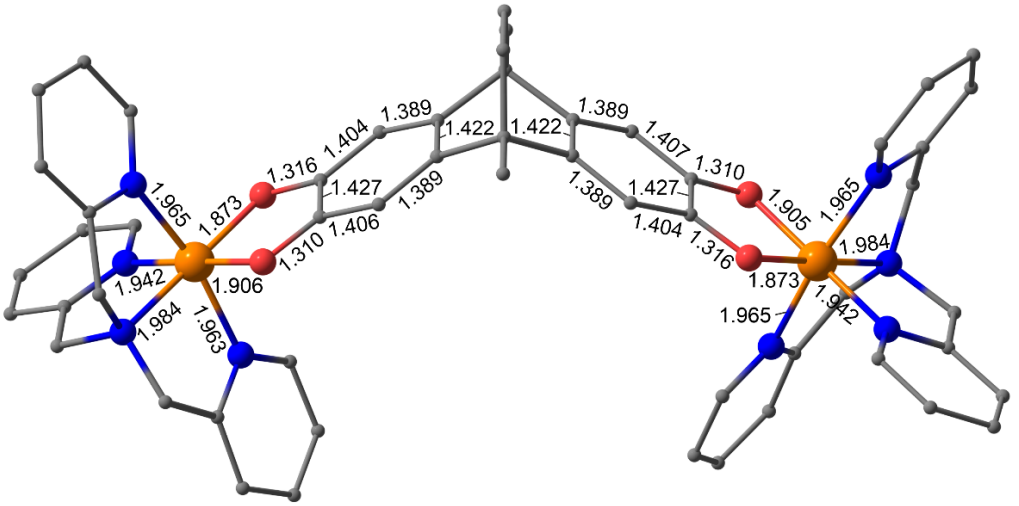

[LS-cat-SQ-LS]

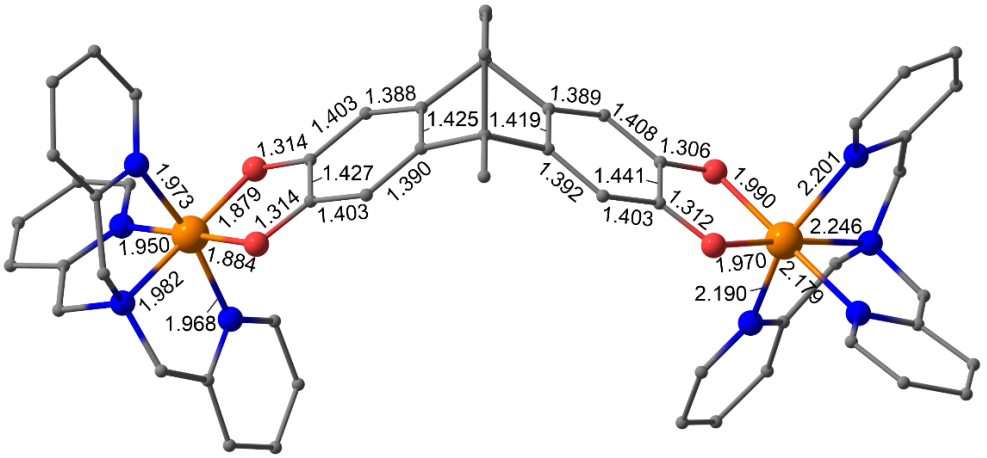

[LS-cat-SQ-HS]

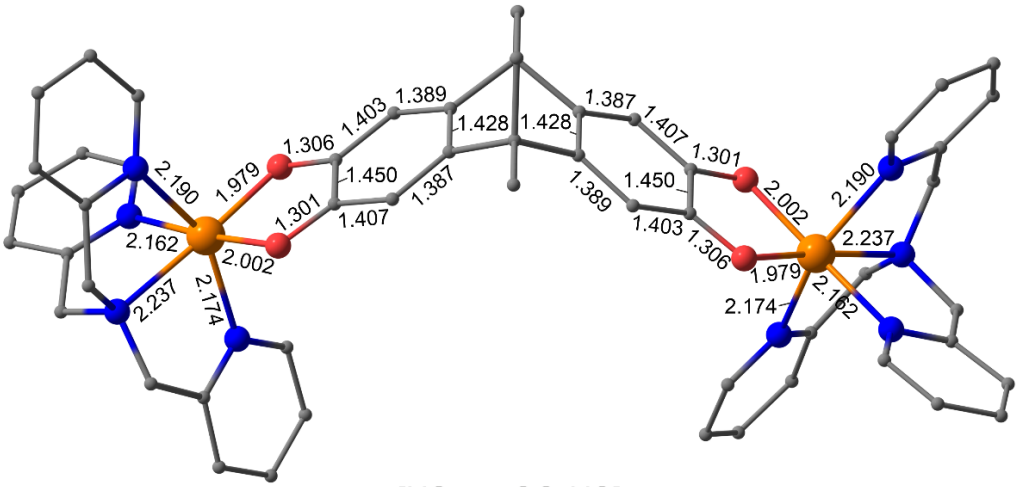

[HS-cat-SQ-HS]

Figure S79. Optimized geometries of the [LS-LS], [LS-HS], and [HS-HS] states of **2** as calculated by the DFT UOPBE/Def2-TZVP (SMD, solvent = BuCN) method. Hydrogen atoms have been omitted for clarity.

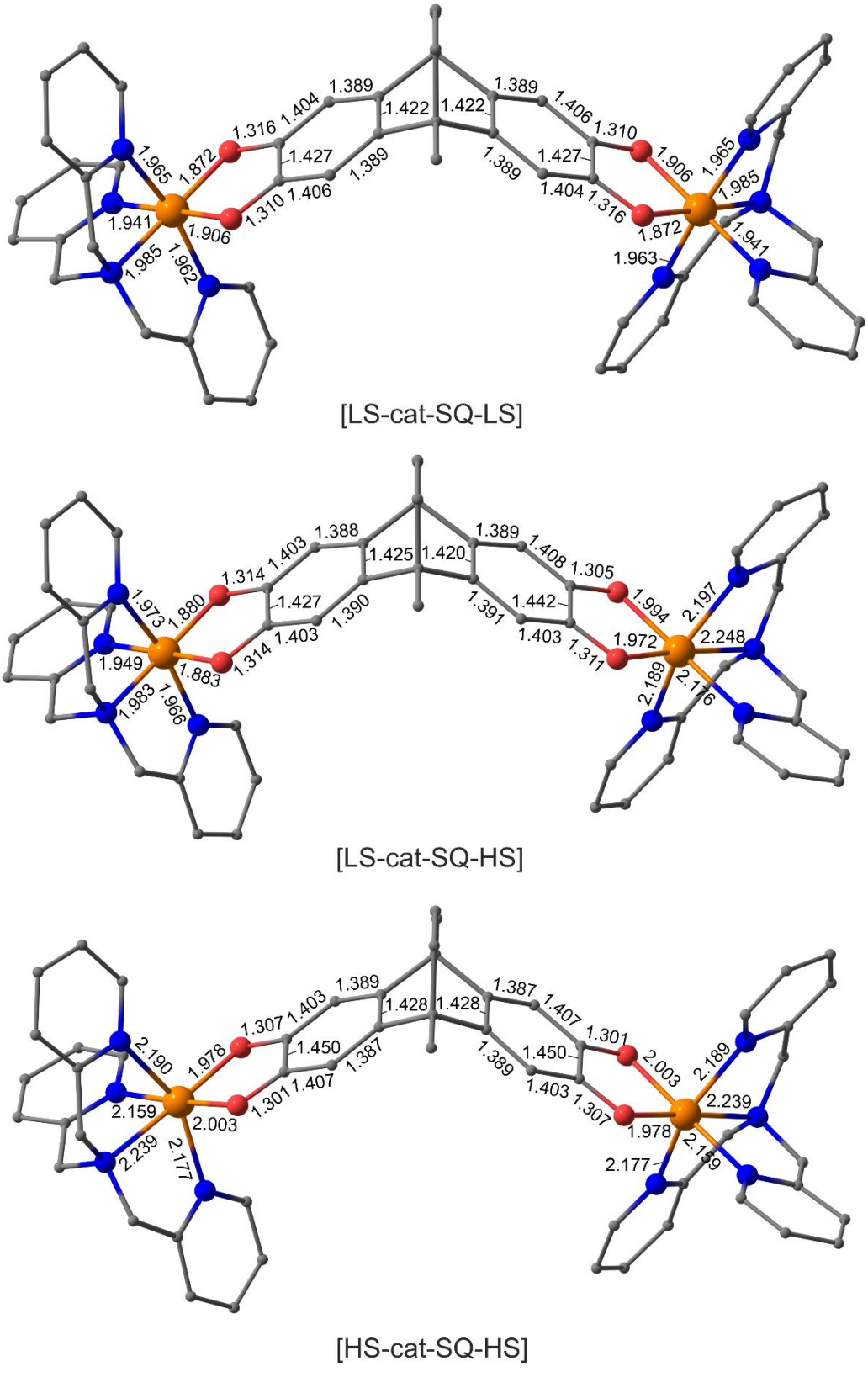

Figure S80. Optimized geometries of the [LS-LS], [LS-HS], and [HS-HS] states of **2** as calculated by the DFT UOPBE/Def2-TZVP (SMD, solvent = DCE) method. Hydrogen atoms have been omitted for clarity.

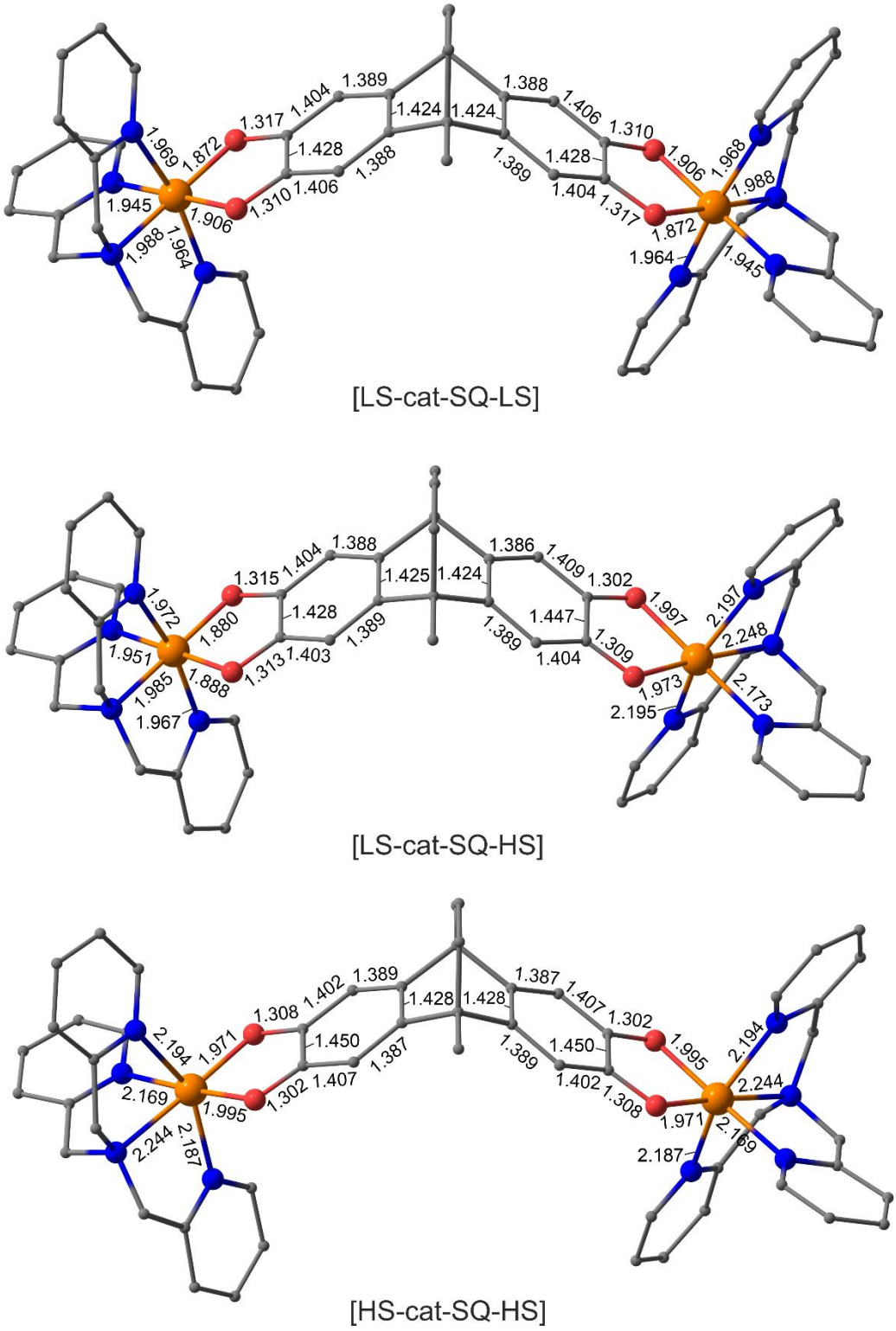

Figure S81. Optimized geometries of the [LS-LS], [LS-HS], and [HS-HS] states of **2** as calculated by the DFT UOPBE/Def2-TZVP (SMD, solvent = toluene) method. Hydrogen atoms have been omitted for clarity.

Table S22. Spin states (S), total energies (E), relative energies (ΔE), the amount of spin density at the metal centres (q_s^{Fe1}, q_s^{Fe2}) and expectation values of the spin-squared operator ($\hat{S}^2$) of the [LS-HS] state of the compound **2** as calculated by the DFT UOPBE/B97-3c (SMD, solvent = MeCN) and DFT UOPBE/Def2-TZVP (SMD, solvent = MeCN) methods with inclusion of the PF_6^- counterions into the computational scheme.

Charge Distribution	S	E, a.u.	ΔE, kcal mol^{-1}	q_s^{Fe1}	q_s^{Fe2}	$\hat{S}^2$
DFT UOPBE/B97-3c (SMD, solvent = MeCN)						
[LS-cat-SQ-HS] **a**	7/2	-8174.979993	4.0	1.09	4.04	15.783
[LS-cat-SQ-HS] **b**	7/2	-8174.986311	0.0	1.11	4.03	15.783
DFT UOPBE/Def2-TZVP (SMD, solvent = MeCN)						
[LS-cat-SQ-HS] **a**	7/2	-8176.436247	1.0	1.16	4.11	15.783
[LS-cat-SQ-HS] **b**	7/2	-8176.437795	0.0	1.12	4.12	15.784

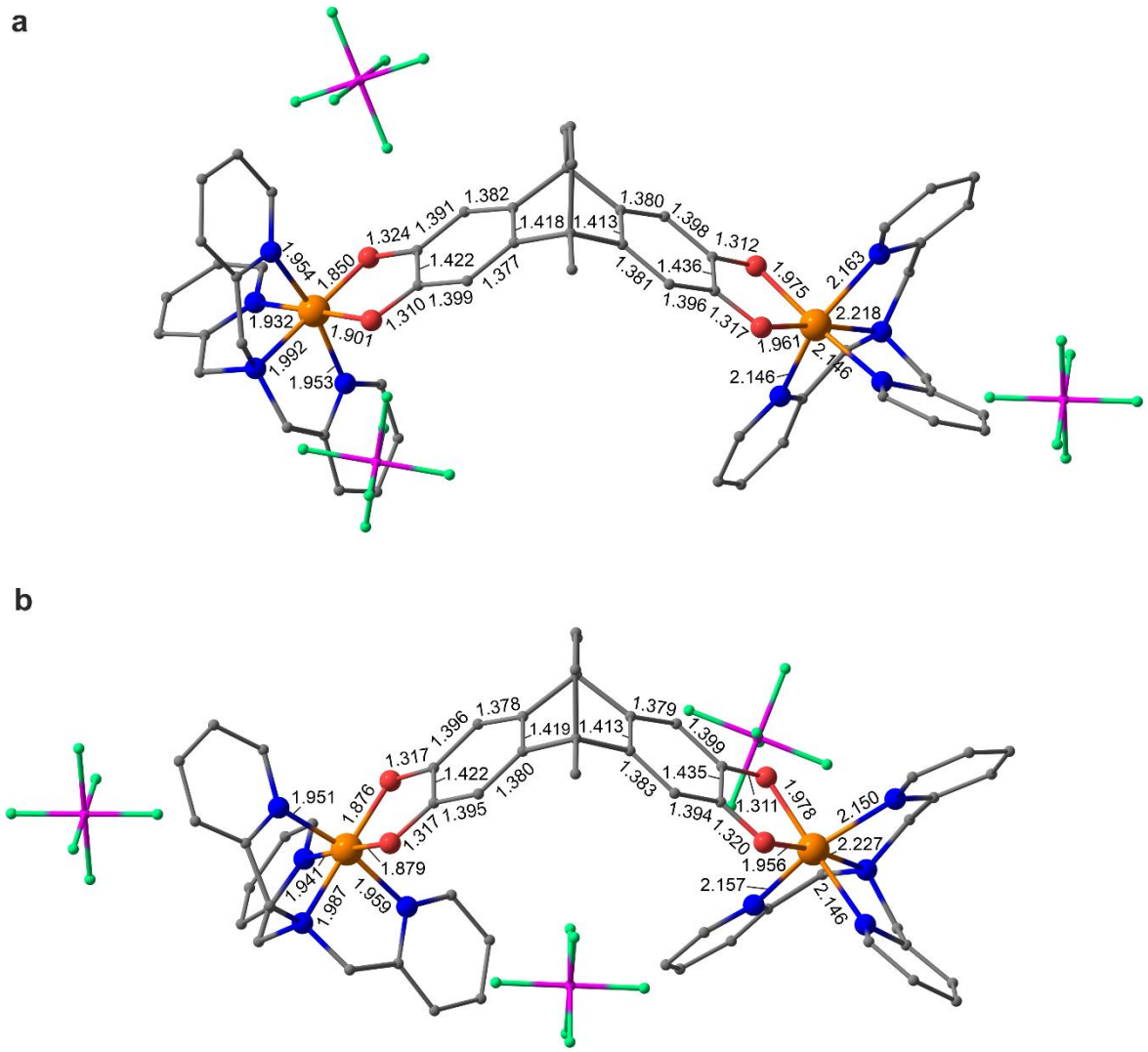

Figure S82. Optimized geometries of the [LS-HS] state of **2** as calculated by the DFT UOPBE/B97-3c (SMD, solvent = MeCN) method with inclusion of the PF_6^- counterions into the computational scheme. Hydrogen atoms have been omitted for clarity.

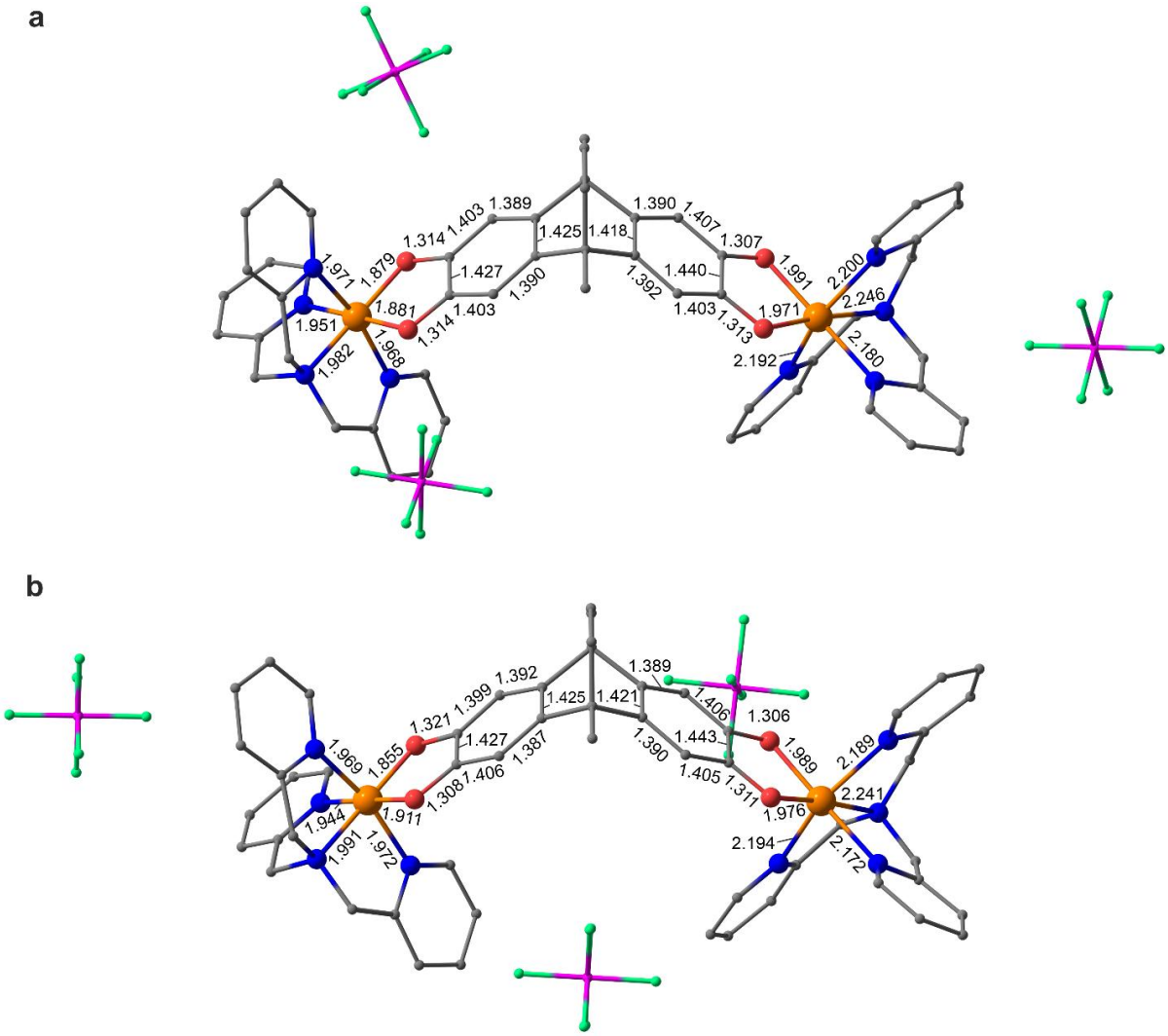

Figure S83. Optimized geometries of the [LS-HS] state of **2** as calculated by the DFT UOPBE/Def2-TZVP (SMD, solvent = MeCN) method with inclusion of the PF_6^- counterions into the computational scheme. Hydrogen atoms have been omitted for clarity.

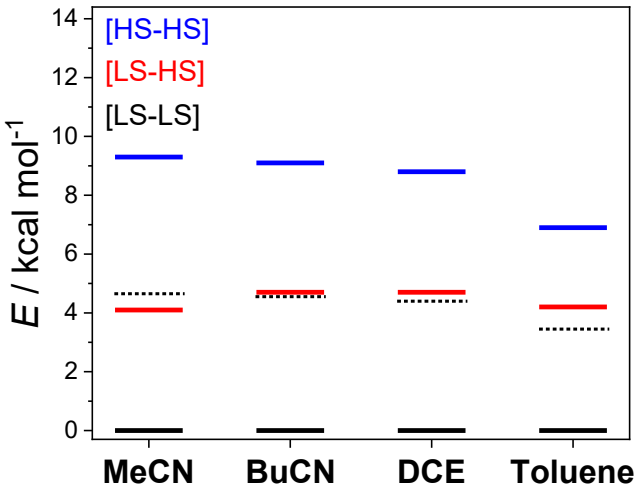

Figure S84. Relative energies of electronic states for **2** calculated by the DFT UOPBE/Def2-TZVP (SMD, solvent = acetonitrile, butyronitrile, 1,2-dichloroethane, and toluene) method. Dashed lines correspond to the halfway E between the [HS-HS] and [LS-LS] states ($\Delta E/2$). Calculated ρ values of −0.059 (MeCN), 0.016 (BuCN), 0.034 (DCE), and 0.11 (toluene).

References

(1) D. Fritsch, G. Bengtson, M. Carta and N. B. McKeown, Synthesis and Gas Permeation Properties of Spirobischromane-Based Polymers of Intrinsic Microporosity, *Macromol. Chem. Phys.*, 2011, **212**, 1137–1146.

(2) J. T. Janetzki, M. G. Chegerev, G. K. Gransbury, R. W. Gable, J. K. Clegg, R. J. Mulder, G. N. L. Jameson, A. A. Starikova and C. Boskovic, . Controlling Spin Crossover in a Family of Dinuclear Fe(III) Complexes via the Bis(Catecholate) Bridging Ligand, *Inorg. Chem.*, 2023, **62**, 15719–15735.

(3) J. T. Janetzki, G. K. Gransbury, R. W. Gable, M. J. Giansiracusa, A. A. Starikova and C. Boskovic, Tuning Valence Tautomerism in Dinuclear Cobalt Complexes by Modulating Communication in the Bridging Ligand, *Eur. J. Inorg. Chem.*, 2024, **27**, 1–15.

(4) D. Aragão, J. Aishima, H. Cherukuvada, R. Clarken, M. Clift, N. P. Cowieson, D. J. Ericsson, C. L. Gee, S. Macedo, N. Mudie, S. Panjikar, J. R. Price, A. Riboldi-Tunnicliffe, R. Rostan, R. Williamson and T. T. Caradoc-Davies, MX2: A High-Flux Undulator Microfocus Beamline Serving Both the Chemical and Macromolecular Crystallography Communities at the Australian Synchrotron, *J. Synchrotron Radiat.*, 2018, **25**, 885–891.

(5) N. P. Cowieson, D. Aragao, M. Clift, D. J. Ericsson, C. Gee, S. J. Harrop, N. Mudie, S. Panjikar, J. R. Price, A. Riboldi-Tunnicliffe, R. Williamson and T. Caradoc-Davies, MX1: A Bending-Magnet Crystallography Beamline Serving Both Chemical and Macromolecular Crystallography Communities at the Australian Synchrotron, *J. Synchrotron Radiat.*, 2015, **22**, 187–190.

(6) G. M. Sheldrick, SADABS, University of Göttingen, Germany, 1996.

(7) G. M. Sheldrick, SHELXT − Integrated Space-Group and Crystal-Structure Determination, *Acta Crystallogr., Sect. A: Found. Adv.*, 2015, **71**, 3–8.

(8) G. M. Sheldrick, Acta Crystallogr., Sect. C: Struct. Chem., 2015, 71, 3–8.

(9) O. V. Dolomanov, L. J. Bourhis, R. J. Gildea, J. A. K. K. Howard and H. Puschmann, OLEX2: A Complete Structure Solution, Refinement and Analysis Program, *J. Appl. Crystallogr.*, 2009, **42**, 339–341.

(10) P. van der Sluis and A. L. Spek, BYPASS: An Effective Method for the Refinement of Crystal Structures Containing Disordered Solvent Regions, *Acta Crystallogr., Sect. A: Found. Adv.*, 1990, **46**, 194–201.

(11) D. F. Evans, The Determination of the Paramagnetic Susceptibility of Substances in Solution by Nuclear Magnetic Resonance, *J. Chem. Soc.*, 1959, 2003..

(12) S. Brahma and R. L. Gardas, Understanding the Solvation Behavior of Pyrrolidinium Based Ionic Liquids in Acetonitrile through Thermophysical Properties at 293.15 to 328.15 K, *J. Mol. Liq.*, 2018, **256**, 22–28..

(13) S. O. Morgan and H. H. Lowry, Dielectric Polarization of Some Pure Organic Compounds in the Dissolved, Liquid, and Solid States, *J. Phys. Chem.*, 1930, **34**, 2385–2432.

(14) G. A. Bain and J. F. Berry, Diamagnetic Corrections and Pascal's Constants, *J. Chem. Educ.*, 2008, **85**, 532.

(15) N. F. Chilton, R. P. Anderson, L. D. Turner, A. Soncini and K. S. Murray, *PHI*: A Powerful New Program for the Analysis of Anisotropic Monomeric and Exchange-Coupled Polynuclear d- and f-Block Complexes, *J. Comput. Chem.*, 2013, **34**, 1164–1175.

(16) S. Stoll and A. Schweiger, EasySpin, a Comprehensive Software Package for Spectral Simulation and Analysis in EPR, *J. Mag. Res.*, 2006, **178**, 42–55

(17) M. J. Frisch, G. W. Trucks, H. B. Schlegel, G. E. Scuseria, M. A. Robb, J. R. Cheeseman, G. Scalmani, V. Barone, G. A. Petersson, H. Nakatsuji, X. Li, M. Caricato, A. V.

Marenich, J. Bloino, B. G. Janesko, R. Gomperts, B. Mennucci, H. P. Hratchian, J. V. Ortiz, A. F. Izmaylov, J. L. Sonnenberg, D. Williams-Young, F. Ding, F. Lipparini, F. Egidi, J. Goings, B. Peng, A. Petrone, T. Henderson, D. Ranasinghe, V. G. Zakrzewski, J. Gao, N. Rega, G. Zheng, W. Liang, M. Hada, M. Ehara, K. Toyota, R. Fukuda, J. Hasegawa, M. Ishida, T. Nakajima, Y. Honda, O. Kitao, H. Nakai, T. Vreven, K. Throssell, J. A. Montgomery Jr., J. E. Peralta, F. Ogliaro, M. J. Bearpark, J. J. Heyd, E. N. Brothers, K. N. Kudin, V. N. Staroverov, T. A. Keith, R. Kobayashi, J. Normand, K. Raghavachari, A. P. Rendell, J. C. Burant, S. S. Iyengar, J. Tomasi, M. Cossi, J. M. Millam, M. Klene, C. Adamo, R. Cammi, J. W. Ochterski, R. L. Martin, K. Morokuma, O. Farkas, J. B. Foresman and D. J. Fox, Gaussian 16, Revision C.01, Gaussian, Inc., Wallingford, CT, 2016.

(18) M. Swart, A. W. Ehlers and K. Lammertsma, Performance of the OPBE Exchange-Correlation Functional, *Mol. Phys.*, 2004, **102**, 2467–2474.

(19) M. Swart, A. R. Groenhof, A. W. Ehlers and K. Lammertsma, Validation of Exchange-Correlation Functional for Spin States of Iron Complexes, *J. Phys. Chem. A*, 2004, **108**, 5479–5483.

(20) F. Neese, Software Update: The Orace Program System—Version 5.0. *WIREs Comput. Mol. Sci.* 2022, **12**, 1–15.

(21) F. Neese, Software Update: The ORCA Program System, Version 4.0. *WIREs Comput. Mol. Sci.* 2018, **8**, 4–9.

(22) F. Neese and F. Wennmohs, U. Becker, C. Riplinger, The ORCA Quantum Chemistry Program Package. *J. Chem. Phys.* **2020**, 152.

(23) F. Neese, The ORCA Program System. *Wiley Interdiscip. Rev. Comput. Mol. Sci.* 2012, **2**, 73–78.

(24) A. V. Marenich, C. J. Cramer and D. G. Truhlar, Universal Solvation Model Based on Solute Electron Density and on a Continuum Model of the Solvent Defined by the Bulk Dielectric Constant and Atomic Surface Tensions. *J. Phys. Chem. B* **2009**, *113*, 6378–6396.

(25) G. A. Andrienko, Chemcraft - Graphical Software for Visualization of Quantum Chemistry Computations.

(26) P. Tourón Touceda, S. Mosquera Vázquez, M. Lima, A. Lapini, F. Paolo, D. Andrea and R. Roberto, Transient Infrared Spectroscopy: A New Approach to Investigate Valence Tautomerism, *Phys. Chem. Chem. Phys.*, 2012, **14**, 1038–1047.

(27) G. K. Gransbury, B. N. Livesay, J. T. Janetzki, M. A. Hay, R. W. Gable, M. P. Shores, A. Starikova and C. Boskovic, Understanding the Origin of One- or Two-Step Valence Tautomeric Transitions in Bis(Dioxolene)-Bridged Dinuclear Cobalt Complexes, *J. Am. Chem. Soc.*, 2020, **142**, 10692–10704.

(28) K. G. Alley, G. Poneti, P. S. D. Robinson, A. Nafady, B. Moubaraki, J. B. Aitken, S. C. Drew, C. Ritchie, B. F. Abrahams, R. K. Hocking, K. S. Murray, A. M. Bond, H. H. Harris, L. Sorace and C. Boskovic, Redox Activity and Two-Step Valence Tautomerism in a Family of Dinuclear Cobalt Complexes with a Spiroconjugated Bis(Dioxolene) Ligand, *J. Am. Chem. Soc.*, 2013, **135**, 8304–8323

(29) F. Rupp, K. Chevalier, M. Graf, M. Schmitz, H. Kelm, A. Grün, M. Zimmer, M. Gerhards, C. van Wüllen, H.-J. Krüger and R. Diller, Spectroscopic, Structural, and Kinetic Investigation of the Ultrafast Spin Crossover in an Unusual Cobalt(II) Semiquinonate Radical Complex, *Chem. – Eur. J.*, 2017, **23**, 2119–2132.

(30) X. Xuan, J. Wang and H. Wang, Theoretical Insights into PF_6^- and Its Alkali Metal Ion Pairs: Geometries and Vibrational Frequencies, *Electrochim. Acta*, 2005, **50**, 4196–4201

(31) C. R. Tichnell, D. A. Shultz, C. V. Popescu, I. Sokirniy and P. D. Boyle, Synthesis, Characterization, and Photophysical Studies of an Iron(III) Catecholate-Nitronylnitroxide Spin-Crossover Complex, *Inorg. Chem.*, 2015, **54**, 4466–4474.
(32) A. J. Simaan, M.-L. Boillot, R. Carrasco, J. Cano, J.-J. Girerd, T. A. Mattioli, J. Ensling, H. Spiering and P. Gütlich, Electronic, Vibrational, and Structural Properties of a Spin-Crossover Catecholato-Iron System in the Solid State: Theoretical Study of the Electronic Nature of the Doublet and Sextet States. *Chem. – Eur. J.*, 2005, **11**, 1779–1793.
(33) M. Chegerev, O. Demidov, P. Vasilyev, N. Efimov, S. Kubrin, A. Starikov, V. Vlasenko, A. Piskunov, S. Shapovalova, A. Guda, Y. Rusalev and A. Soldatov, Spin Transitions in Ferric Catecholate Complexes Mediated by Outer-Sphere Counteranions. *Dalton Trans.* 2022, **51**, 10909–10919.
(34) T. Tezgerevska, E. Rousset, R. W. Gable, G. N. L. Jameson, E. C. Sañudo, A. Starikova and C. Boskovic, Valence Tautomerism and Spin Crossover in Pyridinophane–Cobalt–Dioxolene Complexes: An Experimental and Computational Study. *Dalton Trans.* 2019, **48**, 11674–11689.
(35) S. Floquet, A. J. Simaan, E. Rivière, M. Nierlich, P. Thuéry, J. Ensling, P. Gütlich, J.-J. Girerd and M.-L. Boillot, Spin Crossover of Ferric Complexes with Catecholate Derivatives. Single-Crystal X-Ray Structure, Magnetic and Mössbauer Investigations. *Dalton Trans.* 2005, 1734–1742.
(36) W. O. Koch, V. Schünemann, M. Gerdan, A. X. Trautwein and H.-J. Krüger, Evidence for an Unusual Thermally Induced Low-Spin (S=1/2) ⇄ Intermediate-Spin (S=3/2) Transition in a Six-Coordinate Iron(III) Complex: Structure and Electronic Properties of a (1,2-Benzenedithiolato)Iron(III) Complex Containing N,N′-Dimethyl-2,11-Diaza[3.3](2,6)pyridinophane as Ligand *Chem. – Eur. J.*, 1998, **4**, 686–691.
(37) M. Schmitz, M. Seibel, H. Kelm, S. Demeshko, F. Meyer and H.-J. Krüger, How Does a Coordinated Radical Ligand Affect the Spin Crossover Properties in an Octahedral Iron(II) Complex? *Angew. Chem., Int. Ed.,* 2014, **53**, 5988–5992.
(38) J. T. Henthorn, G. E. Cutsail, T. Weyhermüller and S. DeBeer, Stabilization of Intermediate Spin States in Mixed-Valent Diiron Dichalcogenide Complexes. *Nat. Chem.* 2022, **14**, 328–333.
(39) S. Llunell, M. Casanova, D. Cirera, J. Alemany and P. Alvarez, SHAPE 2.1, 2013.
(40) S. Alvarez, D. Avnir, M. Llunell and M. Pinsky, Continuous Symmetry Maps and Shape Classification. The Case of Six-Coordinated Metal Compounds, *New J. Chem.*, 2002, **26**, 996–1009..
(41) R. Ketkaew, Y. Tantirungrotechai, P. Harding, G. Chastanet, P. Guionneau, M. Marchivie and D. J. Harding, OctaDist: A Tool for Calculating Distortion Parameters in Spin Crossover and Coordination Complexes, *Dalton Trans.*, 2021, **50**, 1086–1096.
(42) S. N. Brown, Metrical Oxidation States of 2-Amidophenoxide and Catecholate Ligands: Structural Signatures of Metal–Ligand π Bonding in Potentially Noninnocent Ligands, *Inorg. Chem.*, 2012, **51**, 1251–1260.
(43) O. Carugo, C. B. Castellani, K. Djinovic and M. Rizzi, Derived from O-Benzoquinone: Statistical Correlation between Oxidation State and Structural Features, *Dalton Trans.*, 1992, 837–841.
(44) G. K. Gransbury, M.-E. Boulon, R. A. Mole, R. W. Gable, B. Moubaraki, K. S. Murray, L. Sorace, A. Soncini and C. Boskovic, Single-Ion Anisotropy and Exchange Coupling in Cobalt(II)-Radical Complexes: Insights from Magnetic and *Ab Initio* Studies, *Chem. Sci.*, 2019, **10**, 8855–8871.

(45) C. Benelli, A. Dei, D. Gatteschi and L. Pardi, Electronic and CD Spectra of Catecholate and Semiquinonate Adducts of Zinc(II) and Nickel(II) Tetraaza Macrocyclic Complexes, *Inorg. Chem.*, 1989, **28**, 1476–1480.
(46) M. E. Bodini, G. Copia, R. Robinson and D. T. Sawyer, Redox Chemistry of Metal-Catechol Complexes in Aprotic Media. 5. 3,5-Di-*Tert*-Butylcatecholato and 3,5-Di-*Tert*-Butyl-*o*-Benzosemiquinonato Complexes of Zinc(II), *Inorg. Chem.*, 1983, **22**, 126–129
(47) V. L. Nadurata and C. Boskovic, Switching Metal Complexes via Intramolecular Electron Transfer: Connections with Solvatochromism, *Inorg. Chem. Front.*, 2021, **8**, 1840–1864.
(48) S. Rodríguez-Jiménez, A. S. Barltrop, N. G. White, H. L. C. Feltham and S. Brooker, Solvent Polarity Predictably Tunes Spin Crossover $T_{1/2}$ in Isomeric Iron(II) Pyrimidine Triazoles, *Inorg. Chem.*, 2018, **57**, 6266–6282.
(49) S. Sundaresan, J. A. Kitchen and S. Brooker, Hydrophobic Tail Length in Spin Crossover Active Iron(II) Complexes Predictably Tunes $T_{½}$ in Solution and Enables Surface Immobilisation, *Inorg. Chem. Front.*, 2020, **7**, 2050–2059.
(50) M. Higuchi, Y. Hitomi, H. Minami, T. Tanaka and T. Funabiki, Correlation of Spin States and Spin Delocalization with the Dioxygen Reactivity of Catecholatoiron(III) Complexes, *Inorg. Chem.*, 2005, **44**, 8810–8821.
(51) A. Bencini, C. A. Daul, A. Dei, F. Mariotti, H. Lee, D. A. Shultz and L. Sorace, Charge Distribution in Bis-Dioxolene Radical Metal Complexes. Synthesis and DFT Characterization of Dinuclear Co(III) and Cr(III) Complexes with a Mixed-Valent, S = 1/2 Semiquinone-Catecholate Ligand, *Inorg. Chem.*, 2001, **40**, 1582–1590.
(52) C. Benelli, A. Dei, D. Gatteschi and L. Pardi, Redox Potentials and Charge Transfer Spectra of Catecholate and Semiquinone Adducts of a Cobalt-Tetraazamacrocyclic Complex, *Inorganica Chim. Acta*, 1989, **163**, 99–104
(53) D. D. Cox, S. J. Benkovic, L. M. Bloom, F. C. Bradley, M. J. Nelson, L. Que and D. E. Wallick, Catecholate LMCT Bands as Probes for the Active Sites of Nonheme Iron Oxygenases, *J. Am. Chem. Soc.*, 1988, **110**, 2026–2032.
(54) S.-Q. Wu, M. Liu, K. Gao, S. Kanegawa, Y. Horie, G. Aoyama, H. Okajima, A. Sakamoto, M. L. Baker, M. S. Huzan, P. Bencok, T. Abe, Y. Shiota, K. Yoshizawa, W. Xu, H.-Z. Kou and O. Sato, Macroscopic Polarization Change via Electron Transfer in a Valence Tautomeric Cobalt Complex, *Nat. Commun.*, 2020, **11**, 1992.
(55) J. J. Loughrey, S. Sproules, E. J. L. McInnes, M. J. Hardie and M. A. Halcrow, Stable Mixed-Valent Radicals from Platinum(II) Complexes of a Bis(Dioxolene) Ligand, *Chem. – Eur. J.*, 2014, **20**, 6272–6276.
(56) W. O. Koch, V. Schünemann, M. Gerdan, A. X. Trautwein and H.-J. Krüger, Structural, Spectroscopic, and Chemical Properties of the First Low-Spin Iron(III) Semiquinonate Complexes in the Solid State and in Solution, *Chem. – Eur. J.*, 1998, **4**, 1255–1265.
(57) A. Diebold and K. S. Hagen, Iron(II) Polyamine Chemistry: Variation of Spin State and Coordination Number in Solid State and Solution with Iron(II) Tris(2-Pyridylmethyl)Amine Complexes, *Inorg. Chem.*, 1998, .**37**, 215–223.
(58) A. L. Ward, L. Elbaz, J. B. Kerr and J. Arnold, Nonprecious Metal Catalysts for Fuel Cell Applications: Electrochemical Dioxygen Activation by a Series of First Row Transition Metal Tris(2-Pyridylmethyl)Amine Complexes, *Inorg. Chem.*, 2012, **51**, 4694–4706.
(59) A. Robinson, D. John, O. Nickel, I. I. Complexes, A. Robinson, J. D. Curry and H. Busch, Complexes Derived from Strong Field Ligands. XVII. Electronic Spectra of Octahedral Nickel(II) Complexes with Ligands of the α-Diimine and Closely Related Classes, *Inorg. Chem.*, 1963, **2**, 1178–1181..
(60) P. Robin and Melvin B. Day, Mixed Valence Chemistry-A Survey and Classification, *Adv. Inorg. Chem. Radiochem.*, 1967, **10**, 247–422

(61) D. M. D'Alessandro and F. R. Keene, Current Trends and Future Challenges in the Experimental, Theoretical and Computational Analysis of Intervalence Charge Transfer (IVCT) Transitions, *Chem. Soc. Rev.*, 2006, **35**, 424–440.
(62) A. Arnold, T. J. Sherbow, R. I. Sayler, R. D. Britt, E. J. Thompson, M. T. Muñoz, J. C. Fettinger and L. A. Berben, Organic Electron Delocalization Modulated by Ligand Charge States in $[L_2M]^{n-}$ Complexes of Group 13 Ions, *J. Am. Chem. Soc.*, 2019, **141**, 15792–15803.
(63) K. Tahara, T. Kadowaki, J. Kikuchi, Y. Ozawa, S. Yoshimoto and M. Abe, Synthesis and Characterization of a New Series of Binuclear Pd(II) Biscatecholato Complexes: Non-Innocent Ligand-Based Approach to a Wide Range of Variation in Near-Infrared Absorptions of Mixed-Valence Complexes, *Bull. Chem. Soc. Jpn.*, 2018, **91**, 1630–1639.
(64) Á. Moneo, G. C. Justino, M. F. N. N. Carvalho, M. C. Oliveira, A. M. M. Antunes, D. Bléger, S. Hecht and J. P. Telo, Electronic Communication in Linear Oligo(Azobenzene) Radical Anions, *J. Phys. Chem. A*, 2013, **117**, 14056–14064.
(65) K. D. Demadis, C. M. Hartshorn and T. J. Meyer, The Localized-to-Delocalized Transition in Mixed-Valence Chemistry, *Chem. Rev.*, 2001, **101**, 2655–2685.
(66) N. S. Hush, Homogeneous and Heterogeneous Optical and Thermal Electron Transfer, *Electrochim. Acta*, 1968, **13**, 1005–1023
(67) B. S. Brunschwig and N. Sutin, Energy Surfaces, Reorganization Energies, and Coupling Elements in Electron Transfer, *Coord. Chem. Rev.*, 1999, **187**, 233–254.
(68) O. S. Siig and K. P. Kepp, Iron(II) and Iron(III) Spin Crossover: Toward an Optimal Density Functional. *J. Phys. Chem. A* 2018, **122**, 4208–4217.
(69) M. Swart, Accurate Spin-State Energies for Iron Complexes. *J. Chem. Theory Comput.* 2008, **4**, 2057–2066.
(70) J. Sirirak, D. Sertphon, W. Phonsri, P. Harding and D. J. Harding, Comparison of Density Functionals for the Study of the High Spin Low Spin Gap in Fe(III) Spin Crossover Complexes. *Int. J. Quantum Chem.* 2017, **117**, 1–8.
(71) Y. Zhang and W. Yang, Challenge for Density Functionals: Self-Interaction Error Increases for Systems with a Noninteger Number of Electrons, *J. Chem. Phys.*, 1998, **109**, 2604–2608.
(72) J. L. Bao, L. Gagliardi and D. G. Truhlar, Self-Interaction Error in Density Functional Theory: An Appraisal, *J. Phys. Chem. Lett.*, 2018, **9**, 2353–2358.
(73) D. R. Lonsdale and L. Goerigk, The One-Electron Self-Interaction Error in 74 Density Functional Approximations: A Case Study on Hydrogenic Mono- And Dinuclear Systems, *Phys. Chem. Chem. Phys.*, 2020, **22**, 15805–15830.
(74) V. N. Staroverov, G. E. Scuseria, J. Tao and J. P. Perdew, Comparative Assessment of a New Nonempirical Density Functional: Molecules and Hydrogen-Bonded Complexes, *J. Chem. Phys.*, 2003, **119**, 12129–12137.
(75) J. Tao, J. P. Perdew, V. N. Staroverov and G. E. Scuseria, Climbing the Density Functional Ladder: Nonempirical Meta–Generalized Gradient Approximation Designed for Molecules and Solids, *Phys. Rev. Lett.*, 2003, **91**, 146401.
(76) L. Noodleman, Valence Bond Description of Antiferromagnetic Coupling in Transition Metal Dimers, *J. Chem. Phys.*, 1981, **74**, 5737–5743.
(77) M. Shoji, K. Koizumi, Y. Kitagawa, T. Kawakami, S. Yamanaka, M. Okumura and K. Yamaguchi, A General Algorithm for Calculation of Heisenberg Exchange Integrals J in Multispin Systems, *Chem. Phys. Lett.*, 2006, **432**, 343–347.
(78) R. P. Joshi, J. J. Phillips, K. J. Mitchell, G. Christou, K. A. Jackson and J. E. Peralta, Accuracy of Density Functional Theory Methods for the Calculation of Magnetic Exchange Couplings in Binuclear Iron(III) Complexes, *Polyhedron*, 2020, **176**, 114194.

(79) C. J. Cramer and D. G. Truhlar, Density Functional Theory for Transition Metals and Transition Metal Chemistry, *Phys. Chem. Chem. Phys.*, 2009, **11**, 10757–10816.
(80) S. Weissman, M. Antkowiak, B. Brzostowski, G. Kamieniarz and L. Kronik, Accurate Magnetic Couplings in Chromium-Based Molecular Rings from Broken-Symmetry Calculations within Density Functional Theory, *J. Chem. Theory Comput.*, 2019, **15**, 4885–4895.
(81) J. J. Phillips and J. E. Peralta, Towards the Blackbox Computation of Magnetic Exchange Coupling Parameters in Polynuclear Transition-Metal Complexes: Theory, Implementation, and Application, *J. Chem. Phys.*, 2013, **138**, 174115.
(82) H. C. Fitzhugh, J. W. Furness, M. R. Pederson, J. E. Peralta and J. Sun, Comparative Density Functional Theory Study of Magnetic Exchange Couplings in Dinuclear Transition-Metal Complexes, *J. Chem. Theory Comput.*, 2023, **19**, 5760–5772.